Synthesis, Characterization and *in situ* Catalysis of Silica SBA-15 Supported Molybdenum Oxide Model Catalysts

Dissertation von Dipl.-Chem. Jörg Thielemann

TECHNISCHE
UNIVERSITÄT
DARMSTADT

Synthesis, Characterization and *in situ* Catalysis of Silica SBA-15 Supported Molybdenum Oxide Model Catalysts

von

Jörg Thielemann

Diplom Chemiker

aus Berlin

vom Fachbereich VII – Chemie
der Technischen Universität Darmstadt
zur Erlangung des akademischen Grades
Doktor der Naturwissenschaften

Dr. rer. nat.

genehmigte Dissertation

Referent:	**Prof. Dr. Christian Hess**
Koreferent I:	**Prof. Dr. Robert Schlögl**
Koreferent II:	**Prof. Dr. Reinhard Schomäcker**
Fachprüfer I:	**Prof. Dr. Jörg Schneider**
Fachprüfer II:	**Prof. Dr. Rolf Schäfer**

Tag der Einreichung:	**20. Dezember 2010**
Tag der wissenschaftlichen Aussprache:	**14. Februar 2011**

Darmstadt 2011

D17

Danksagung

Zuallererst möchte ich mich herzlich bei Herrn Prof. Dr. Robert Schlögl für die Überlassung des interessanten Themas und für die Anregungen und Unterstützung beim Erstellen dieser Arbeit bedanken.

Des Weiteren möchte ich mich bei Herrn Prof. Dr. Christian Hess für die vielen Diskussionen, die exzellente Betreuung und die Schaffung eines sehr angenehmen Gruppenklimas in den Arbeitskreisen in Berlin und in Darmstadt bedanken. Beiden Professoren bin ich zu Dank verpflichtet für die Möglichkeit, meine Arbeiten nach der Berufung von Prof. Hess an die Technische Universität Darmstadt sowohl in Berlin als auch in Darmstadt fortzuführen.

Bei Frau Jutta Kröhnert möchte ich mich herzlich ich für die Durchführung der IR-spektroskopischen Untersuchungen und bei Frau Dr. Trunschke für die Diskussionen bedanken. Außerdem danke ich herzlich Herrn Lenard-Istvan Csepei für die Hilfe bei der Durchführung der katalytischen Testung/Analyse bedanken.

Herr Prof. Dr. Ressler und Frau Anke Walter von der Technischen Universität Berlin danke ich für die Durchführung und Auswertung der EXAFS-Experimente am HASYLAB in Hamburg.

Weiterhin möchte ich mich bei Rita Herbert, Frank Girgsdies, Gisela Lorenz, Gisela Weinberg, Wei Zhang, Genka Tzolova-Müller, Olaf Timpe, Lars Giebeler, Karl Kopp und Dominik Stranz, den Werkstätten und allen anderen Kollegen am Fritz-Haber Institut und der TU Darmstadt die zum Gelingen dieser Arbeit beigetragen haben herzlich danken.

Bei meinen Eltern und meiner Familie möchte ich mich besonders für die moralische Unterstützung während der Anfertigung der Dissertation bedanken.

Abstract

This work describes the synthesis, the structural characterization and the catalytic testing of silica SBA-15 supported molybdenum oxide model catalysts. Additionally, a solvent induced washing effect during the SBA-15 synthesis and its scale up on the SBA-15 structure was studied. The Mo_xO_y/SBA-15 catalysts were prepared with a Mo loading between 1.0 and 21.1 wt.% Mo (0.2 to 9.8 Mo/nm^2) by a grafting/ion exchange procedure and incipient wetness impregnation. The catalyst structure was analyzed with Raman-, UV/Vis-, Photoelectron-, X-ray absorption- and IR spectroscopy. Furthermore, the catalyst structure was studied under reaction conditions in presence of propylene/oxygen and steam in an *in situ* Raman-MS setup, which was constructed in the course of this work.

The study of washing SBA-15 with two solvents (water and ethanol) with nitrogen adsorption and XRD revealed that the surface area can be increased by 25% to 800 m^2/g compared to washing with a single solvent. Moreover, it was found that huge solvent quantities for washing should be avoided, as they induce hydrolysis reactions, which alter the SBA-15 structure and lead to a widening and narrowing of certain mesopore sections. This decreases the surface area and pore volume of the support. The effect decreases with up-scaling of the synthesis.

For the Mo_xO_y/SBA-15 catalysts the molybdenum oxide was observed on the support in a dispersed state up to a loading of 12.1 wt.% Mo (3.5 Mo/nm^2). Above this loading crystalline α-MoO_3 and as minority phase β-MoO_3 are formed. In this loading region the fraction of dispersed molybdenum oxide was almost constant at 12 to 13 wt.% Mo.

Regarding the dispersed molybdenum oxide two structurally different states were observed. The hydrated state exists in the presence of moisture at room temperature, whereas the dehydrated state is obtained after treatment over 350°C in synthetic air.

The molybdenum oxide structure in the hydrated state can be described as preferentially octahedral centres, which also exhibit connections and form di- or oligomers beside monomers.

Comparing the XPS data of the dehydrated and the hydrated state showed that the molybdenum oxide was higher dispersed in the dehydrated state. UV/Vis spectroscopy supported this finding and showed that beside monomeric also di- or oligomeric species were present at Mo densities in the range of dispersed molybdenum oxide ($\leq$3.5 Mo/nm^2). Connections between neighbouring molybdenum oxide centres were detected by EXAFS and IR Spectroscopy using nitric oxide as probe molecule. Furthermore, a octahedral to tetrahedral ratio of 1 : 3 was found by a XANES fit. Therefore, the molybdenum oxide structure of the dehydrated state can be described as dispersed tetrahedral and octahedral molybdenum oxide centres, which coexist as monomers and connected di- or oligomers on the silica support surface. Moreover, the size distribution of the dispersed molybdenum oxide species in the hydrated and dehydrated state seems to be independent of the loading.

Mo_xO_y/SBA-15 was catalytically tested in the selective oxidation of propylene and propane. Whereas propylene was oxidized selectively to propionaldehyde, acetone and acrolein as major products, the oxidation of propane led unselectively to CO_x. *In situ* Raman investigations reveal that during the propylene oxidation or in the presence of steam, the structure of the catalyst largely resembles the structure of dehydrated dispersed molybdenum oxide.

Zusammenfassung

Die Arbeit beschreibt die Synthese, die strukturelle Charakterisierung und die katalytische Untersuchung von Silika SBA-15 getragenen Molybdänoxid-Modelkatalysatoren. Des Weiteren wurde ein durch Lösungsmittel induzierter Wascheffekt untersucht, welcher während der SBA-15 Synthese und bei der Vergrößerung des Ansatzes auftrat. Die Herstellung der Mo_xO_y/SBA-15-Katalysatoren erfolgte mit einer Aufpfropf/Ionenaustausch- und einer Trockenimprägnierungsmethode im Beladungsbereich von 1.0 bis 21.1 Gew.% Mo (0.2 to 9.8 Mo/nm^2). Die Struktur des Katalysators wurde dabei mit Raman-, UV/Vis-, Photoelektronen-, Röntgenabsorptions- und Infrarotspektroskopie analysiert. Des Weiteren erfolgte eine Untersuchung der Katalysatorstruktur unter Reaktionsbedingungen in einer Propylen/Sauerstoff und Wasserdampfatmosphäre in einem *in situ* Raman-MS Aufbau, der im Rahmen dieser Arbeit konstruiert wurde.

Die Untersuchung der Auswirkungen des Waschens bei SBA-15 mit zwei Lösungsmitteln (Wasser und Ethanol) mit Stickstoffadsorption und XRD zeigte, dass die Oberfläche um 25% auf 800 m^2/g vergrößert werden kann, verglichen mit dem Waschen mit einem Lösungsmittel. Es wurde des Weiteren festgestellt, dass große Lösungsmittelmengen beim Waschen vermieden werden sollten, da diese Hydrolysereaktionen im Silikatgerüst auslösen können. Durch Aufweitung und Verengung von einzelnen Abschnitten der Mesoporen führt dies zu einer Veränderung der SBA-15-Struktur und bewirkt dadurch eine Verringerung der Oberfläche und des Porenvolumens. Der beobachtete Effekt wird mit steigender Ansatzgröße geringer.

Die Analyse des Mo_xO_y/SBA-15-Katalysators zeigte, dass Molybdänoxide auf der Trägeroberfläche bis zu einer Beladung von 12.1 Gew.% Mo (3.5 Mo/nm^2) ausschließlich in einem dispersem Zustand vorliegen. Bei höheren Beladungen wird kristallines α-MoO_3 und als Minoritätsphase β'-MoO_3 gebildet. Der Anteil an dispersem Molybdänoxid ist in diesem Beladungsbereich bei 12 bis 13 Gew.% Mo nahezu konstant.

Für disperses Molybdänoxide existieren zwei strukturell unterschiedliche Zustände. Der hydratisierte Zustand wird bei Raumtemperatur in der Anwesenheit von

Luftfeuchtigkeit beobachtet, während der dehydratisierte Zustand nach thermischer Behandlung in synthetischer Luft bei über 350°C erhalten werden kann.

Die Struktur des Molybdänoxids im hydratisierten Zustand kann als vorzugsweise oktaedrisch koordiniert mit monomeren als auch di- oder oligomeren verknüpften Zentren beschrieben werden. Für den dehydratisierten Zustand wurde mittels XPS eine höhere Dispersion als für den hydratisierten Zustand festgestellt. Dieses Resultat wird auch durch UV/Vis-spektroskopische Ergebnisse gestützt. Weiterhin zeigen die Ergebnisse, dass neben monomeren auch di- und oligomere Spezies im Mo-Dichtenbereich von dispersem Molybdänoxid vorliegen ($\leq$3.5 Mo/nm^2). Verbindungen zwischen benachbarten Molybdänoxidzentren wurden auch durch EXAFS und IR Spektroskopie mit NO als Sondenmolekül detektiert. Weiterhin wurde durch einen XANES-Fit ein Okta- zu Tetraederverhältnis von 1 : 3 bestimmt. Die Molybdänoxidstruktur im dehydratisierten Zustand kann daher als aus okta- und tetraederischen Molybdänoxidzentren bestehend beschrieben werden, welche als Monomere und verbundene Di- und Oligomere auf der Silicaoberfläche vorkommen. Darüber hinaus scheint die Größenverteilung der dispersen Molybdänoxidspezies im hydratisierten und dehydratisierten Zustand unabhängig von der Beladung zu sein.

Weiterhin wurden auch katalytische Untersuchungen für die selektive Oxidation von Propylen und Propan am Mo_xO_y/SBA-15-Systems durchgeführt. Das Modell-katalysatorsystem oxidierte Propylen selektiv zu Propionaldehyd, Aceton und Acrolein als Hauptprodukte, während Propan nur unselektiv zu CO_x oxidiert wurde. *In situ* Raman Untersuchungen zeigten, dass der Katalysator während der Oxidation von Propylen und in Anwesenheit von Wasserdampf strukturell größtenteils dem von dehydratisiertem dispersem Molybdänoxid bei Raumtemperatur entspricht.

Contents

Abbreviations

List of symbols

a	[Å]	unit cell parameter
A	[m^2]	surface area
c	[mol]	concentration
F	[KMU]	Kubelka-Munk function
p	[Pa]	pressure
p_0	[Pa]	pressure of the adsorbate at adsorption
r	[m]	radius
t	[h]	hour
T	[K]	temperature

Abbreviations

AA	acrylic acid
ACA	acetic acid
ACR	acrolein
ACE	acetone
AHM	ammonium heptamolybdate
APTMS	3-aminopropyltrimethoxysilane
BET	method for the determination of the specifc surface area (Brunauer, Emmet, Teller)
CT	charge transfer
DFT	density functional theory
DSC	differential scanning calorimetry
FTIR	fourier transformed infrared spectroscopy
EDX	energy-dispersed X-ray spectroscopy
EO	ethylene oxide
EXAFS	extended X-ray absorption fine structure

FWHM	full width at half maximum
H^+X^-	acid media
hex-MoO_3	hexagonal MoO_3
HOMO	highest occupied molecular orbital
GC	gas chromatography
I^-	cationic inorganic solution
I^+	anionic inorganic solution
ICSD	inorganic crystal structure database
IR	infrared spectroscopy
LUMO	lowest unoccupied molecular orbital
NEXAFS	near edge X-ray absorption fine structure
NLDFT	non local density functional theory
MCM	mobil composition of matter (mesoporous silica)
MS	mass spectrometry
PA	propion aldehyde
PO	propylene oxide
PPS	polyphenylensulfide
PTFE	polytetrafluorethylene
S^-	cationic Surfactant
S^+	anionic Surfactant
SBA	Santa Barbara (mesoporous silica)
SEM	scanning electron microscopy
TEOS	tetraethoxysilane
TEM	transmission electron microscopy
TG	thermal gravimetry
UV/Vis	ultraviolet and visible spectroscopy
XANES	X-ray absorption near edge structure
XPS	X-ray photoelectron spectroscopy
XRD	X-ray diffraction

1. Introduction

1.1. Motivation

Selective catalytic oxidation processes generate approximately one quarter of the value produced world wide by catalytic processes. Therefore, those processes contribute significantly to the national income of the industrial countries. [1] Especially molybdenum oxides are of particular interest as they are often the catalytic active component of partial oxidation catalysts for industrial applications. A challenge for the study of those multi-element catalysts is their complexity and inhomogeneity on the microscopic scale. The structure of a real catalyst, for instance, might consist of several cooperating phases. Additionally, the structure of the crystalline surface, where the process of catalysis occurs, is often rich in structural defects and differs from the bulk structure, which leads to a huge variety of possible active surface sites. Moreover, due to migration of the elements between surface and bulk, the microscopic composition can differ from the macroscopic composition, as well. Therefore, in many cases it is still unclear, which structure and which composition forms the active site of the "real" catalyst.

While industrial research uses an empirical approach for the optimization, it is attempted in basic research to understand the catalytic system in all details, which is a prerequisite for tailor-made molecularly defined selective catalysts. A well established approach in basic research is to reduce the complexity of industrial catalysts to obtain simplified catalyst models, which comprise only a limited variety of the structures present in the real catalyst and are consequently easier to characterize.

The aim of this work is the investigation of model molybdenum oxide catalysts, which are less complex but still catalytically functional. These investigations are dedicated to

identify the molybdenum oxide structures in the model catalyst and to attempt to correlate them with catalytic activity. Therefore, silica SBA-15 supported nanostructured molybdenum oxide catalysts were synthesized, characterized by *ex*- and *in situ* techniques and tested for their catalytic properties in the partial oxidation of propylene.

In the following sections, an introduction to partial oxidation reactions on molybdenum oxide systems as well as the current knowledge about the structure of amorphous silica and supported molybdenum oxides is given. In later chapters, the effects of washing on the upscaling of the SBA-15 synthesis is discussed (chapter 3.). Furthermore the synthesis and structure of Mo_xO_y/SBA-15 under *ex*- and *in situ* conditions and first catalytic results on the partial oxidation of propylene are reported (chapter 4 to 6).

1.2. Molybdenum Oxide Systems in Partial Oxidation Reactions

The molybdenum oxide catalysts used for partial oxidations can be subdivided in bulk and supported catalysts. Bulk multi-element molybdenum containing catalysts are mainly used for partial oxidation or ammoxidation reactions of alkenes or aromatic hydrocarbons. The best known process in this regard is probably the two stage conversion of proplyene to acrylic acid via acrolein as intermediate catalyzed a Mo-Bi-Fe-O and a Mo-V-W-O catalyst. [2,3] The Mo-Bi-Fe-O catalyst system is also used for the ammoxidation of propylene to acrylonitrile. [1] The conversion of aromatic compounds like benzene and naphthalene to maleic and phthalic anhydride by a Mo-V-O catalysts is of industrial interest, as well. [2] Furthermore, the Mo-V-Te-Nb-O system is very promising for the direct oxidation of propane to acrylic acid. [4,5] An overview of industrial scale reactions using molybdenum containing catalysts is given in Table 1.1.

Supported molybdenum oxides are used for a variety of reactions, as for instance partial oxidation reactions of methane [6], propane [7,8], propylene [9], methanol [6,10], ethanol [11], dimethylether [12], olefin metathesis reactions [13,14] and selective reduction of nitric oxide with ammonia. [15,16] Typically, zirconia, titania, alumina and silica are used as support materials. The structure of supported molybdenum oxides especially at low loadings of typically ≤1.0 Mo/nm^2 is still a matter of debate and will be discussed in the chapters 1.3.2. and 6.

Table 1.1: Important industrial processes involving molybdenum oxides

Industrial process	Catalyst	Ref.
Oxidation of propylene to acrolein	Mo–Bi–Fe–O	[2]
Oxidation of acrolein to acrylic acid	Mo–V–W–O	[3]
Oxidation of propane to acrylic acid	Mo–V–Te–Nb–O	[4]
Oxidation of isobutene to methacrylic acid	(i) Mo–Bi–O (ii) Mo–V–P–O	[2]
Oxidation of benzene to maleic anhydride	Mo–V–O	[2]
Oxidation of naphthalene to phthalic anhydride	Mo–V–O	[2]
Ammoxidation of olefins	Mo–Bi–Fe–O	[1]

1.3. Nanostructured Supported Model Catalysts

Nanostructured materials are defined as materials with a dimension of ≤100 nm, which can be for instance clusters, crystallites or molecules. Materials in that dimension possess unusually high specific surface areas. The specific surface area of spherical silica particles with a density of typically 2.2 g/cm^3 and a radius of 1.0 nm for instance is approximately 1400 m^2/g. Similar huge surface areas can be obtained by porous

materials, such as mesoporous materials with pore diameters of 2 to 50 nm [17], which make them attractive as support materials for catalysts.

In catalysis research models are often used to gain insight into the surface structures of real bulk catalysts which are responsible for the catalytic activity. Therefore, model catalysts mimic structures of the active catalyst surface, but at the same time isolate intrinsic properties of the different catalyst components. The use of supported model catalysts is especially interesting as the high surface area of the support permits a high dispersion and thus also a good isolation of active sites. Site isolation in that sense means that active sites are not necessarily isolated mono centres, but that they can be also formed by oligomeric species present on the support. The high surface area also allows increasing the concentration of isolated active surface sites, which leads to a better traceability by spectroscopy. Furthermore, this approach also solves the problem of distinguishing between the surface and subsurface region of bulk catalyst by spectroscopy, as they are very similar in structure and composition. Additionally, a homogeneous ordered structure of the support material is favourable, as it provides a nearly identical environment for the deposition of the active metal oxide and therefore decreases the number of possible structures for the active sites. Also the support material itself should be catalytically inactive and serve as an "inert" platform for the active metal oxide. [18-20]

Ordered mesoporous silica materials fulfill these requirements. The first mesoporous materials were described in a patent by Chiola et al. in 1969, but their promising properties for other applications were not yet recognized. [21] In 1992 the interest for mesoporous materials raised, as scientists of the Mobile Oil Cooperation discovered similar mesoporous silica materials (MCM-41, -48 and -50). [22]

SBA-15, the mesoporous support material, which has been used in the course of this work, was discovered in 1998. [23,24] SBA-15 has a structure composed of hexagonal channels, a high surface area and a narrow pore size distribution. The surface area (~800 m^2) and pore width (5 to 30 nm) are tuneable by the preparation procedure.

Additionally, the framework walls of SBA-15 (3.1 to 6.4 nm) are thicker than those of MCM-41. This increases the mechanical, thermal and hydrothermal stability of SBA-15 as compared to MCM-41 [25], which makes it more preferable for catalytic applications at high temperatures and the presence of steam. Furthermore, the mechanical stability of SBA-15 can also be increased further by a post-synthesis functionalization with alkoxysilanes. [26]

1.3.1. Surface Structure of Amorphous Silica

The structure of amorphous silica consists of interlinked corner sharing SiO_4 tetrahedrals, which can be regarded as a polymer of condensed silicic acid. On the surface the structure is terminated by siloxane groups (≡Si–O–Si≡) or silanol groups (≡Si–OH). The silanol groups can be divided into isolated, geminal and vicinal silanol groups (see Fig. 1.1). The existence of geminal silanol groups is still under discussion in the literature. [27] Furthermore also interactions between the silanol groups via hydrogen bridging bonds are possible.

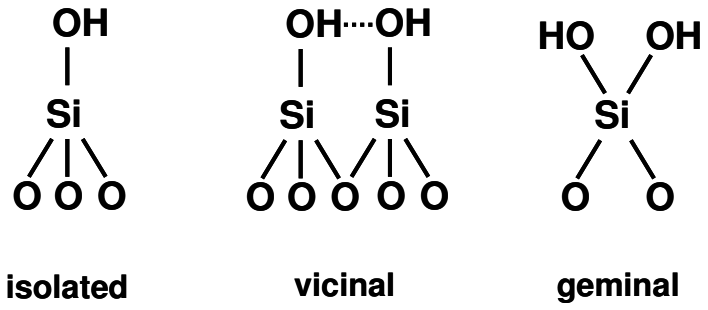

Fig. 1.1: Scheme of the different silanol group types

As the surface of amorphous silica is disordered, practically all three types of silanol groups can be found on the silica surface. The ratio depends on conditions like gas

pressure, temperature, and presence of water. Various experimental techniques like FTIR, NMR, the titration with hexamethylsilazane, and theoretical calculations show that the surface density of silanol groups can be considered as a physicochemical

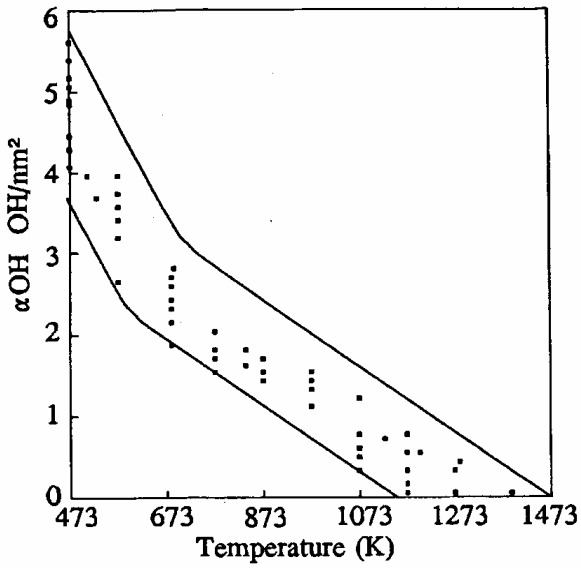

Fig. 1.2: Silanol density as a function of the temperature [27]

Table 1.2: Concentration of different silanol types as a function of treatment temperature in vacuum. [27]

Temperature (°C)	Total (OH/nm^2)	Isolated (OH/nm^2)	Vicinal (OH/nm^2)	Geminal (OH/nm^2)
200	4.60	1.15	2.85	0.60
300	3.55	1.65	1.40	0.50
400	2.35	2.05	0	0.30
500	1.80	1.55	0	0.25
600	1.50	1.30	0	0.20
700	1.15	0.90	0	0.25
800	0.70	0.60	0	0.10

constant, which is independent of the silica type. (Fig.1.2) Therefore, fully hydroxylated silica exhibits a silanol density of 4.6 OH/nm^2 at room temperature. As can be seen in table 1.2, the number of hydroxyl groups is decreasing rapidely to 2.3 OH/nm^2 up to a temperature of 400°C. At higher temperatures, the decrease is more slowly. A total removal of all silanol groups requires a temperature of 1200°C. [27]

The dehydroxylation behaviour depends to a small extent on the surface morphology of the silica, which has an influence on the number and the relative distribution of the silanol group types. For instance, small pores in the nanometer range exhibit a negative radius of curvature. Consequently, the distance between the silanol groups decreases and leads to a stronger interaction via hydrogen bonding, which is reflected by slower dehydroxylation. For small spherical particles, the opposite behaviour occurs. There the positive radius of curvature leads to a decrease of interactions between the silanol groups, as their distance is smaller. [27]

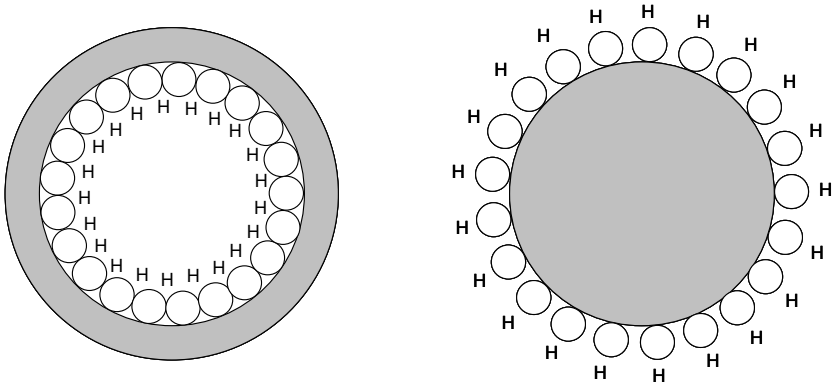

Fig 1.3: Effect of curvature on the hydroxyl distance; small pore (left), small particle (right)

1.3.2. Structure of Supported Molybdenum Oxide

The structure of silica supported dispersed molybdenum oxide is still a matter of debate in the literature. Therefore, the different published results regarding silica and silica

SBA-15 supported molybdenum oxide systems are summarized in the following. With regard to analytic methods mainly Raman, IR, UV-Vis, NMR and X-ray absorption techniques have been used to investigate supported molybdenum oxide structures. [28-38]

Based on the literature dispersed molybdenum oxide occurs depending on the method of preparation up to a density of 1.1 Mo/nm^2. At higher loadings, molybdenum oxide tends to form α-MoO_3 crystallites, due to weaker interaction with the silica support compared to titania or alumina. [39,40]

For the structure of dispersed molybdenum oxide, basically two different states, a hydrated and a dehydrated state have to be distinguished. Under ambient conditions, when the silica supported molybdenum oxide is exposed to atmospheric moisture, the hydrated state is present. While heating in dry synthetic air at elevated temperatures ($\geq$350°C), a conversion of the supported molybdenum oxide into a dehydrated state occurs, which is also stable at room temperature under anhydrous conditions. [41] As at low Mo densities catalytic activity is still observed and a simplification of the structure is expected, the discussion on the active structures has been focused on densities below 1.0 Mo/nm^2. [9,10]

A significant amount of research on this topic has been performed by Wachs and his coworkers. [10] For the hydrated state on the basis of XANES, Raman spectroscopy, and comparison with reference compounds, Wachs et al. concluded that for Cabosil supported molybdenum oxide at Mo densities of 0.2-0.8 Mo/nm^2 the surface structure consists in the hydrated state of polymolybdate clusters with $Mo_7O_{24}^{6-}$ and $Mo_8O_{26}^{4-}$ as the principal species. [28,29] The structure of the dehydrated state has been assigned on the basis of Raman and EXAFS results to a mixture of isolated dioxo and monooxo molybdenum oxide species. Di- and oligomeric species were excluded to be present at low molybdenum densities. [28,42]

Previously in the literature the presence of silico molybdic acid (SMA) as principle molybdenum oxide structure on silica was discussed. [41,43] Banares et al. showed that

SMAs are not stable at higher temperatures on silica supports and convert during dehydration to species, which are also obtained by other molybdenum oxide precursors like AHM. Moreover it was shown that SMAs are formed only in the presence of moisture at ambient temperatures. [41]

Oyama and his coworkers carried out a combined EXAFS / NEXAFS study supported by results from theoretical calculations and Raman spectroscopy. For Cabosil supported samples with 0.1 and 0.5 Mo/nm^2 loading it was concluded that the dispersed molybdenum oxide is present as a mixture of mono centres with tetrahedral dioxo and distorted octahedral geometry for the lower loading. For the higher loading, mono centres with tetrahedral coordination with traces of MoO_3 for the higher loading were reported. [30] Recently, Bell and his coworkers studied Silicycle supported molybdenum oxide (0.44 Mo/nm^2) with EXAFS, Raman spectroscopy and theoretical calculations and reported that the molybdenum oxide forms tetrahedral dioxo molybdenum oxide mono centres besides small amounts of pentacoordinated monooxo centres. [31-33]

The main argument for the exclusive presence of the molybdenum oxide mono centres on silica supports in the dehydrated state is based on the absence of a Mo-O-Mo mode, which is observed by Raman spectroscopy in the hydrated state. Additionally, the structure was assigned on the basis of quantum chemical calculations and comparison with molybdyl halogenides ($MoOF_4$, MoO_2Cl_2) as reference compounds. [28,31]

With regard to vanadia, a similar debate about the structure at low V densities is found in the literature. In the course of this debate a band at 950 cm^{-1}, that was assigned to the V-O-V mode, should indicate the presence of polymeric vanadia species. Magg et al. showed by theoretical calculations that the band is due to a vanadia-support interface mode (V-O-Support). [44] In contrast to alumina, for silica a strong mode coupling between the vanadyl (V=O) and the vanadia-support interface mode occurs. Consequently, the absence of a band at the position of the two coupled vibrations is no indication for the absence of polymeric vanadia species. [44] Furthermore, it has been

shown by analysis of NEXAFS, EXAFS and IR data that at low loadings at least dimeric interconnected vanadia centres beside monomeric centres are present. [45-47]
In contrast to the previous assignments, Ressler and coworkers examined SBA-15 supported molybdenum oxide (0.9 Mo/nm^2) by X-Ray absorption spectroscopy and reported that the structure of the molybdenum oxide shows similarities to hexagonal MoO_3 in the hydrated and dehydrated state. In addition, small amounts of crystalline α-MoO_3 were observed. [34,35] Also, Iwasawa and coworkers reported on the basis of EXAFS and H_2 reduction experiments that dimeric molybdenum oxide structures are present on silica supports for Mo densities of 0.1 and 0.3 Mo/nm^2. [48,49]
Furthermore, the results from UV/Vis spectroscopy show some contradiction with a structural picture based on the exclusive presence of monomeric species at low Mo densities. [42] Therefore, the structure assignment is performed by comparison with reference materials. On the one hand, for a tetrahedral monomeric reference material like Na_2MoO_4 absorption up to 280 nm is observed (see chapter 6). On the other hand, most silica supported molybdenum oxide systems at Mo densities ≤1.0 Mo/nm^2 show absorption ≥300 nm which can be seen as an indication that not only monomeric but also di- or oligomeric species are present. [50,51] Additionally, UV/Vis spectra frequently exhibit two bands at 240 and 280 nm. This supports the argument that additional species are present. [42,52,53]
The intention of this thesis is to contribute to the discussion about the molybdenum oxide structures present on silica supports at *ex* and *in situ* conditions. Therefore, results by EXAFS, *in situ* Raman spectroscopy and new techniques for the structure assignment of supported molybdenum oxides like the adsorption of nitric oxide probe molecules and detection of neighbouring molybdenum oxide structures by IR spectroscopy [54] as well as O K-edge NEXAFS are used to investigate supported molybdenum oxide structures.

1.4. Selective Oxidation of Propylene

The selective oxidation of propylene to acrylic acid is not possible by simple thermal activation, as consecutive oxidation of intermediate products is kinetically and thermodynamically favoured. [5] Additionally, the binding energy of C-C bonds (246 kJ/mol) is lower compared to C-H bonds (363 kJ/mol) so that the C-C bond cleavage is favoured by thermodynamics. [55] Therefore, catalysts have to be employed to control the reaction kinetics and change the selectivities in the desired way as illustrated in Fig. 1.4. This can be achieved by a limitation of oxygen and electron storage capacity in the active sites and therefore requires site isolation on the catalyst surface. [56] These requirements are for example matched by dispersed molybdenum oxides at low loadings ($\leq$1.0 Mo/nm^2) on inert silica supports.

On heterogeneous oxide catalysts, the selective oxidation can either be performed by activated electrophilc oxygen ($O\cdot^-$, O_2^{2-} and $O_2\cdot^-$) or by nucleophilic oxygen (O^{2-}). which is stored on the catalyst surface. The nucleophilic oxygen can stem from deeper lattice layer like in heterogenous bulk oxide catalysts and diffuse to the surface or can be formed at defect sites on the catalyst surface. [57] For propylene it is largely accepted that selective oxidation proceeds with nucleophilic oxygen [58], while oxidation by electrophilic oxygen attacks electron rich parts of the substrate molecule like π-bonds and leads to a degradation of the carbon skeleton and total oxidation by C-C bond cleavage. The distribution of nucleophilic and electrophilic oxygen depends on the temperature and also the catalyst structure. [58] Therefore it is an interesting question how the absence of bulk molybdenum oxide in supported molybdenum oxide systems influences the ratio of nucleophilic and electrophilic oxygen.

For the oxidation by nucleophilic oxygen essentially two mechanisms have to be distinguished. The first one is the Mars van Krevelen mechanism [59], which proceeds in two steps: (I) the propylene molecule is activated on the catalyst surface and the

lattice oxygen inserts into the molecule. Afterwards, the oxygenated product desorbs and leaves a partially reduced catalyst with oxygen vacancies at the surface. Then (II) the catalyst is reoxidized and the vacancies are refilled with oxygen from the gas phase,

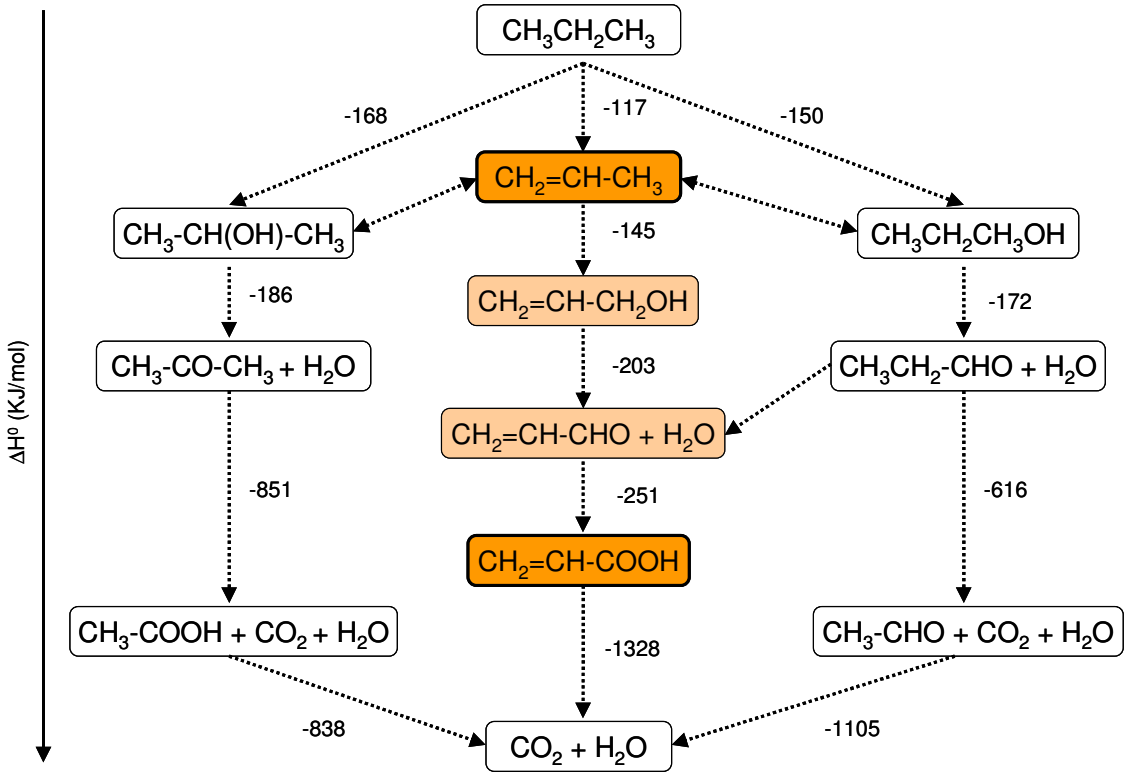

Fig 1.4: Propane oxidation pathway and calculated standard reaction enthalpies [5]

resulting in the restorage of the inital state. As the reduction and oxidation are considered to be separated steps, this mechanism can be called a redox mechanism. [60] As second possibility, the reduction and oxidation step may occur in a concerted transformation, which is called push-pull mechanism. [58]

2. Experimental

2.1. Raman Spectroscopy

The Raman spectra were measured using an argon ion laser (Melles Griot) at 514 nm and a helium neon laser at 632 nm for excitation. For detection a transmissive spectrometer equipped with a Pelletier CCD detector operated at -40°C was used (Kaiser Optical, HL5R). The spectral resolution was about 5 cm^{-1}. The laser power was 6 mW as measured at the position of the sample. The powder samples were introduced into a sample holder made of stainless steel with a bed size of 12 x 8 mm and a depth of 0.6 mm. The Raman spectra of the dehydrated sample were recorded at room temperature after a treatment at 300°C for 30 min in synthetic air. The accumulation time for the spectra was typically 30 min.
The samples used for EXAFS-Spectroscopy were measured in an *in situ* Raman cell operated at 500°C in synthetic air with a flow of 50 ml/min. For these experiments the Mo_xO_y/SBA-15 was pressed at 70 MPa and sieved to obtain a particle size in between 250 and 355 µm. The spectra accumulation time was 120 min.
The Raman spectra will be presented at an excitation wavelength of 514 nm as long as not indicated otherwise.

2.2. The *in situ* Raman-MS Setup

2.2.1. Introduction

In the course of this work a coupled Raman-MS-test setup was constructed for the *in situ* examination of the Mo_xO_y/SBA-15 catalysts. A schematic overview of the setup is

given in Fig. 2.1. With the setup it is possible to produce defined gas mixtures and to direct them through the catalyst bed at temperatures up to 500°C. Changes of the catalyst structure can be followed with Raman spectroscopy and reaction products simultaneously analyzed by mass spectrometry. Moreover, the setup composed of a saturator unit, Raman chamber and mass spectrometer unit is designed in a modular and mobile way. This allows to assemble the components in relative short time and to use single modules separately for other applications.

2.2.2. Construction Details on the Setup

For the construction of the setup (Fig. 2.1) 1/8 inch gas pipes and standard Swagelok components in U.S. customary units have been used. The gas mixtures necessary for the experiments can be premixed in various ratios in a fixed gas mixing station with mass flow controllers from Bronckhorst allowing gas flow rates between 0 to 200 ml/min. Nitrogen dioxide, nitrogen, oxygen and propane/propylene are available as gases. In addition, the nitrogen can also be used as a rinsing gas for the nitrogen dioxide pipes to prevent corrosion. Furthermore the saturation of nitrogen with water and other liquid reactants can be done in the saturator unit, which will be described in chapter 2.2.4. To prevent condensation of educts and products all pipes starting at the saturator unit are heated to 130°C while operation of the setup. To this end, the pipes have been wrapped with HS-450 heating bands and covered for heat isolation with BCTEX tissue tape (2 x 25 mm).

The plywood made Raman chamber is the spectroscopic part of the setup. It contains the probe head equipped with an objective and the *in situ* Raman cell which is installed into a heating block. Reaction products from the *in situ* Raman cell are directed towards the mass spectrometer unit. The insertion into the mass spectrometer is performed by a

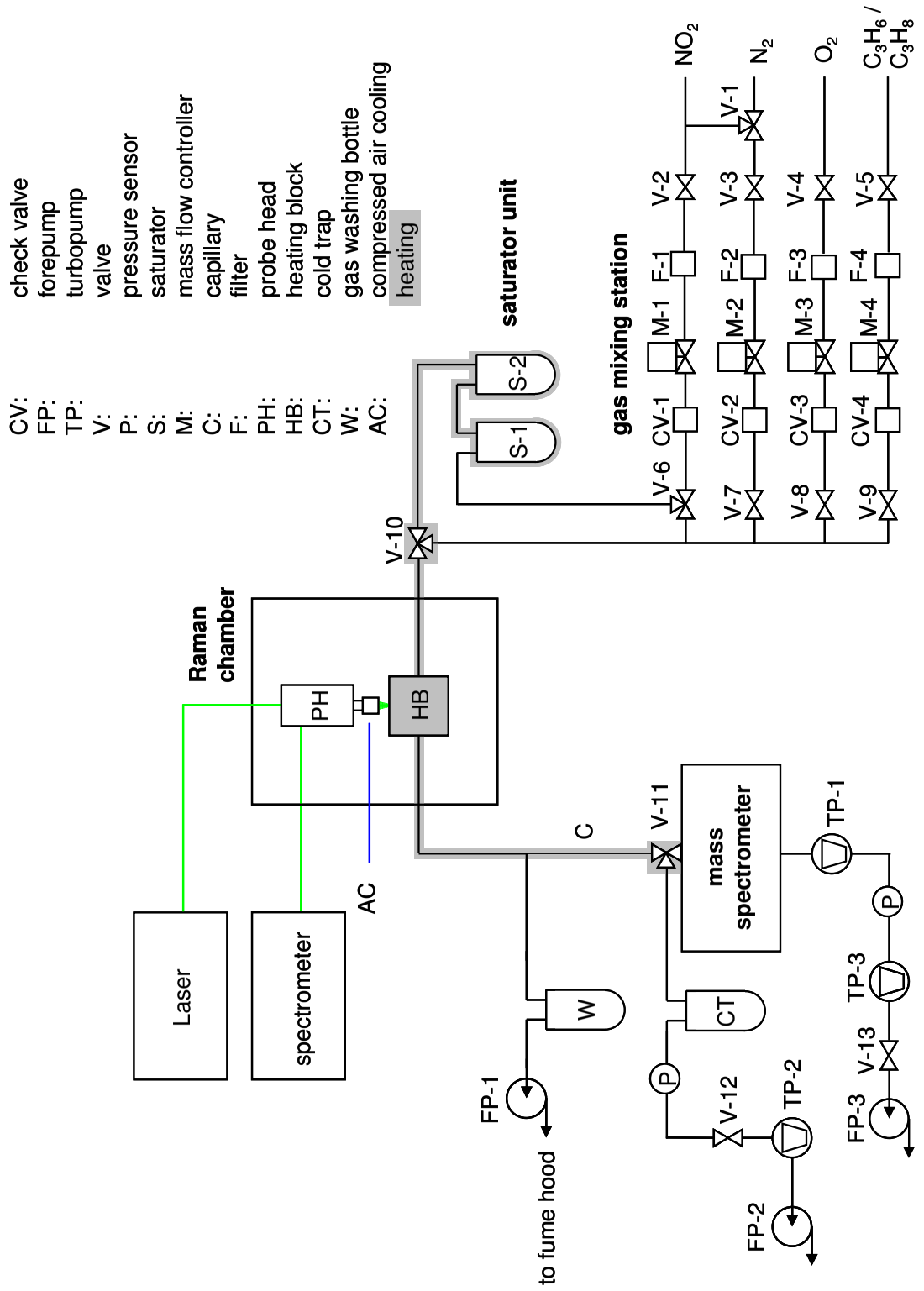

Fig. 2.1: Scheme of the *in situ* Raman setup

polymer enhanced glass capillary from SGE Analytical Science of 1200 mm length and 0.2 mm inner diameter. Product gas, which is not passed through the capillary to the mass spectrometer, is directed into a gas washing bottle and then into the fume hood. To oxidize harmful reaction products like acrolein the gas washing bottle is filled with a mixture of diluted phosphoric acid and potassium permanganate.

The product gas being sucked through the capillary has a residual pressure of 10^{-1} to 10^{-2} mbar. The inlet into the analysis chamber of the mass spectrometer (Pfeifer QMS200) is provided by a fine dosage valve from Pfeiffer (UDV 140) which makes it possible to adjust the pressure very precisely in a pressure range of 10^{-9} to 10^{3} mbar. For the measurements a pressure between 10^{-6} and $5 \cdot 10^{-6}$ mbar was used.

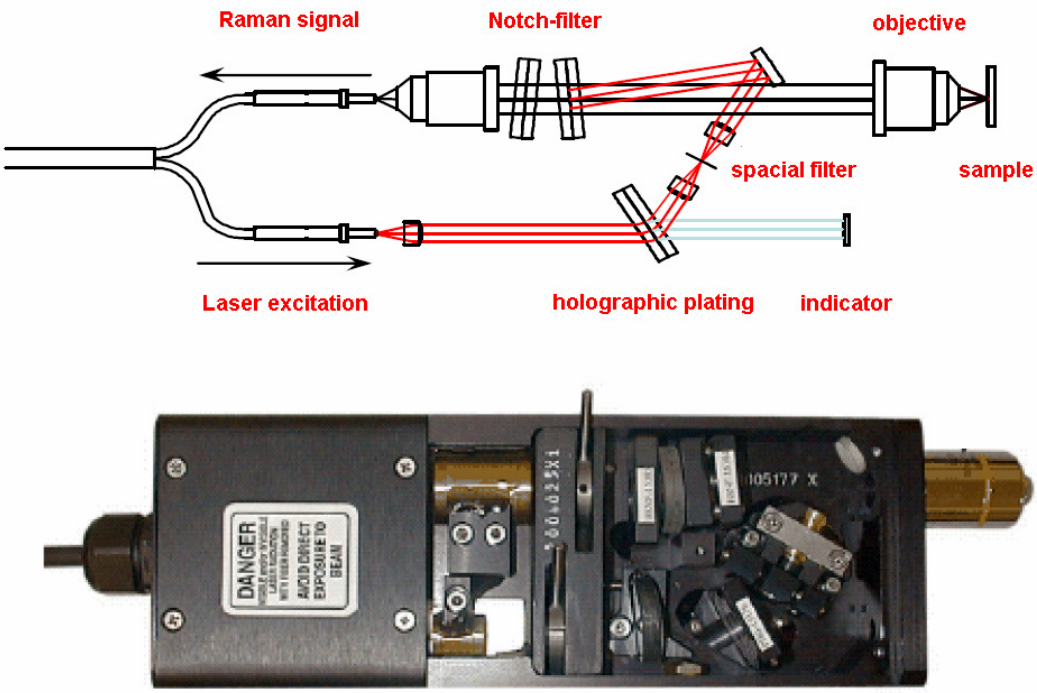

Fig. 2.2: Scheme (top) and picture (bottom) of the probe head

2.2.3. The *in situ* Raman Setup

For the excitation of the Raman process a helium-neon laser (633 nm) or an argon ion laser (488 / 514 nm) can be used, which were typically operated at a laser power of 6 mW measured at the sample. To this end the laser beam was coupled into a glass fibre optics and directed to the probe head. (Fig. 2.2) In the probe head the light was first cleaned from background signals which originate form the passage through the fibre optics by optical grating and spacial filters. Afterwards the light is redirected with

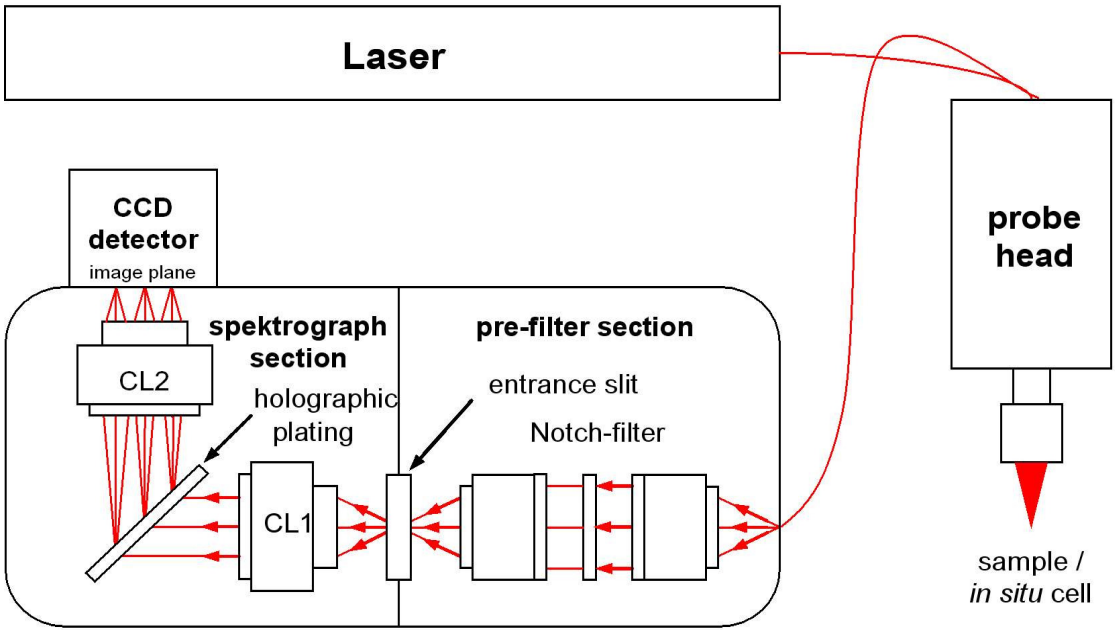

Fig. 2.3: Scheme of the Raman spectroscopic setup

mirrors towards the objective (Olympus SLMPlan N, 20x , NA = 0.25 , f = 25 mm). The diameter of the focussed laser beam was about 1.0 µm. Subsequently, the Rayleigh line of the elastically backscattered light was removed with notch filters. The residue inelastically scattered light was focused on the entrance of a glass fibre, which connects

the probe head with the spectrograph. In the pre-filter section of the spectrograph again residue Rayleigh light is removed by a notch filter and spatially restricted when passing through the entrance slit. Then the light rays are parallelized by the collimator lens CL1 and afterwards splitted by a holographic grating to obtain a spectrum which is projected by a second collimator lens CL2 onto the image plane of the CCD camera. To enhance the spectral resolution the camera was cooled by Pelletier elements to -40°C.

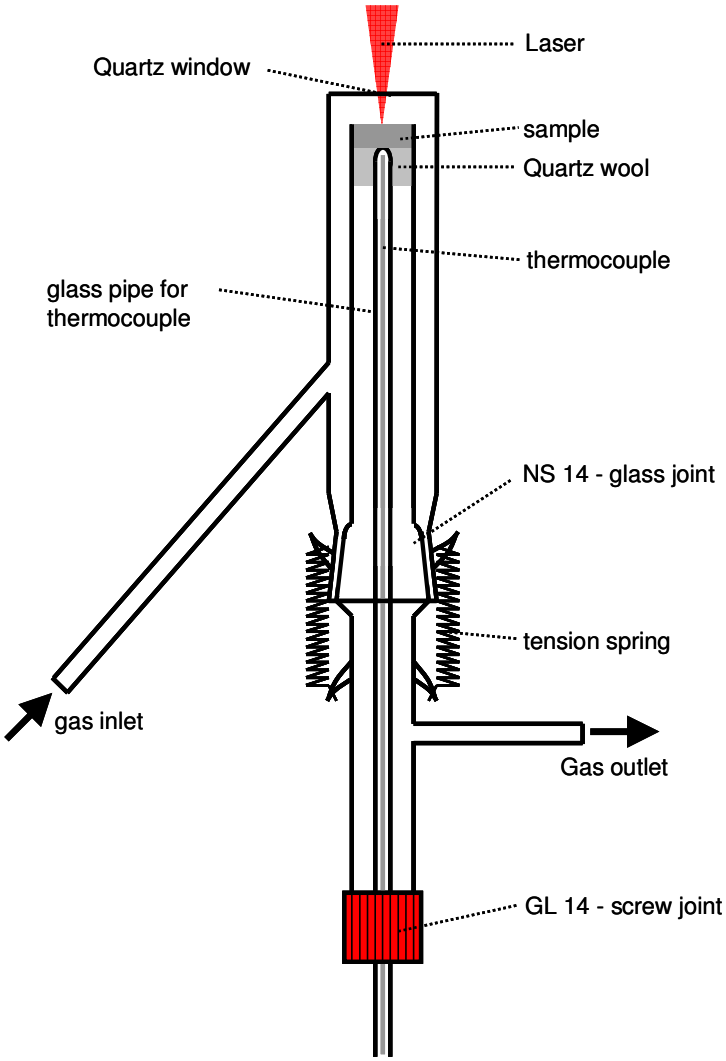

Fig. 2.4: Scheme of the *in situ* Raman cell

2.2.4. The *in situ* Raman Cell

The *in situ* Raman cell being used for the experiments (Fig. 2.4) was made of quartz glass. The outer diameter of the upper part is 17 mm and that of the gas in- and outlet 6 mm. The window for Raman spectroscopy on top of the cell was made of quartz glass with 1 mm thickness for optical applications. The outer diameter of the inset was 10 mm and was connected to the upper part of the cell by a NS 14 glass joint, which was held together by two tension springs.

For the glass to metal cross-over of the gas in- and outlet pipe teflon sealed, twistable joints were used. The bottom of the inset is sealed with a GL 14 screw joint, which contains a sealing disc with a hole. A glass pipe with 4 mm outer diameter, which is sealed on top, has been stuck through the sealing disc. It contains the thermocouple (Ø 0.5 mm, company Jumo) and protects it while the Raman cell is operated.

For the sample bed in the upper part of the inset 50 mg of catalyst with a particle size of 250 to 355 µm have been used. Beneath quartz wool was put to hold the catalyst in position. The thermocouple was placed directly under the catalyst bed.

2.2.5. The Heating Block

The heating block for the *in situ* Raman cell consists of two halves (90 x 100 x 30 mm) which have been screwed together and are made of aluminium. Every half of the heating block contains a bore passing through the hole half. In each bore a heating cartridge of HS-Heizelemente (60 mm x 6.5 mm, 350 W) is installed. For heat shielding during operation shielding plates made of stainless steel with 0.5 mm thickness were installed on the top and on the sides with a distance of 2 and 4 mm to the surface of the

heating block. During operation the setup can be used at any temperature between 25 and 500°C.

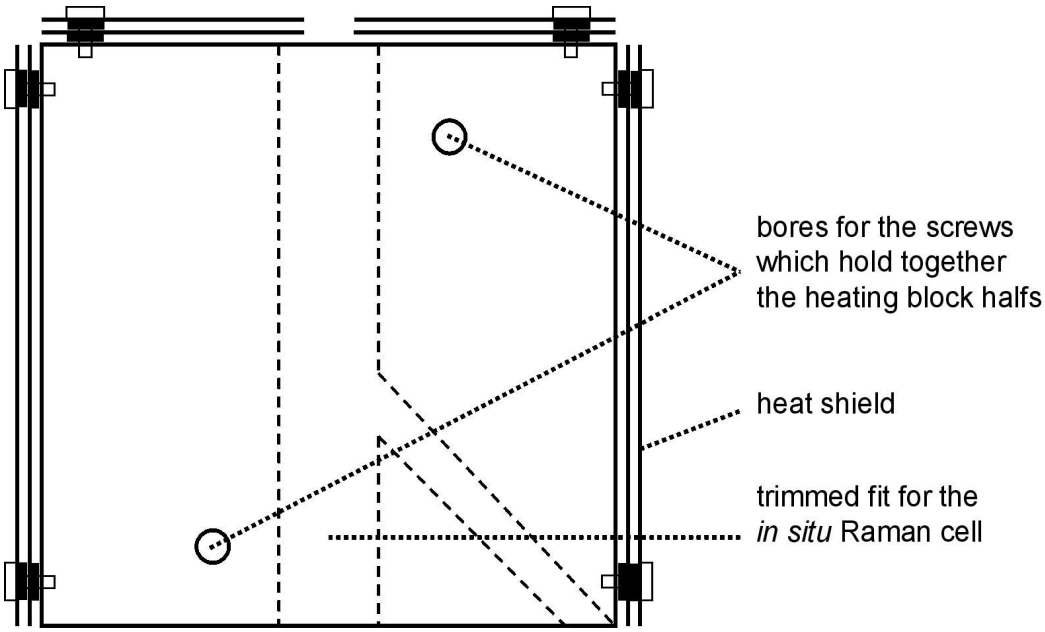

Fig. 2.5: Front view of the heating block

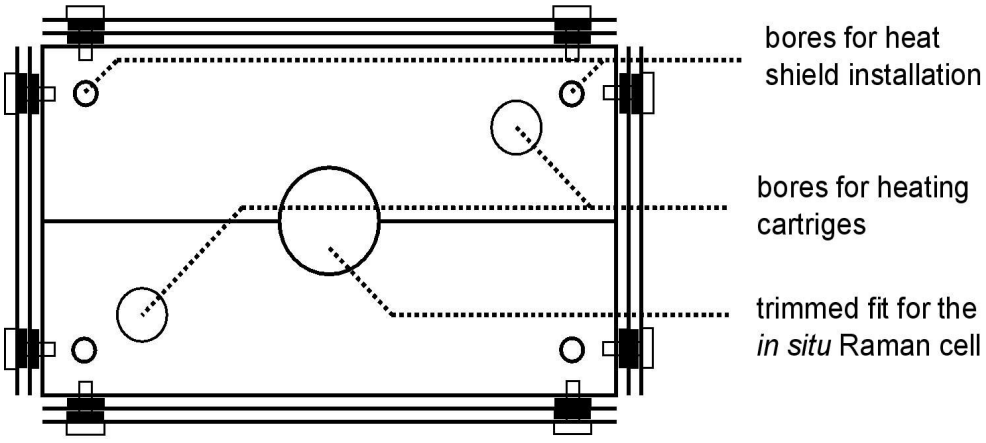

Fig. 2.6: Top view of the heating block

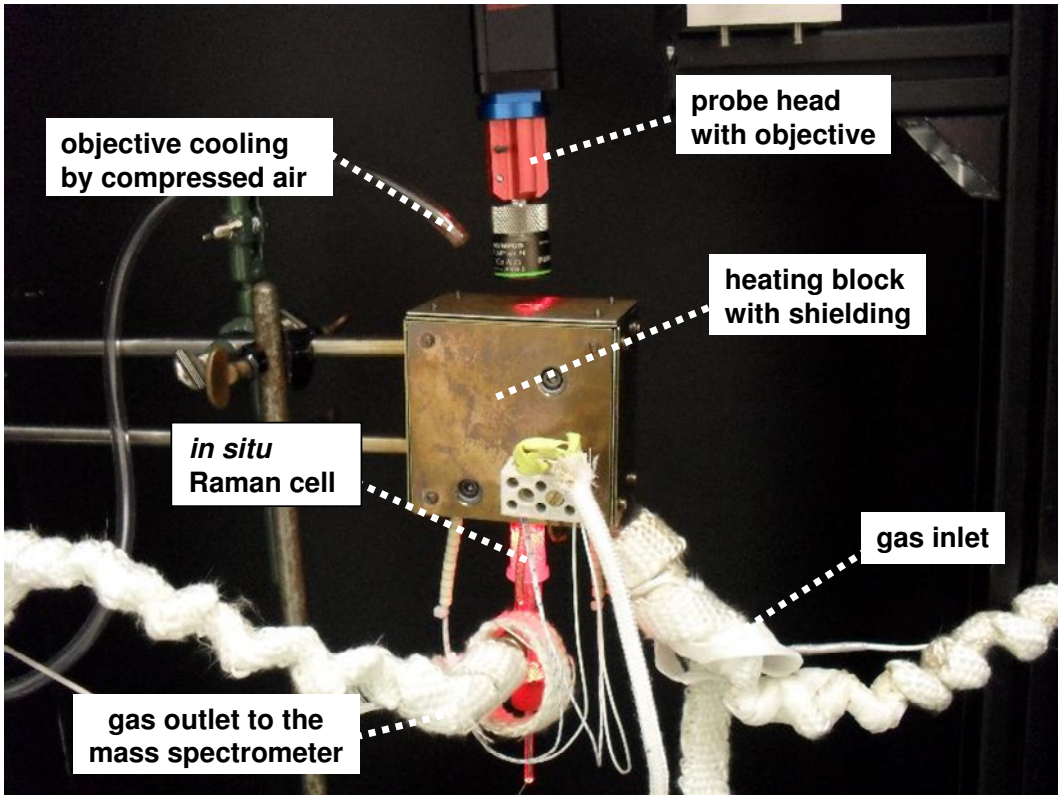

Fig. 2.7: *In situ* Raman setup in operation

2.2.6. The Saturator Unit

The saturator unit consists of two similar saturators (Fig. 2.8), which have been constructed in the glass workshop of the chemistry department of the TU-Darmstadt. The saturators have a diameter of 100 mm and a height measured at the outlet valve of 200 mm. The cooling cylinder has an inner diameter of 70 mm and a thickness of 6 mm. On top of the saturator four GL 14 screw joints, two in- and two outlets, for nitrogen and the liquid saturation medium (e.g. water) are attached to the inner and outer cylinder of the saturator. To ensure the gas tightness during heating the metal to glass cross-over was established with special screw joints made of polyphenylensulfide (PPS) and sealing rings made of polytetrafluorethylene (PTFE) from Bola.

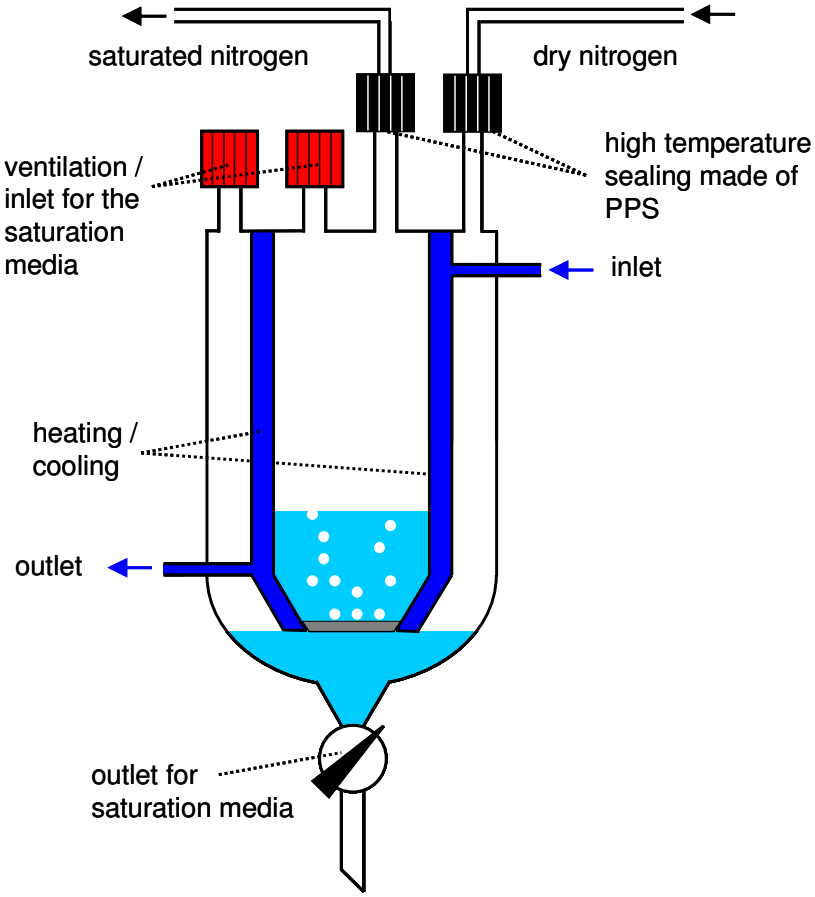

Fig. 2.8: Scheme of the Saturator

Both saturators (Fig. 2.9) have been mounted onto a metal rack, which was fixed on a mobile table module. The heat isolation of the saturators was done by BCTEX fleece and glass textile tape (25 mm) of the company Horst. On the ground plate of the table module two bath thermostats were placed for thermostatisation of the saturators. If water was used, the saturators were operated in the following way: The pre-saturator (Fig. 2.9 right) was heated to a slightly higher temperature than the second saturator ($\Delta T = 3$ K). In that manner the nitrogen was slightly higher saturated in the pre-saturator

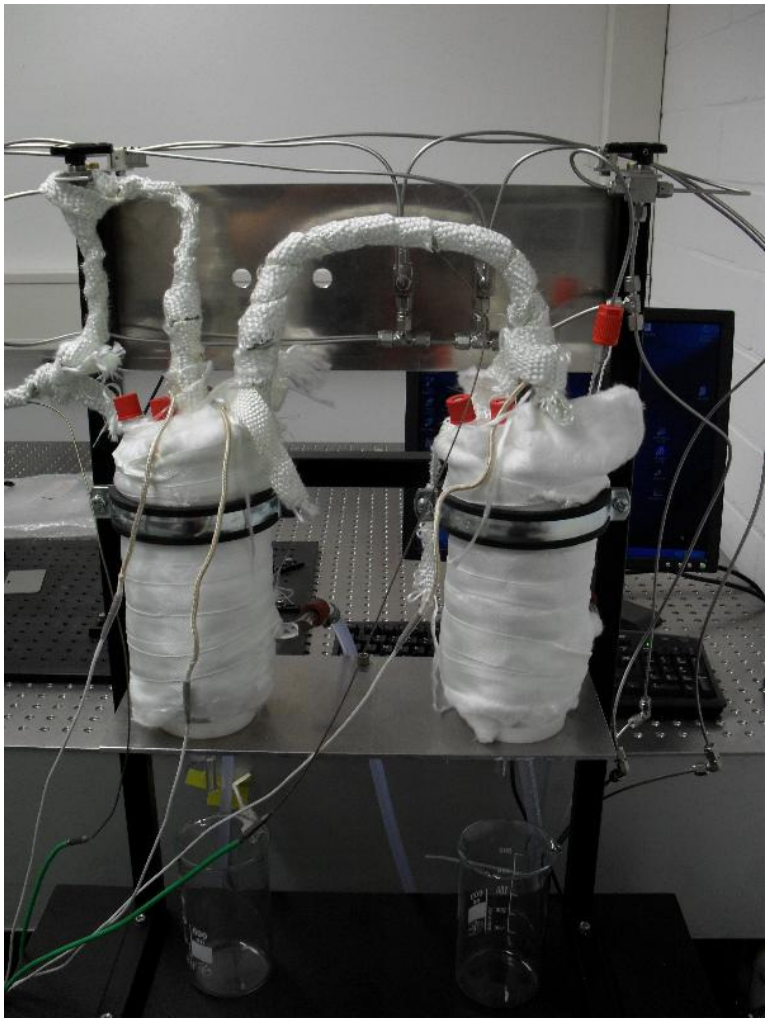

Fig. 2.9: Saturator installed on a rack with heat isolation in operation

and the desired saturation level was set in the second saturator (Fig. 2.9 left). To reach a saturation level of 50% the temperature of the second saturator was set to 83°C. [61] For the pre-saturator a heating bath thermostat of Fisherbrand (FBH604, 20 to 120°C) has been used. In contrast to that for the second saturator a bath thermostat, which can be used for heating and cooling from Huber (CC2-K6, -25°C to 200°C) was employed. This has the advantage that beside water as saturation medium also other volatile intermediate products of the propane/propylene oxidation like acetone, propionaldehyde or acrolein can be fed into the Raman cell in low concentrations (<5 vol.%).

2.3. FTIR Spectroscopy

FTIR spectra were measured using a Perkin-Elmer PE 100 spectrometer with a resolution of 4 cm^{-1} and 32 scans per spectrum. The samples were pressed at 10^4 kPa to obtain self-supporting wafers. They were treated in a transmission IR cell, which could be evacuated to a residual pressure of 10^{-7} kPa. The samples were evacuated at 673 K for 1 h before the adsorption measurements. For reduction, they were heated with 5 K/min to 673 K in 50 kPa hydrogen for 1 h, evacuated at the same temperature and left for cooling. For oxidation, the same procedure was performed but 50 kPa oxygen was used instead of hydrogen. The adsorption of ^{14}NO or ^{15}NO (Linde, 99,5%) with O_2 was done at room temperature. The D_2O (Aldrich, 99,9%) exchange was performed in the IR cell by cyclic treatment of the sample at 300°C with 6 mbar D_2O vapor for 1 h followed by evacuation. Background spectra were generated by taking spectra of the evacuated empty cell equipped with CaF_2 windows. Difference spectra were obtained by subtracting the spectrum of the sample in vacuum before the experiment from spectra collected during the experiment.

2.4. X-Ray Absorption Spectroscopy

Transmission XAS experiments were performed at the Mo K edge at beamline X at the *Hamburg Synchrotron Radiation Laboratory*, HASYLAB, using a Si(311) double crystal monochromator (measuring time ~4 min/scan). *In situ* experiments were conducted in a flow-reactor at atmospheric pressure (5 vol.% oxygen in He, total flow ~30 ml/min, temperature range from 300 K to 773 K, heating rate 4 K/min). The gas phase composition at the cell outlet was continuously monitored using a non-calibrated

mass spectrometer in a multiple ion detection mode (Omnistar from Pfeiffer). Reference oxides were mixed with boron nitride (~7 mg each with 30 mg BN) while SBA-15 materials (~50 mg) were used as-is. Powders were pressed with a force of 1 ton into a 5 mm in diameter pellet resulting in an edge jump at the Mo K-edge of $\Delta\mu_x \sim 1$.

X-ray absorption fine structure (XAFS) analysis was performed using the software package WinXAS v3.2. [62] Background subtraction and normalization were carried out by fitting linear polynomials to the pre-edge and 3rd degree polynomials to the post-edge region of an absorption spectrum, respectively. The extended X-ray absorption fine structure (EXAFS) $\chi(k)$ was extracted by using cubic splines to obtain a smooth atomic background $\mu_0(k)$. The $FT(\chi(k)\cdot k^3)$, often referred to as pseudo radial distribution function, was calculated by Fourier transforming the k^3-weighted experimental $\chi(k)$ function, multiplied by a Bessel window, into the R space.

EXAFS data analysis was performed using theoretical backscattering phases and amplitudes calculated with the ab-initio multiple-scattering code FEFF7. [63] Structural data employed in the analyses were taken from the Inorganic Crystal Structure Database (ICSD). Single scattering and multiple scattering paths in the hexagonal MoO_3 (hex-MoO_3) model structure were calculated up to 6.0 Å with a lower limit of 4.0% in amplitude with respect to the strongest backscattering path. EXAFS refinements were performed in R space simultaneously to magnitude and imaginary part of a Fourier transformed k^3-weighted and k^1-weighted experimental $\chi(k)$ using the standard EXAFS formula. [47] This procedure strongly reduces the correlation between the various XAFS fitting parameters. Structural parameters allowed to vary in the refinement were (i) disorder parameter σ^2 of selected single-scattering paths assuming a symmetrical pair-distribution function and (ii) distances of selected single-scattering paths. The statistical significance of the fitting procedure employed was carefully evaluated [64] according to procedures recommended by the *International X-ray Absorption Society* on criteria and error reports. [65] First, the number of independent parameters (N_{ind}) was calculated according to the Nyquist theorem $N_{ind} = 2/\pi \cdot \Delta R \cdot \Delta k + 2$. In all cases the

number of free running parameters in the refinements was well below N_{ind}. Second, confidence limits were calculated for each individual parameter. [64] Third, a so-called F test was performed to assess the significance of the effect of additional fitting parameters on the fit residual. [66]

2.5. NEXAFS

The *in situ* NEXAFS measurements were performed at the BESSY (Berliner Elektronenspeicherringgesellschaft für Synchrotronstrahlung) synchrotron radiation facility using monochromatic radiation of the ISISS (Innovative Station for *In Situ* Spectroscopy) beamline as a tuneable X-ray source. In the presence of oxygen at elevated temperature the high pressure X-ray absorption spectra were obtained using the high pressure endstation, which was constructed and designed at the FHI. Details about the setup are described elsewhere. [67-69] The Mo_xO_y/SBA-15 samples were pressed into pellets of 8 mm diameter (1t/6min) and some reference compounds as suspension in chloroform on a steel plate. The pressed pellets were heated in 0.5 mbar O_2 from RT to 350°C with 5K/min. Data was recorded while holding min. 30 min at 350°C until H_2O MS-signal reached the baseline. The Auger Electron Yield (AEY) spectra were obtained in 0.5 mbar O_2. Two sets of data have been taken with different kinetic energy windows of the analyzer. The pass energy was about 100 eV. Using a monochromator the energy range of the O K-edge was scanned in a continuous mode with a constant speed (250 meV/s). The typical scan time for the whole region was approximately 5 min to reduce the impact of the X-ray beam on the sample. Typically 3 scans have been averaged and the spot position was changed after every scan. The amount of data points was reduced from 4000 points per scan in the range of 520 to 560 eV by a factor 6. Additionally, for reconstruction the data were pre-edge normalized to 1 and corrected for variations in the photon flux by absorption in the gas phase as described in detail in [45].

The photon energy calibration was done with a simultaneously recorded O_2 gas phase spectrum. When no gas phase was present the calibration was done with features in the M4 mirror current. The absolute energy calibration should be within 0.2 eV for the π^* of O_2 taken at 530.93 eV.

2.6. UV/Vis Spectroscopy

The diffuse reflectance UV/Vis spectra were measured using a Perkin-Elmer Lambda 950 spectrometer, which was equipped with a Harrick diffuse reflectance attachment and reaction chamber. The optical system consisted of a tungsten-halogen and a deuterium light source, a holographic grating monochromator with 1440 lines/mm UV-vis and a photomultiplier R6872 for the entire UV/Vis wavelength range as detector. Measurements have been taken in the range of 200 to 800 nm.
The samples were dehydrated by heating with 10 K/min up to 450°C in 20% O_2 and 80% N_2. Spectra were taken after cooling down to room temperature. During the heating spectra were recorded in 5 min intervals with the PerkinElmer UV WinLab 5.2.0 software. $BaSO_4$ was used as white standard.

2.7. Nitrogen Adsorption

The SBA-15 samples were pretreated overnight in vacuum at 80°C and then measured on Quantachrome Autosorb-1 and Autosorb-6B instruments. The total pore volume was determined from the adsorption branch of the N_2 isotherm curve at a relative pressure of $p/p_0 = 0.95$. A standard isotherm was measured with 80 data points. For the calculation of the surface area a nitrogen cross section of 13.5 $Å^2$ was used [70]. The pore-size distribution was calculated from the adsorption and desorption branch of the isotherm

using the NLDFT method and its FWHM determined by fitting with a Gaussian function. The micropore surface area was calculated at p/p_0 values from 0.3 to 0.45 with the t-plot method by de Boer [71].

2.8. X-Ray Diffraction

Low angle X-ray diffraction (XRD) measurements were performed on a conventional (i.e. wide angle) STOE STADI P transmission powder diffractometer, equipped with a primary focusing Ge monochromator (Cu $K\alpha_1$ radiation) and scintillation counter. In order to enhance the accuracy of the 2θ scale, a measurement mode with two symmetric scans (negative and positive 2θ) was chosen. Small amounts of powdered sample were sandwiched between two layers of polyacetate film and fixed with a small amount of X-ray amorphous grease. This sandwich was clamped into a sample holder ring, which was rotated around the primary beam axis.

At low angles, small differences in 2θ result in significant errors on the d-spacing scale. Thus, the diffractions patterns were evaluated using correlated fitting of the asymmetric diffraction peaks. An asymmetric instrumental function was convoluted with a symmetric Voigt function representing the sample contribution. A common lattice parameter *a* and a common 2θ offset (zero error) was refined on the 100, 110 and 200 peaks of the two-dimensional hexagonal lattice for both scan ranges (negative and positive) simultaneously. Due to the internal 2θ calibration based on the symmetric scan mode and correlated fitting, the instrumental zero error can be determined with high precision, yielding a more reliable determination of the a_0 lattice parameter in turn. Thus, this procedure allows a robust and reproducible evaluation of the d-values of differently treated samples. However, it needs to be kept in mind that both due to the asymmetric peak shape and the strongly asymmetric background, these values will depend strongly

on the evaluation procedure applied. Thus, care should be taken when comparing the results of different studies on an absolute scale.

2.9. X-Ray Photoelectron Spectroscopy

The XPS measurements were performed on a modified LHS/SPECS EA200 MCD system which was equipped with a Mg Ka source (1253.6 eV, 168 W). The powder samples were placed on a sample holder with a rectangular deepening of 12 x 8 x 0.6 mm made of stainless steel. The deepening was completely filled to obtain a plain surface. For dehydration the sample was heated in a special chamber (lock chamber) of the setup to 350°C for 30 min in synthetic air at a flow rate of 50 ml/min. The lock chamber can also be used to measure Raman spectra. Afterwards the sample was evacuated stepwise and transferred into the analysis chamber (base pressure $1 \cdot 10^{-9}$ to 10^{-10} mbar) for the measurement. The typical recording time for a spectrum was 40 min. The obtained data was analyzed by the SciPlot 3.9n software. With this software satellite subtraction and Shirley background subtraction was performed. To compensate charging effects the binding energy of the Si2p peak as reference was set to 103.6 eV. The whole spectrum was normalized to the area of the Si2p peak. Peak fitting using 30/70 Gauss-Lorentz product function was performed.

2.10. Catalysis Setup

The catalysis tests were performed in a setup constructed at the Fritz Haber Institut. The reactor consisted of a quartz tube with a inner diameter of 6.8 mm, which is heated electrically from outside and possesses an isothermal zone of 40 mm. Furthermore, the reactor was placed in a drying oven heated to 140°C. For the catalysis tests 0.25 or 1.0 cm^3 of catalyst with a particle diameter of 250 to 355 µm were filled into the reactor and

sealed on both ends with quartz wool plugs. The dosage of the feed gases propane, propylene, oxygen and nitrogen was controlled by standard mass flow controllers from Bronkhorst. Furthermore it was also possible to add steam into the feed mixture by a evaporator unit and a syringe pump from Harvard Apparatus. The detection of the products was performed by a GCMS system (5975 B, Agilent Technologies). The device contained two DB1 columns for the separation of the oxygenates, which were detected by mass spectrometry. The separation of the other gases (propane, propylene, CO, CO_2, H_2O, O_2 and N_2) was performed by a Haysep Q, a Plot Q and a Plot Molesieve column and detected with a thermal conductivity detector.

3. SBA-15

3.1. Formation of SBA-15

For the synthesis of ordered mesostructured silica materials nanostructured templates are required. Those templates can be formed, for instance, by defined aggregations of surfactant molecules, which are called micelles. Surfactant molecules are amphiphil and possess a hydrophilic polar headgroup and a lipophilic non-polar tail. In aqueous

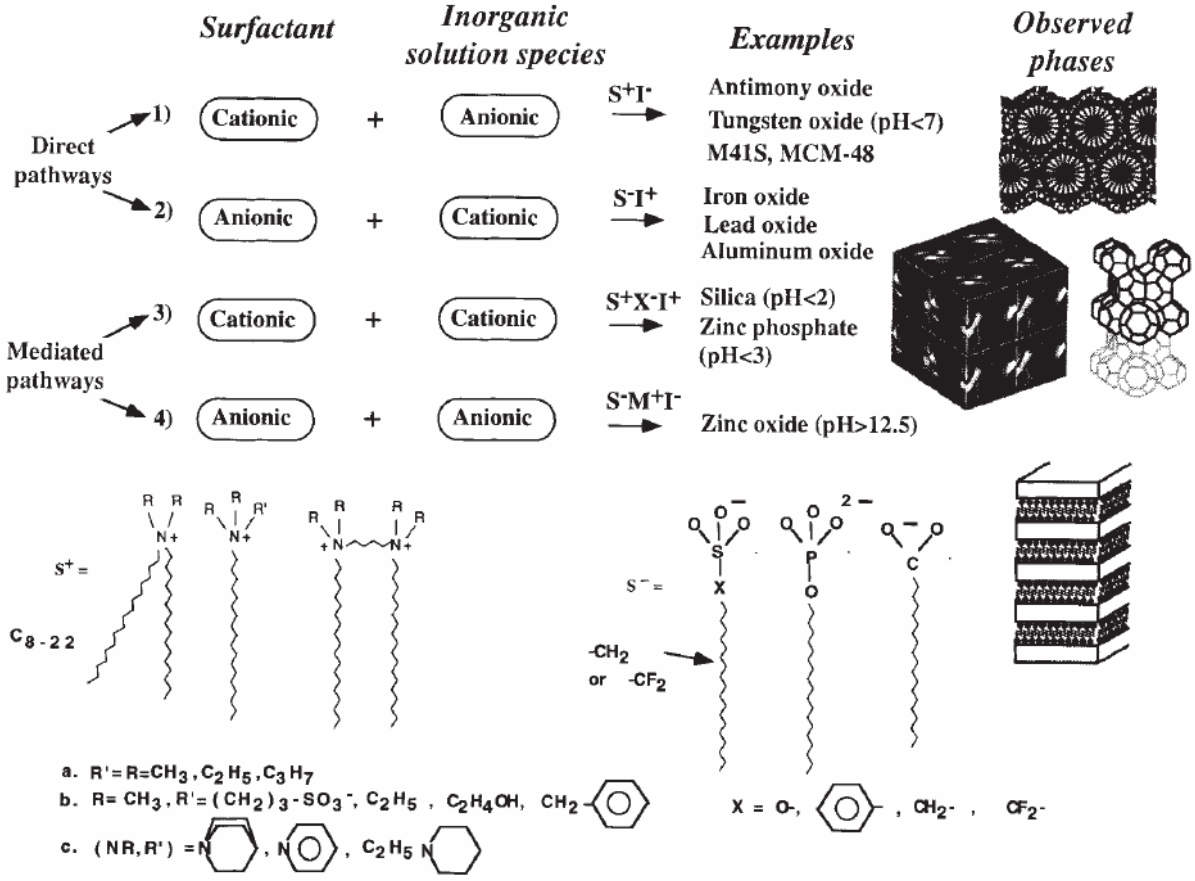

Fig. 3.1: General scheme for the self-assembly reaction of different surfactants and inorganic species [72]

solutions micelle formation occurs at a critical surfactant concentration. At that point the lipophilic tails start to stick together and form the core of the micelle while the polar head groups are located outside towards the polar solvent. The shape of the micelles can be rod- or bilayer-like depending on tail length to headgroup area ratio, salt and surfactant concentration in the solution, pH and temperature. The micelles may also interact. Then bigger self-organized mesostructures are formed, which can be used as templates for nanostructured materials. [73,74]

A general approach for the formation of ordered surfactant/inorganic composite materials was suggested by Huo et al.. [72] The self-assembly can either occur on direct pathway by the interaction of the surfactant and the inorganic species (S^+I^- or S^-I^+) or can be mediated by a small ions of opposite charge ($S^+X^-I^+$ or $S^-X^+I^-$) (see Fig. 3.1).

In the synthesis of silica SBA-15 Pluronic 123 a triblock copolymer consisting of ethylene oxide and propylene oxide units ($EO_{20}PO_{70}EO_{20}$) is used as surfactant. The propylene oxide units of the polymere forms the lipophilic part of the surfactant, while the ethylene oxide units form the hydrophilic part. Zhao et al. proposed that the self-assembly of the SBA-15 proceeds in acidic media according to the $(S^0H^+)(X^-I^+)$ mechanism. [24] At first ethoxysilane species are hydrolyzed followed by a partial oligomerization at the silica.

$$Si(OEt)_4 + nH_3O^+ \xrightarrow[pH<2]{\text{hydrolysis}} Si(OEt)_{4-n}(OH_2^+)_n + n\text{EtOH}$$

The EO surfactant moieties are associated with hydronium ions in strong acidic media.

$$REO_m + y\text{HX} \xrightarrow{H_2O} REO_{m-y}[(EO) \cdot H_3O^+]_y \cdots yX^-$$

The moiety R consists of poly(propylene oxide) and the counterion X^- is in the case of hydrochloric solutions as acidic media Cl^-. The assembly of the protonated EO units and the cationic silica species occurs by a combination of electrostatic, hydrogen bonding

and van der Waals interaction $REO_{m-y}[(EO)H_3O+]_y \cdots yX^- \cdots I^+$, which can be designated as $(S^0H^+)(X^-I^+)$. [24]

3.2. Pore Structure of SBA-15

Beside the mesoporous structure SBA-15 also exhibits micropores, which have been explored by several research groups. [75-82] Imperor-Clerc et al. for instance studied microporsity of SBA-15 with N_2 adsorption, TEM and small angle XRD. By application of models to fit the XRD data it was found that the silica density at the pore walls is lower than in deeper layers of the SBA-15 structure. The area of lower silica density is called corona (Fig. 3.2) and is supposed to originate from the hydrophilc PEO-units of the triblock copolymer template, which penetrate into the silica walls during the synthesis of the SBA-15 structure. [77]

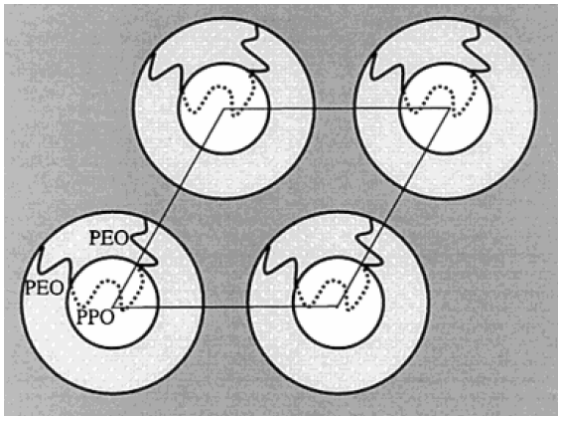

Fig. 3.2: Schematic picture of uncalcined SBA-15. [77]

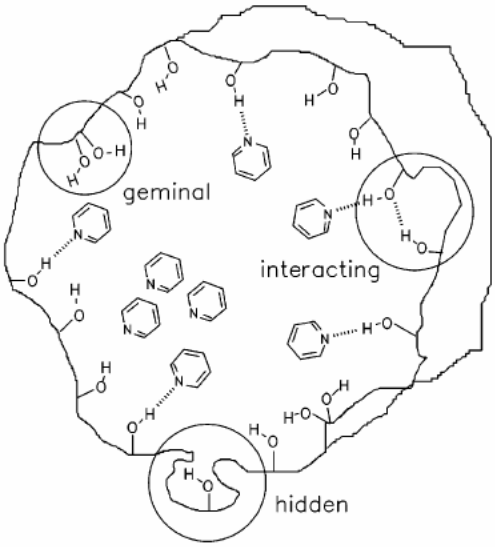

Fig. 3.3: Pore model for SBA-15 exhibiting a rough inner surface probed by solid state NMR employing ^{15}N-pyridine. [78]

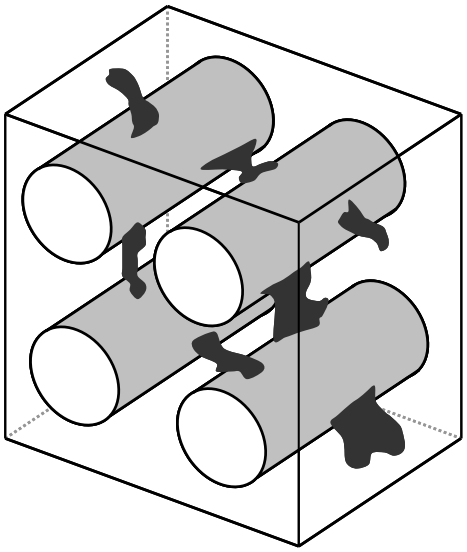

Fig. 3.4: Scheme of the three dimensional pore structure of SBA-15 [79]

Furthermore, Ryoo et al. reported the synthesis of stable carbon [75] and platinum [76] replicas of SBA-15, which shows that some micropores penetrate the hole silica wall and interconnect the mesopores. (Fig. 3.4)

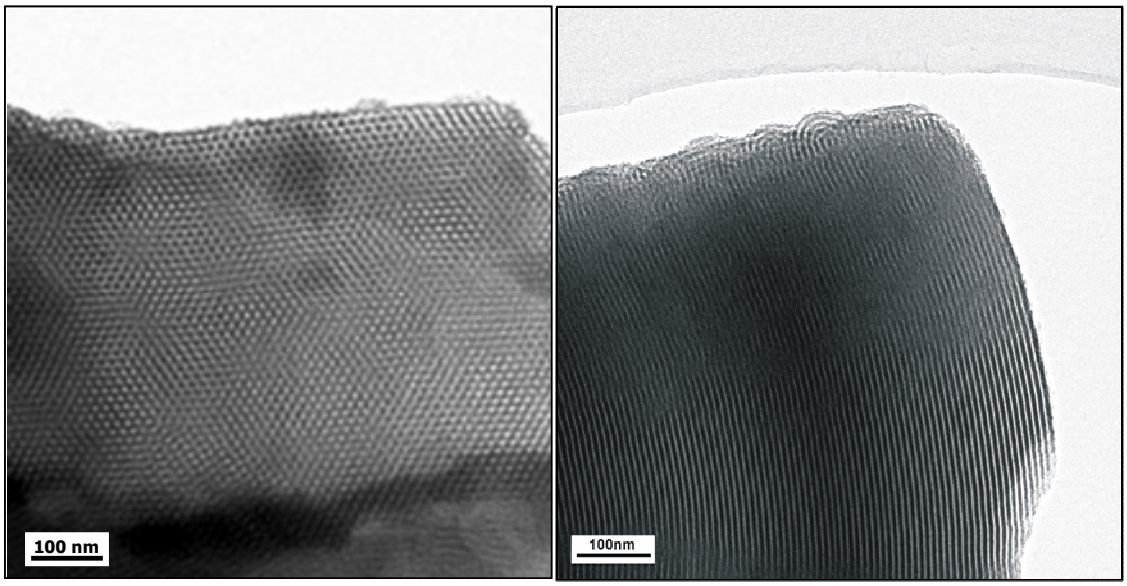

Fig. 3.5.: The TEM images show the hexagonal pores (right) and the longitudinal channels (left) of a SBA-15 particle.

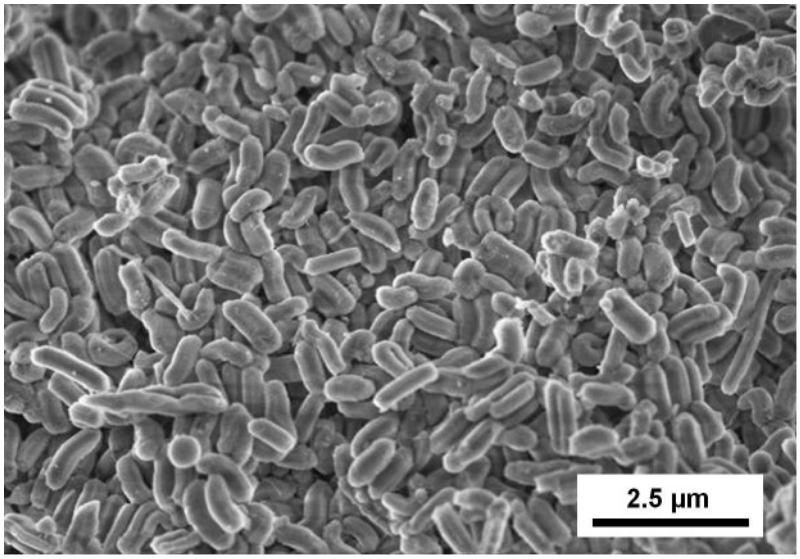

Fig. 3.6: SEM image of the SBA-15 particles

Additionally, Shenderovich et al. showed by solid state NMR using ^{15}N labelled pyridine as probe molecule, that SBA-15 has a rougher surface than MCM-41, which is another mesoporous silica material. (Fig. 3.3) [78]

Fig. 3.5 shows TEM images of the hexagonal pores and the longitudinal channels of SBA-15 structure. The shape of the SBA-15 particles can be described as rice grain like, which are often stuck together in groups. As shown in Fig. 3.6 the particles possess a diameter of approximately 0.5 µm and a length of 1 µm.

However, not all details of the SBA-15 structure and the factors influencing the synthesis are fully understood. Therefore, in the next sections the removal of the triblock copolymere template from the freshly prepared SBA-15 structure by washing and the scale up of the synthesis will be discussed.

3.3. Influence of Washing and Scale Up on to the Pore Structure and Surface Area of Silica SBA-15

3.3.1. Introduction

The removal of the surfactant template ($EO_{20}PO_{70}EO_{20}$) by washing before final calcination is a critical step in the synthesis of silica SBA-15, as it can influence the micro- and mesostructure of the final product and is therefore addressed in this chapter.

In the literature various methods are described to remove the template, which can be performed for instance by calcination [23,24], washing [83,84], reflux extraction [23,24], acid [85] or H_2O_2 treatment [86], extraction with supercritical CO_2 [87] and microwave digestion [88]. The washing described after the synthesis is mostly done using only pure solvent like water [89], acetone [90] or ethanol [91,92]. According to Bae et al. using ethanol instead of water is three times more effective to remove the template from the SBA-15 framework. Although the Pluronic 123 can not be removed completely from the SBA-15 by washing, as shown by thermogravimetric analysis (TGA) [93]. Also the more effective template removal by ethanol is connected with a shrinkage of the SBA-15 structure as observed by Ko et al. [83].

In the literature no reports on SBA-15 synthesis using a washing approach with two solvents are to be found. In the following it will be shown that the use of two solvents while washing can lead to an increase of the surface area and that for small batches the volume of the solvents has an impact on surface area and pore size distribution of SBA-15. Also the influence of scale up to 27 g per batch on the properties of SBA-15 is discussed. So far the largest synthesis scale is reported by Tkachenko et al. corresponding to approximately 24.5 g [94].

Chapter 3.3. is organized as follows: Paragraph 3.3.2. describes the synthesis of SBA-15. In paragraph 3.3.3. the influence of washing freshly synthesized SBA-15 with water or ethanol is discussed. Paragraph 3.3.4. deals with a combinational washing approach using water and ethanol. Particular emphasis is put on the effect of the solvent quantities being used while washing. Paragraph 3.3.5. addresses the issue of scaling up the SBA-15 synthesis to 9 times the size described in the original procedure by Zhao et al.. [23,24]

3.3.2. Synthesis of SBA-15

3.3.2.1. Synthesis

4.07 g Pluronic 123 were dissolved at 35°C in 30 ml distilled water and 120 ml 2M hydrochloric acid in a perfluoralkoxylalkane (PFA) bottle. Afterwards 9 ml of tetraethoxysilane (TEOS) were added and the mixture was stirred (600 rpm) at 35°C for 20 h in the closed bottle. The formed white suspension was then aged at 85°C for 24 h without stirring. After cooling to room temperature the copolymer was removed by washing with distilled water and/or ethanol using a G4 frit. The product was dried at room temperature over night and was then heated up to 550°C in 6 h and calcined for 12 h in static air. Afterwards the product was carefully grinded and characterized by N_2 adsorption.

The FWHM and intensity maxima of the pore size distribution were determined by fitting with a Gaussian function. Furthermore, the batches were also increased in size (3x, 9x), as compared to the size described in the literature. [23,24] These batches will be referred to as 3x or 9x batches. When they are divided into two smaller batches they will be named 3x or 9x half-batches. The yield for a 1x, 3x and 9x batch was 2.5 g, 7.5 g and 25 g SBA-15. The residue carbon content of the SBA-15 determined by

elementary analysis after calcination was independent of batch size and washing procedure only 0.09 % at maximum.

3.3.2.2. Details of the Washing Procedure

Two batches produced under the same synthesis conditions can still show small variations regarding surface area, pore volume and pore size distribution, which makes it difficult to study the pure effect of washing. The absolute surface area and pore volume may deviate from batch to batch by ±5 percent. For the pore size distribution this deviation is about ±2 percent. To overcome this problem, a batch or scaled up batch was divided into two identical half-batches and a small, unwashed reference sample of approximately 80 mg. The weight of the reference samples is negligible compared to the two half-batches, which are used for the washing experiments.

Table 3.1: Typical contact times while washing

SBA-15 sample	Washing procedure [a]	contact time (min) water	ethanol	water
3 A	no washing	0	0	0
B	5 ml ethanol / water (1x halfbatch)	2	2	2
C	35 ml ethanol / water (1x halfbatch)	6	6	6
D	120 ml ethanol / water (3x halfbatch)	15	10	11
E	350 ml ethanol / water (9x halfbatch)	60	30	27

[a] Solvent volume is given per washing cycle.

The washing was always performed 15 times with a defined quantity of solvent, which was poured on to the sample in the G4 frit at 25°C and subsequently removed by suction during each washing cycle. Furthermore, the sample was carefully stirred with a glass stick after each solvent addition. The combined washing approach consisted of washing with defined quantities of water (5x), ethanol (5x) and again water (5x). In the case where only pure solvent was used (section 3.3.3.) the amount of each solvent quantity and the total number of washing cycles (15x) was comparable to the combined washing approach. In table 3.1 typical contact times of the solvents for each washing step with dependence on the batch size are given.

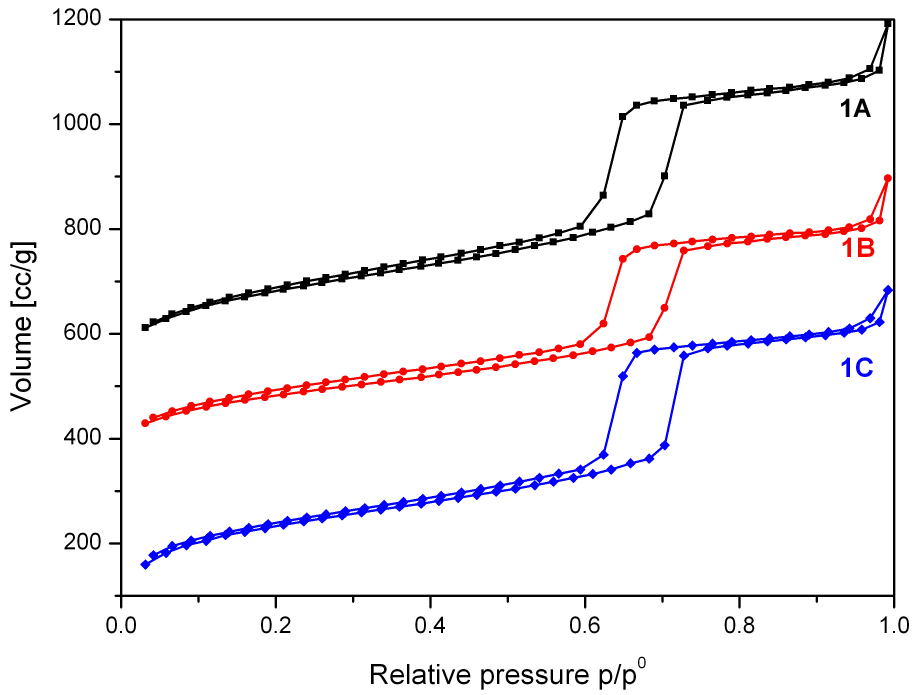

Fig. 3.7: N_2 adsorption/desorption isotherms of SBA-15 unwashed (**1A**), after washing with 30 ml ethanol (**1B**) and 30 ml water (**1C**). The isotherms are offset by 450 (**1A**) and 300 (**1B**) cc/g.

3.3.3. Template Removal by Washing with a Single Solvent

The removal of the Pluronic 123 template ($EO_{20}PO_{70}EO_{20}$) by washing prior to calcination is a crucial step in the SBA-15 synthesis. Therefore, a series of experiments has been conducted to understand first the effect of each solvent (water, ethanol)

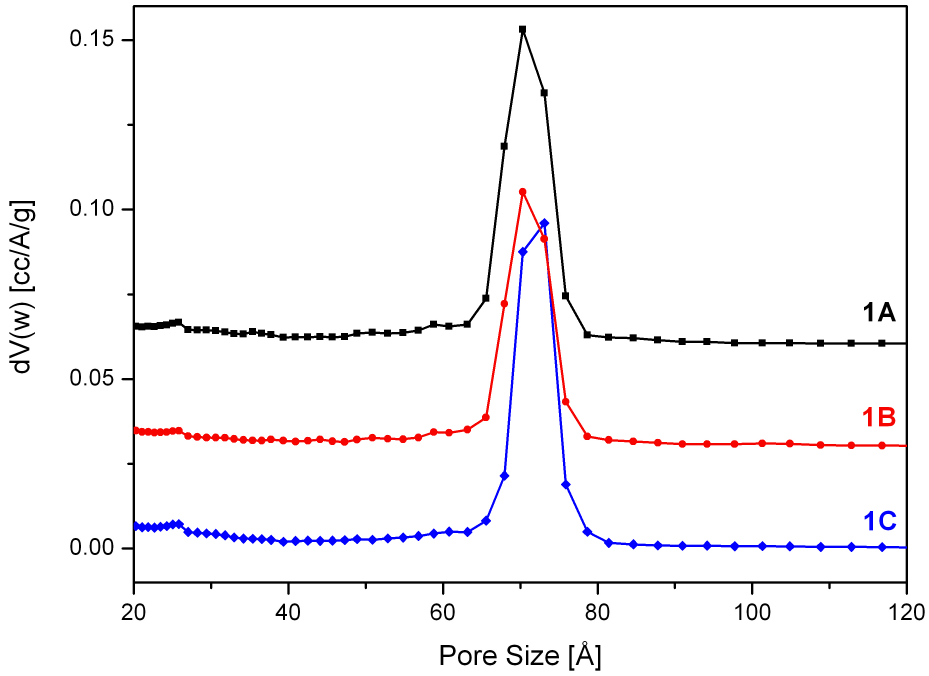

Fig. 3.8: NLDFT pore size distributions of SBA-15 unwashed (**1A**), after washing with 30 ml ethanol (**1B**) and 30 ml water (**1C**) calculated from the adsorption branch of the isotherm. The pore size distributions are offset by 0.06 (**1A**) and 0.03 (**1B**) cc/A/g.

separately and then the effect of a combination of these two solvents (discussed in section 3.3.4.) while washing. To investigate the batch size dependence while washing with a single solvent a 9x batch was separated into two 1x half batches and two 3x half

batches. As the results for both half batches are similar only the 1x half-batch will be discussed in the following.

The shape of the isotherms of sample **1** (see Fig. 3.7) is almost ideal type IV and no change of the hysteresis is observed with different washing procedures. This means that the homogeneity and order of the hexagonal pores is not altered by washing. The surface area and the pore volume of the untreated reference sample **1A** and the water treated sample **1C** is nearly the same, whereas the surface area and pore volume of the ethanol treated sample **1B** is significantly reduced by 150 m^2/g and 0.2 cm^3/g. The shrinking of pore volume and surface area while washing with pure ethanol seems to be due to more efficient removal of the surfactant from the meso- and micropores than with pure water [83]. The shrinking also affected the ratio between micro- and mesopores.

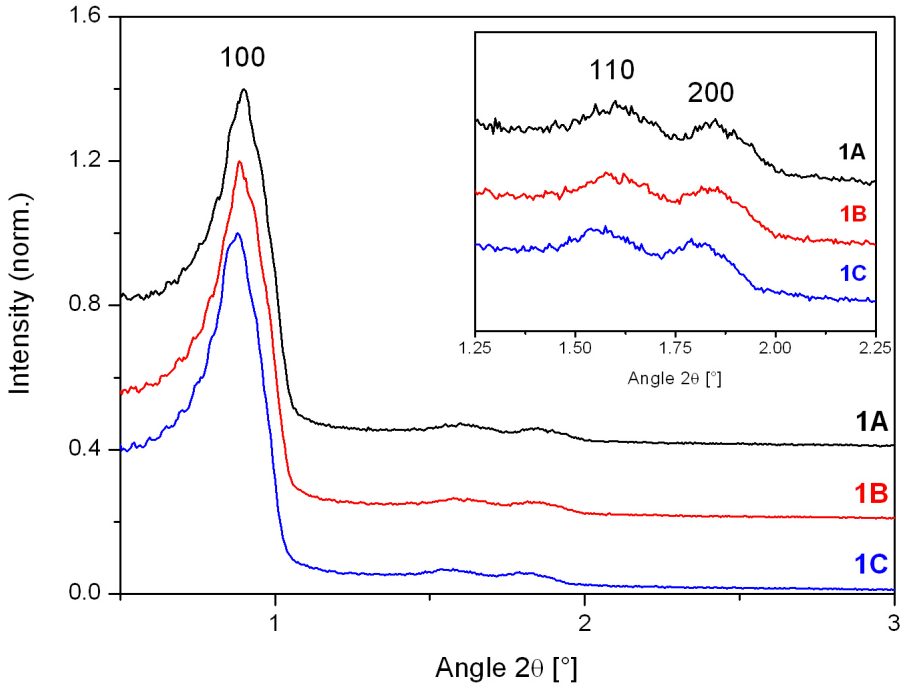

Fig. 3.9: Small angle XRD of SBA-15 unwashed (**1A**), after washing with 30 ml ethanol (**1B**) and 30 ml water (**1C**). The intensities are normalized to the 100 reflex and offset by 0.4 (**1A**) and 0.2 (**1B**).

The ethanol washed sample **1B** exhibits more and the water washed sample **1C** less micropore volume and surface area than the non washed reference samples **1A** (see Table 3.2).

Figure 3.8 depicts the pore size distributions of the adsorption branch of the isotherm for the three samples, which are quite similar. The pore size distributions are characterized by a maximum at 70 Å (sample **1A, 1C**) and 73 Å (sample **1B**) and a FWHM of 8 Å is observed. The high order of the mesopores is also corroborated by XRD results (see Fig. 3.9). Independent of the washing procedure the 100, 110 and 200 reflexes occur at almost the same position and the same relative intensity.

Table 3.2: Surface and porosity characteristics of SBA-15 samples washed with pure water, ethanol and a combination of ethanol and water

SBA-15 sample		washing procedure [a]	S_{Micro} (m^2/g) [b]	S_{Total} (m^2/g) [c]	S_{Micro}/S_{Total} [d]	D_p (Å) [e]	a_0 (Å) [f]	a_0-D_P (Å) [g]	V_{Total} (cm^3/g) [h]
1	**A**	no washing	263	700	0.38	70	108	38	0.98
	B	30 ml ethanol	300	551	0.52	73	110	37	0.78
	C	30 ml water	213	709	0.30	70	108	38	0.94
2	**A**	no washing	267	671	0.40	68	107	39	0.88
	B	5 ml ethanol / water	381	817	0.47	70	109	39	1.01
	C	30 ml ethanol / water	215	573	0.38	61	100	39	0.62
3	**A**	no washing	297	758	0.39	70	111	41	0.88
	B	5 ml ethanol / water (1x halfbatch)	389	872	0.45	70	107	37	1.11
	C	35 ml ethanol / water (1x halfbatch)	343	755	0.45	68	109	41	0.87
	D	120 ml ethanol / water (3x halfbatch)	354	790	0.45	70	109	39	0.96
	E	350 ml ethanol / water (9x halfbatch)	364	838	0.43	70	111	41	1.06

[a] Solvent volume used per washing cycle.
[b] Micropore surface area.
[c] Total BET surface area.
[d] Fraction of the micropore surface area of the total BET surface area.
[e] Pore diameter determined from the adsorption isotherms by the NLDFT method.
[f] Unit-cell parameter (a_0) determined from small-angle XRD.
[g] Pore wall thickness estimated by subtracting the pore diameter value (D_P) from the hexagonal unit-cell dimension (a_0).
[h] Total pore volume.

3.3.4. Influence of Combinational Washing with Ethanol and Water

In contrast to the washing with pure solvent the combined washing with ethanol and water may lead to an increase of surface area (see Table 3.2), but also damages the material. The damage is observed as a bulge in the desorption branch of the BET isotherm. To investigate the possible sources for this decreased homogeneity of the pores the following potential influences on the synthesis were examined and excluded: (i) temperature in the first synthesis step a) by exact temperature stabilization at 35°C and avoidance of any temperature fluctuations b) by increasing the synthesis temperature to 37°C, (ii) variation of the addition velocity of tetraethoxysilane (TEOS), (iii) stirring velocity while synthesis and TEOS addition, (iv) heating rate and temperature fluctuation at the aging step (85°C), (v) influence of the cooling rate after aging, (vi) tightness of the bottle while aging and (vii) influence of grinding [26] after synthesis. Van der Voort et al. and Kruk et al. report that an increased TEOS/surfactant ratio (viii) can influence the structure of the SBA-15. Therefore the TEOS/surfactant ratio has been fixed to 58:1 for all samples to exclude it as source for the observed disorder. [95,96]

Importantly, it was found that only the amount of solvent used in the washing process has a significant influence on the shape of the isotherm of the final product (see Fig. 3.10).

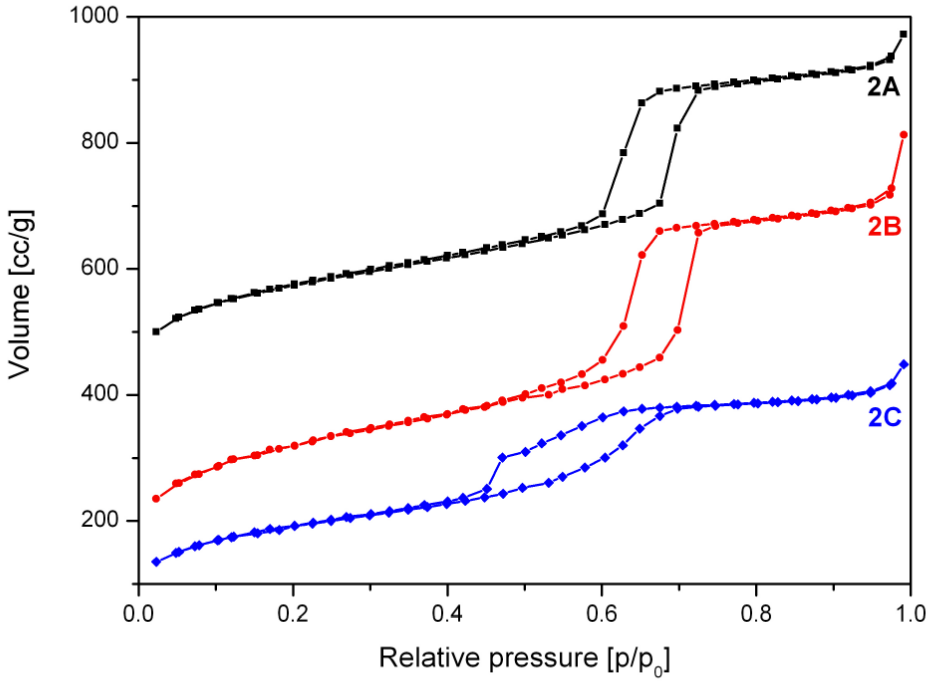

Fig. 3.10: N_2 adsorption/desorption isotherms of SBA-15 unwashed (**2A**), after washing with 5 ml (**2B**) and 30 ml (**2C**) quantities of solvent. The isotherms are offset by 350 (**2A**) and 50 (**2B**) cc/g.

To gain insight into the influence of solvent volume, a single batch (sample **2**) was split into two half batches. At first, a reference sample **2A** of 80 mg, which was not washed, has been taken before splitting into two half-batches. One of the half-batches was gently washed with 5 ml (**2B**) and the other one with 30 ml (**2C**) of solvent. All samples were subsequently calcined at 550°C. The resulting samples were analyzed regarding BET surface area, pore size distribution and pore volume (see Fig. 3.11, Fig. 3.12 and Table 3.2).

The reference sample **2A**, which has not been washed shows the best isotherm hysteresis and a narrow pore size distribution (FWHM: 9 Å) calculated from the adsorption branch of the isotherm (see Fig. 3.11 and Table 3.2). In comparison to the other two samples the gently washed sample **2B** shows a significantly increased surface

area and a narrow pore size distribution (FWHM: 9 Å) with a maximum at 70 Å. In contrast sample **2C** washed with plenty of solvent shows a significantly changed shape of the isotherm with a bulge in the desorption branch at 0.45 p/p_0 as well as a reduced surface area compared to sample **2B**.

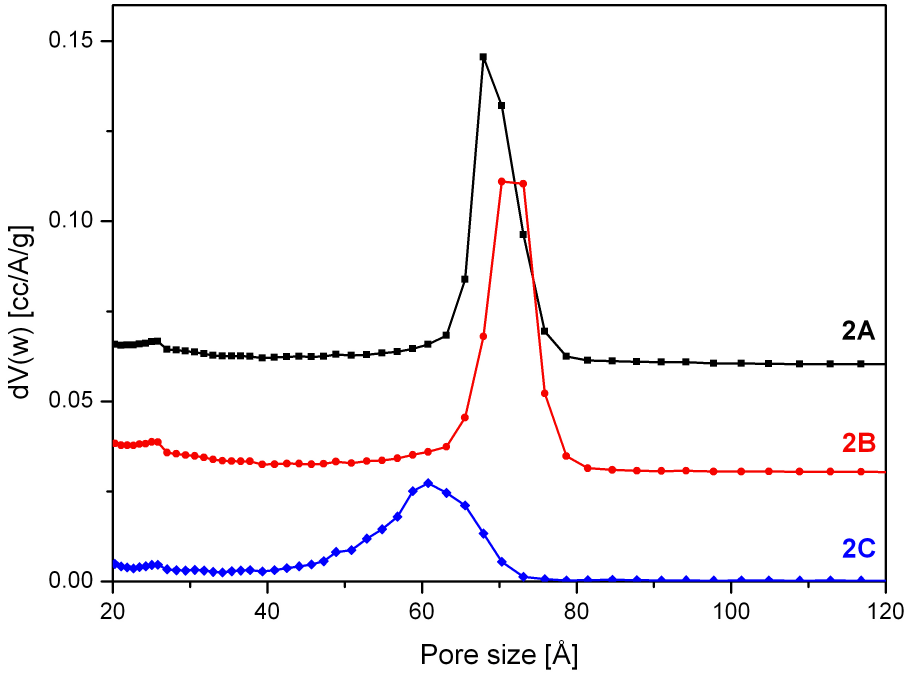

Fig. 3.11: NLDFT pore size distribution of SBA-15 unwashed (**2A**), after washing with 5 ml (**2B**) and 30 ml (**2C**) quantities of solvent calculated from the adsorption branch of the isotherm. The pore size distributions are offset by 0.05 (**2A**) and 0.025 (**2B**) cc/A/g.

The closure of the hysteresis loop at p/p_0 values between 0.4 and 0.45 for sample 2C can be explained by the tensile strength effect [97,98]. The effect occurs when interconnected pores filled with N_2 at 77 K are emptied through smaller pores or narrower sections along the pore. In those pores with a diameter below 50 Å the N_2 evaporation is delayed until a critical pressure $(p/p_0)_{TSE}$ is reached, at which the hemispherical meniscus collapses and the pores are emptied at once. This also leads to the observed forced closure of the hysteresis loop as pores with smaller diameter do not

show a hysteresis [79]. As a result there is a typical sharp peak at 50 Å in the pore size distribution (see Fig. 3.12), which can be considered an artefact [97]. Therefore, as recommended [98, 99] the unaffected adsorption branch of the isotherm was used to calculate the pore size distribution.

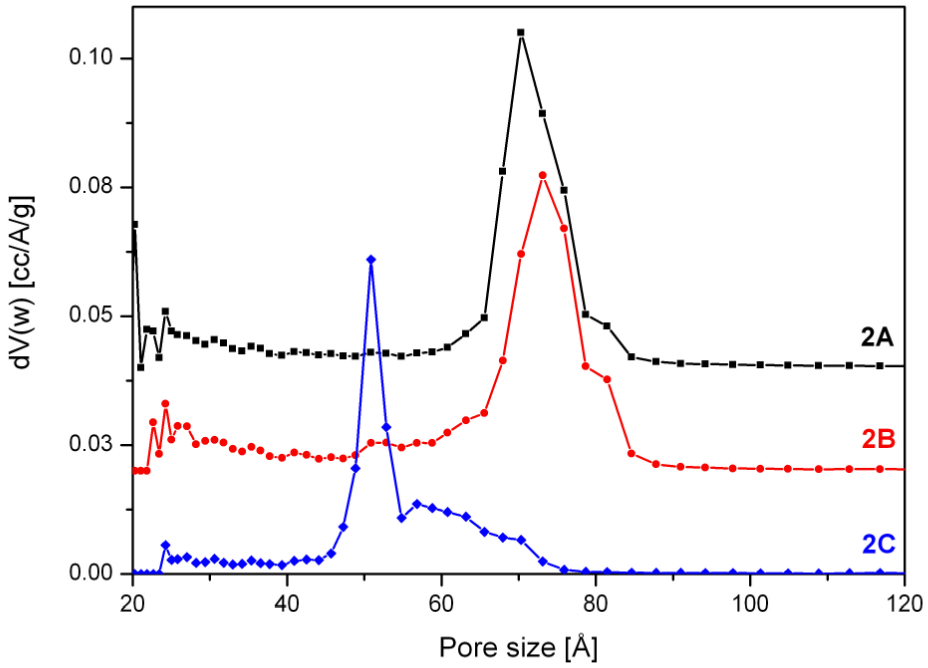

Fig. 3.12: NLDFT pore size distribution of SBA-15 unwashed (**2A**), after washing with 5 ml (**2B**) and 30 ml (**2C**) quantities of solvent calculated from the desorption branch of the isotherm. The pore size distributions are offset by 0.5 (**2A**) and 0.25 (**2B**) cc/A/g.

Nevertheless the pore size distribution of sample **2C** calculated from the adsorption branch of the isotherm is relatively broad and shifted to 61 Å as compared to sample **2A** and **2B**. This behaviour shows that the order of the pores in sample **2C** has decreased due to washing with increased solvent quantities. The ratio of the microporous to mesoporous surface area for **2C** stays almost constant compared to **2A**, whereas the contents of micropore surface area is increased by 7% for **2B** (see Table 3.2.).

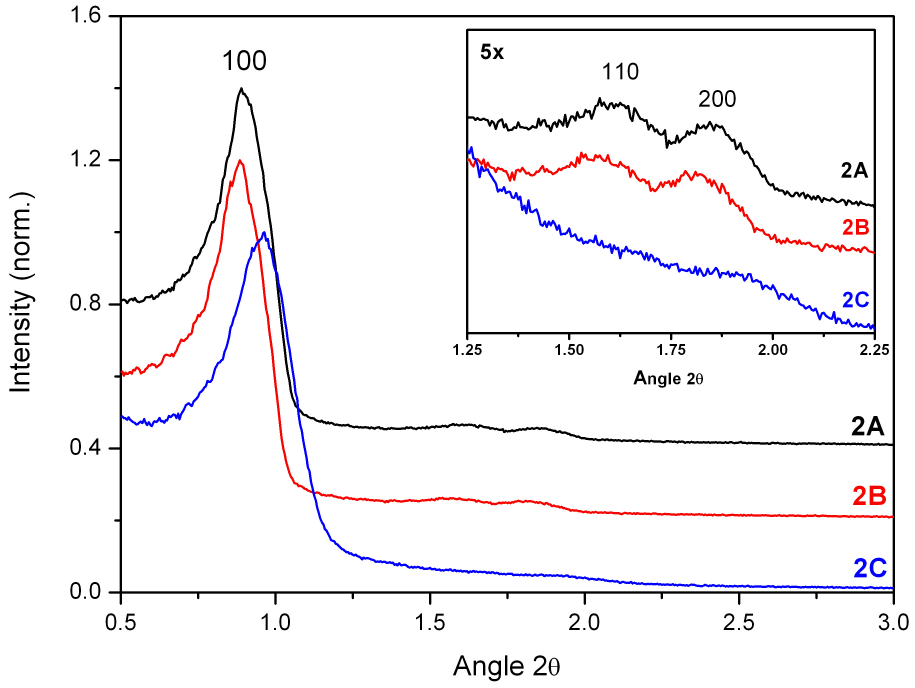

Fig. 3.13: Small angle XRD of SBA-15 unwashed (**2A**), after washing with 30 ml ethanol (**2B**) and 30 ml water (**2C**). The intensities are normalized to the 100 reflex and offset by 0.4 (**2A**) and 0.2 (**2B**).

The reduced order of homogeneity of the pores can be also observed in the XRD data (see Fig. 3.13), as the 110 and 200 reflexes almost disappear for the extensively washed SBA-15 sample **2C**. Also the lattice constant a_0 (see Table 3.2) of sample **2C** is reduced by 9 Å compared to sample **2B**, showing that plenty of washing leads to a shrinking of the SBA-15 structure.

3.3.5. Influence of Scale up on the Washing Effect

In section 3.3.4. it was pointed out that the amount of solvent used while washing has a significant influence on the shape of the isotherm and thus also on the pore size

distribution of the resulting SBA-15 material. To investigate to which extent a synthesis scale up is influenced by this "washing effect" a 9x batch was split into sub factions resembling 9x, 3x, 1x half-batches. Before washing a reference sample (80 mg) was taken form the 9x batch and calcined at 550°C. The half-batches were then washed with linearly scaled up amounts of solvent based on material weight and also calcined at 550°C.

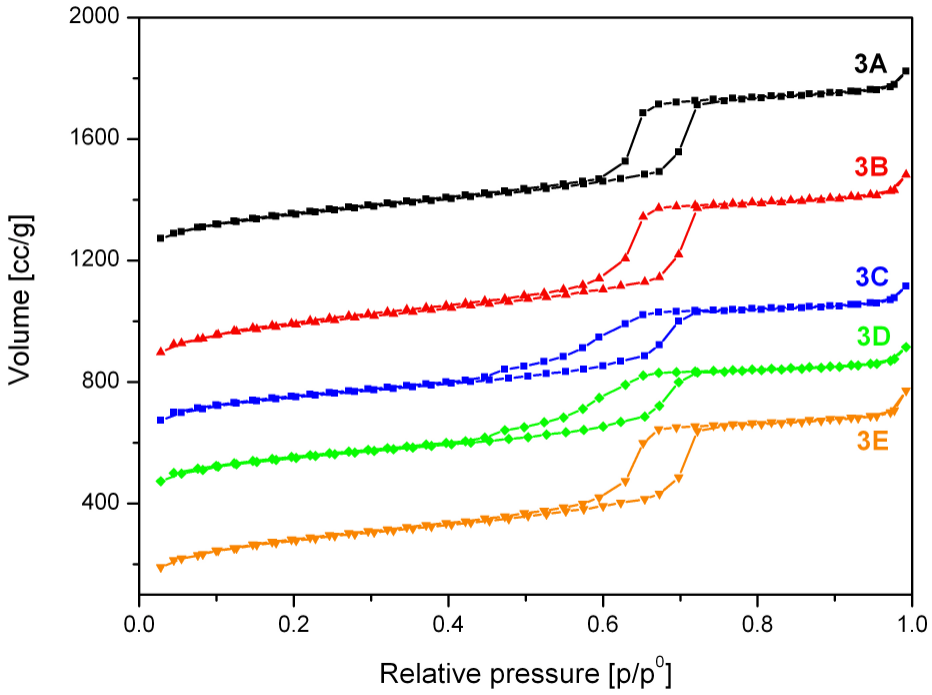

Fig. 3.14: N_2 adsorption/desorption isotherms of SBA-15 sample **3** divided into a 1x half-batch unwashed (**3A**), after washing with 5 ml (**3B**) and 30 ml (**3C**), a 3x half-batch washed with 120 ml (**3D**) and a 9x half-batch washed with 350 ml (**3E**) quantities of solvent. The isotherms are offset by 1100 (**3A**), 700 (**3B**), 500 (**3C**), 300 (**3D**) cc/g.

Interestingly, the BET isotherms of the 1x half batch (see Fig. 3.14), which has been obtained by dividing the 9x batch into smaller factions shows similar features like the 1x half batch discussed in section 3.3.4.. The surface area is maximized for the little washed sample **3B** (see Table 3.2) and the typical bulge in the desorption branch due to the tensile strength effect is observed at 0.45 p/p_0 for **3C** (see Fig. 3.14). As the extent

of the bulge is lower compared to sample **2C** the order of the mesopores appears to be slightly higher for the scaled-up sample after washing with plenty of solvent. This is also reflected in the pore size distributions shown in Fig. 4.15 as the maximum for **3C** is shifted only by 2 Å as compared to the 7 Å shift in case of **2C**. Furthermore the peak broadening of **3C** is much lower as in case of **2C**.

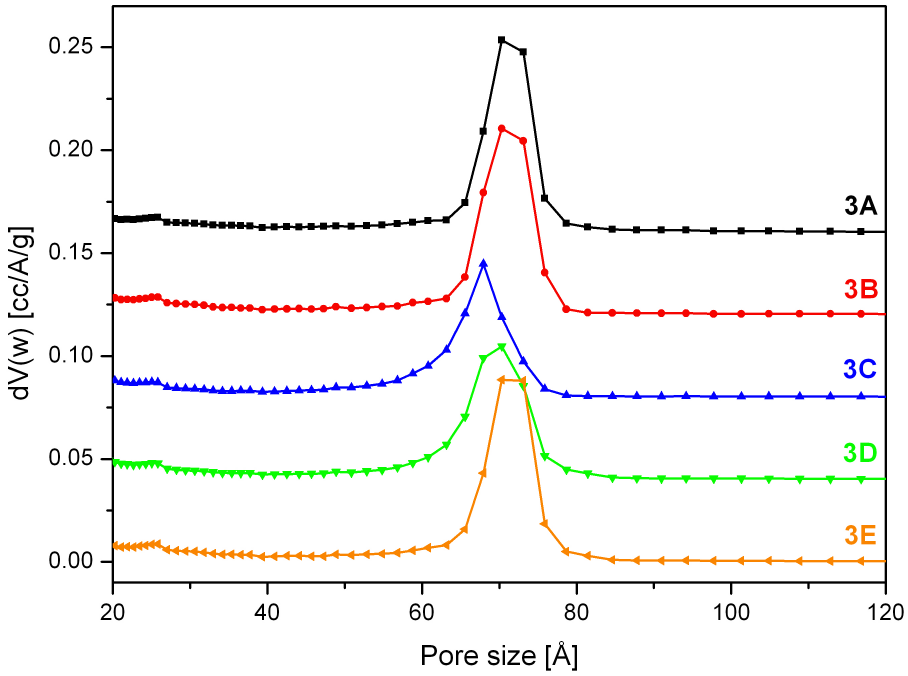

Fig. 3.15: NLDFT pore size distribution of SBA-15 sample **3** calculated from the adsorption branch of the isotherm. The sample was divided into a 1x half-batch unwashed (**3A**), after washing with 5 ml (**3B**) and 30 ml (**3C**), a 3x half-batch washed with 120 ml (**3D**) and a 9x half-batch washed with 350 ml (**3E**) quantities of solvent The pore size distributions are offset by 0.16 (**3A**), 0.12 (**3B**), 0.08 (**3C**) and 0.04 (**3D**) cc/A/g.

Comparison of the desorption branches of the isotherms of the extensively washed samples **3C**, **3D**, **3E** (see Fig. 3.14) reveals that with increasing batch size the bulge at

relative pressure 0.45 decreases and the surface area increases. This indicates that the mesopores in the material become more ordered and homogeneous during the scale up.

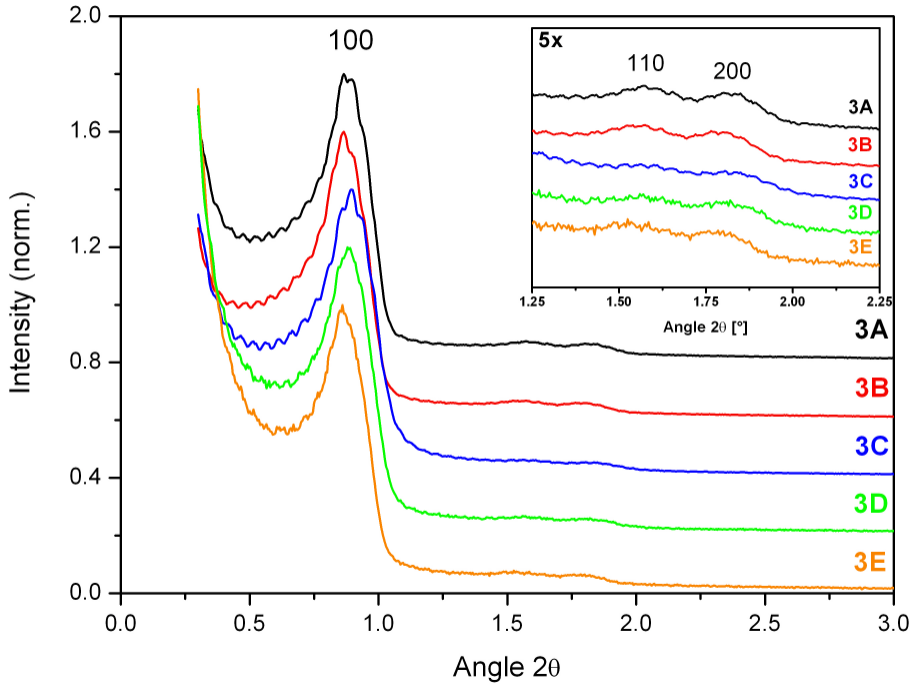

Fig. 3.16: XRD of SBA-15 sample **3** divided into a 1x half-batch unwashed (**3A**), after washing with 5 ml (**3B**) and 30 ml (**3C**), a 3x half-batch washed with 120 ml (**3D**) and a 9x half-batch washed with 350 ml (**3E**) quantities of solvent. The intensities are normalized to the 100 reflex and offset by 0.8 (**3A**), 0.6 (**3B**), 0.4 (**3C**) and 0.2 (**3D**). Note: Oscillations are an artefact in the measurement.

These results are also corroborated by small angle XRD. On the one hand, as can be seen in Fig. 3.16 the relative intensity of the 110 and 200 reflexes decreases compared to the 100 reflex from **3A, 3B** to **3C**, which shows that order of the mesopores decreases when the amount of solvent for the downscaled 1x half-batch is increased. On the other hand, an increase of the mesopore order with batch size is observed for the extensively washed samples **3C**, **3D**, **3E** as the relative intensity of the 110 and 200 reflexes increases.

An explanation for the higher quality of the SBA-15 may be that the washing process is getting less effective during linear scale-up. This behaviour is also consistent with the observation, that for smaller batches (samples **2A-C** and **3A-C**) washing with less solvent leads to a higher quality of the SBA-15.

As described above combined washing with ethanol and water may modify the SBA-15 mesopores. While small amounts of solvent lead to an increase in surface area without signficant effects on pore structure, extensive washing strongly reduces the surface area as well as the order of the pores. A possible explanation for this behaviour can be that the template is better soluble in ethanol than in water. Therefore, ethanol leads to a more efficient removal of the template like described by Ko and Bae [12, 26]. Afterwards the cleaned surface of the SBA-15 can get in full contact with the water, which is more polar and a better source for H^+ and OH^- and might induce hydrolysis reactions. As a result narrowing and widening of part of the SBA-15 mesopores may take place (see Scheme 3.1). Moreover, during extensive washing the formation of blocked pores may not be ruled out, which would offer a straightforward explanation for the significant reduction in surface area. The presence of narrowed and blocked mesopores causes delayed evaporation leading to a lower desorption pressure p/p_0 and changes in the shape of the desorption branch of the isotherm. The pores of the prepared SBA-15 materials exhibit an average diameter of 70 Å. If part of those pores is narrowed to approximately 50 Å or lower evaporation is delayed [79, 97]. As a result the tensile strength effect is observed at $p/p_0 = 0.45$ leading to a forced closure of the hysteresis loop. Its extent depends on the degree of modification, in particular the number of narrowed sections created while washing. The height of the bulge in the desorption branch may therefore be used to qualitatively estimate the degree of disorder created by combinational washing with plenty of solvent. However, the forced closure of the hysteresis loop is temperature and adsorptive dependent [100,101]. Therefore argon adsorption-desorption measurements for example are a good solution to distinguish

more clearly between pores with constrictions, plugs or corrugated surface and to obtain more reliable quantitative information about the pore size distribution [95].

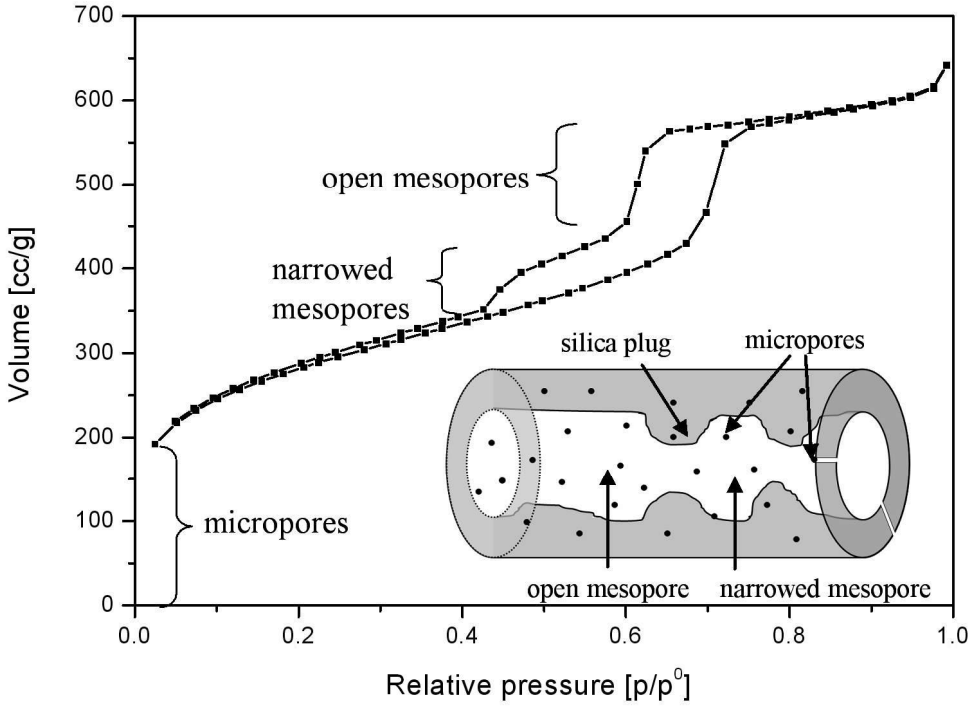

Scheme 3.1: Effect of narrowed pores in the SBA-15 structure on the isotherm shape.

The observed effect on the isotherm shape and the interpretation as blocking or narrowing of the mesopores has also been described by other researchers [96, 102-104]. Vansant et. al for instance reported for Plugged Hexagonal Templated Silica (PHTS), which is an SBA-15 analogous material synthesized at different TEOS/Pluronic 123 ratio, the occurrence of pore narrowing and blocking by silica nanoparticles inside the pores. [96,102,103] Tian et. al polymerized NIPAAM inside the SBA-15 structure and explained their XRD results and the isotherm shape with a bulge at $p/p_0 = 0.45$ by the presence of a PNIPAAM layer of varying thickness on the SBA-15 surface. [104]

3.3.6. Conclusions

Washing with plenty of pure solvent (water or ethanol) does not alter the homogeneity and order of the pores in SBA-15. A combined washing approach using water and ethanol increases the surface area, but may change the SBA-15 when plenty of solvent is used. The change can be observed as a bulge at a p/p_0 value of 0.45 in the desorption branch of the nitrogen adsorption isotherm (tensile strength effect) and a decrease of the long range order in XRD. This may be attributed to hydrolysis and recondensation reactions of the silica in the pore wall, which leads to a narrowing or widening of certain pore sections. Thus controlled washing with reduced solvent quantities is the optimum condition to obtain an increased surface area and a narrow monomodal pore size distribution. Scale up of the SBA-15 synthesis reduces the influence of the solvent volume on the shape of the isotherm and the pore size distribution.

4. Characterization of Mo_xO_y/SBA-15

4.1. Introduction

This chapter describes the synthesis of Mo_xO_y/SBA-15 and the characterization of the individual synthesis steps of the ion-exchange procedure by Raman spectroscopy (section 4.3.) and TG-MS (section 4.4.). Furthermore, the characterization of a minority phase of a β-MoO_3, which forms beside α-MoO_3 at Mo loadings larger than 13.9 wt.% Mo (3.5 Mo/nm^2) is described (section 4.5.). Finally, for samples exhibiting a crystalline and dispersed molybdenum oxide the ratio of these phases is determined by a combination of XRF and EDX results (section 4.6.).

4.2. Synthesis of Mo_xO_y/SBA-15

For the synthesis of Mo_xO_y/SBA-15 2.5 g SBA-15 were suspended in 100 ml toluene and heated to 65°C under stirring. To this suspension 6.4 ml 3-aminopropyl-trimethoxysilane (97%, Aldrich) was added and stirred at constant temperature for 12 hours. Afterwards, the solvent was removed and the functionalized SBA-15 was washed with toluene. The white powder was dried overnight and again suspended and stirred in 150 ml 0.3 M HCl for 12 hours. After removal of the solvent and washing with water the SBA-15 was dried at 130°C. [105]

Then 2 g of this functionalized SBA-15 were suspended in 60 ml distilled water. For a Mo_xO_y/SBA-15 sample with 5.9 wt.% Mo loading 183 mg ammonium heptamolybdate (99+%, Roth) was dissolved in the suspension and stirred for 12 h. The content was filtered, washed with water and dried at room temperature overnight. Finally, the

slightly greyish powder was heated up to 550°C in 6 h and calcined at this temperature for 12 h in static air.

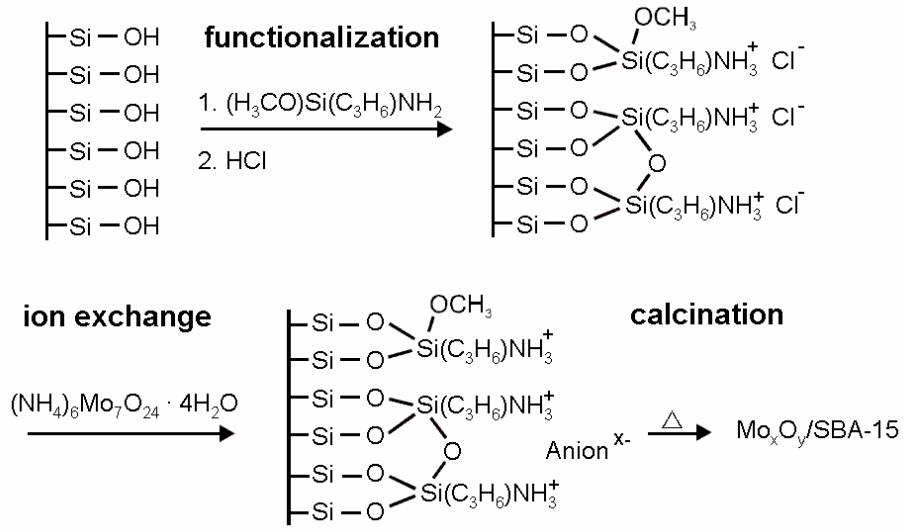

Scheme 4.1.: Scheme of the functionalization and ion exchange of SBA-15

A SBA-15 reference sample, referred to as oxa/SBA-15, was synthesized according to the above procedure with the exception that potassium oxalate monohydrate instead of ammonium heptamolybdate was used in the ion-exchange step.

For samples prepared by *incipient wetness impregnation* 186 mg molybdylacetyl-acetonate ($MoO_2(acac)_2$) were dissolved in 18 ml ethanol, mixed with 4.0 g bare SBA-15 to obtain a Mo loading of 5.5 wt.% Mo. Then the sample was dried overnight at room temperature and calcined for 12 h at 550°C.

4.3. Characterization of the Mo_xO_y/SBA-15 Synthesis by Raman Spectroscopy

Spectrum (a) in Figure 4.1 shows the Raman spectrum of APTMS (aminopropyltri-methoxysilane) functionalized SBA-15 after protonation of the amino group. The bands

at 855, 939 and 1042 cm^{-1} can be attributed to C-C stretching vibrations of the propylammonium group. [106] The bands at 490 and 988 cm^{-1} are identified as the silica D1 band of cyclic tetrasiloxane rings [107] and the Si-OH stretching mode of surface hydroxyl groups, respectively. [108] Spectrum (c) corresponds to a ammonium heptamolybdate (AHM) solution at pH 5.6. Interestingly, the spectrum of the AHM solution shows features which should only be present in solid AHM. [43,109] According to Beato et al., the band at 940 cm^{-1} can be assigned to the Mo=O stretching mode, whereas the band at 892 cm^{-1} represents a Mo=O stretching and bending combination mode. The band at 631 cm^{-1} is identified as a Mo-O-Mo bending mode and the bands at 550 and 364 cm^{-1} as O-Mo-O bending modes. [110]

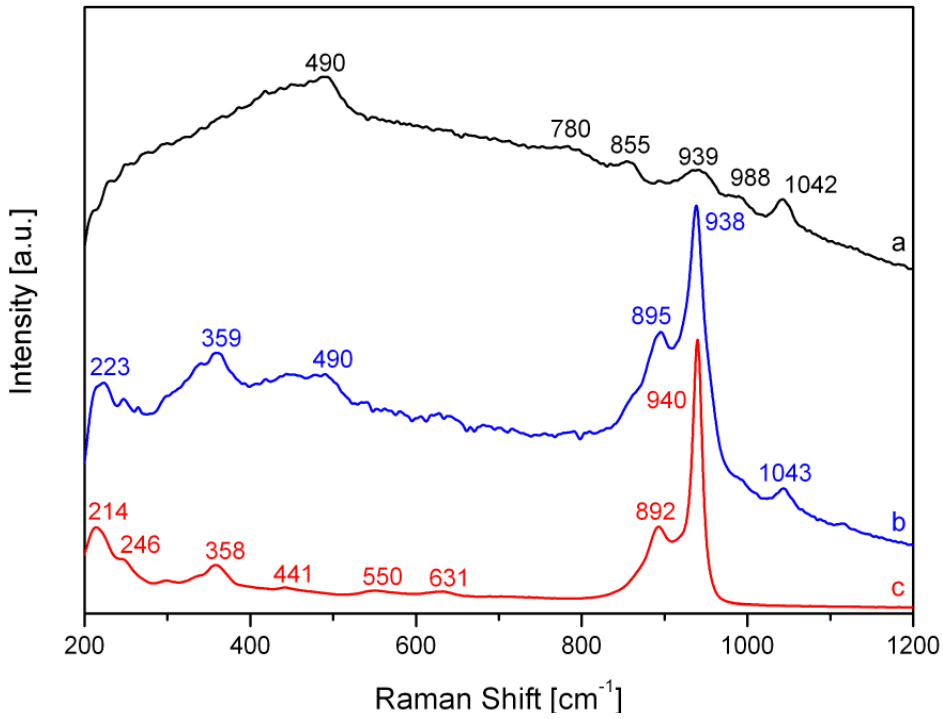

Fig. 4.1: Raman spectra at 633 nm excitation of (a) APTMS functionalised SBA-15; (b) APTMS functionalized SBA-15 after ion exchange with AHM;(c) AHM solution. The spectra are offset for clarity.

Furthermore, the band at 441 cm^{-1} can be assigned to torsion vibrations and the bands at 358, 246 and 214 cm^{-1} to bendings, "bridge stretchings" and torsion modes,

respectively. [110] After the ion exchange the AHM and functionalized SBA-15 containing suspension had a pH of 4.0. A comparison with the phase diagram of isopolymolybdates shows that the majority of isopolymolybdates is present as heptamolybdate anions ($Mo_7O_{24}^{6-}$) in solution. [111] As can be seen in spectrum (b), which was taken of the wet filter cake after ion exchange, the heptamolybdate anion is still intact after the ion exchange step.

Calcination of the dried and grinded filter cake resulted in an anchored, dispersed molybdenum oxide on the SBA-15 surface. Raman spectroscopy gave no indication for the presence of crystalline MoO_3 (Fig. 6.1 and 6.2) up to a loading of 12.1 wt.% Mo (3.5 Mo/nm^2). The structure of the dispersed molybdenum oxide will be discussed in detail in chapter 6.

4.4. TG-MS and DSC

Figures 4.2 and 4.3 show the decomposition of APTMS/SBA-15, after ion exchange with AHM and potassium oxalate in aqueous solution and subsequent drying like described in section 4.2. The samples have been heated in an oxygen/argon atmosphere (20:80) at a heating rate of 2 K/min from room temperature to 700°C. During decomposition the mass loss has been measured by Themogravimetry (TG) and the heat flow by Differential Scanning Calorimetry (DSC). Furthermore, the evolved gases during the process have been monitored by MS. The mass traces at m/z 18, 28, 30 and 44 may be associated with H_2O, CO or N_2, NO and CO_2 or N_2O, respectively.

The decomposition of APTMS/SBA-15 and the heptamolybdate anion shown in Fig. 4.2 starts with the loss of adsorbed residual water in the structure, as indicated by a peak at 65°C in the trace of mass 18. Then, at approximately 200°C, an exothermal peak in the DSC curve and two peaks at mass 18 and 30 are observed. As no increase of the traces for mass 28 and 44 representing CO, N_2, CO_2 and N_2O, is observed, this may be attributed to the decomposition of ammonium groups of the APTMS functionalized

SBA-15 or residue ammonium ions forming primarily H_2O and NO at that temperature. It seems more likely that these peaks are due to residue ammonium counterions surrounding the heptamolybdate as they are missing in the sample prepared by ion

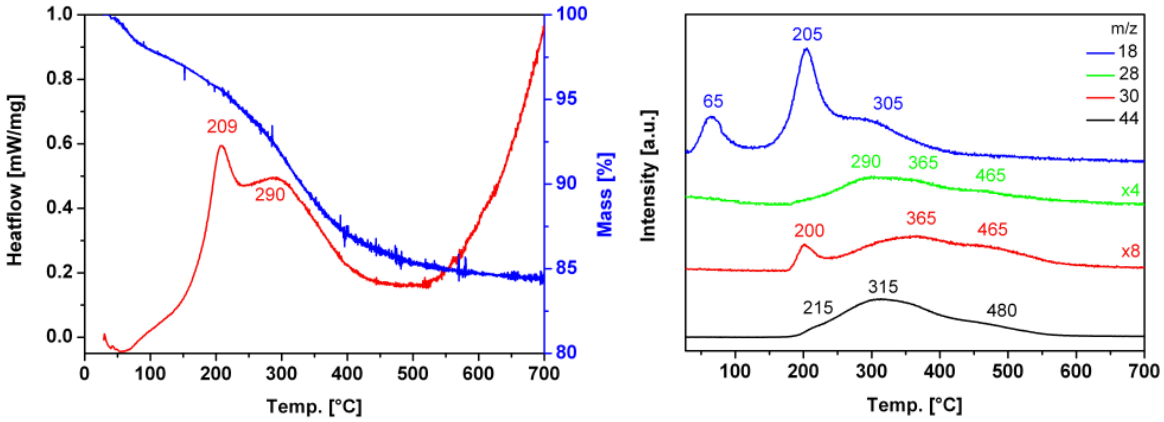

Fig. 4.2: Decomposition of APTMS/SBA-15 after ionexchange with AHM to 12.1 wt.% Mo Mo_xO_y/SBA-15; TG and DSC (left); MS (right)

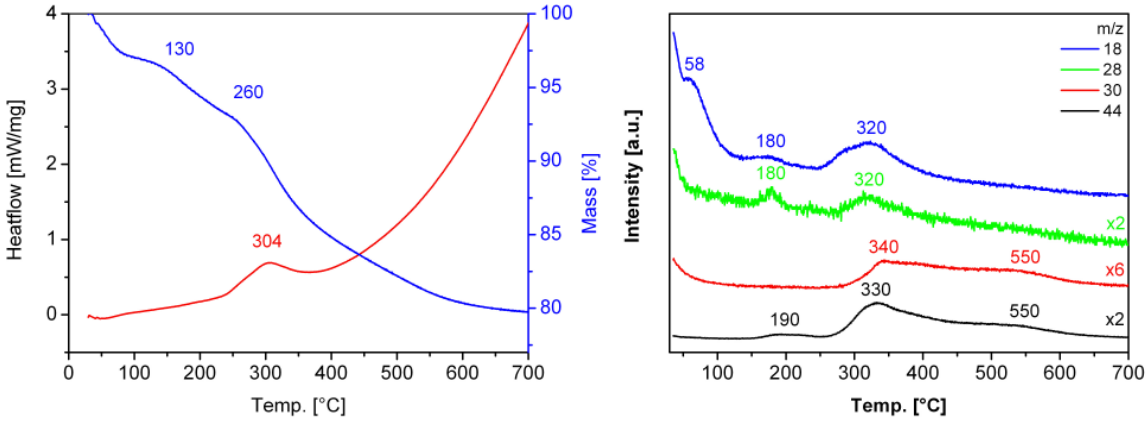

Fig. 4.3: Decomposition of APTMS/SBA-15 after ion exchange with $K_2C_2O_4 \cdot 2\ H_2O$ to oxa/SBA-15; TG and DSC (left); MS (right) and SBA-15-APTMS; (A) TG and DSC; (B) MS

exchange with potassium oxalate (Fig. 4.3). The nitrogen content is calculated to be 4.7 wt.% from the APTMS functionalization and at maximum 1.4 wt.% from the AHM, if six ammonium counterions are considered. As some free ammonium ions should be

substituted by the ammonium ions from the APTMS functionalized matrix during ion exchange, this value should be even lower. If it is assumed that the decomposition of the free ammonium ions occurs at lower and the one of the ammonium ions from the APTMS functionalization at higher temperatures, the ratio for mass 30 of the peak at 200°C and the broad peak with a maximum at 365°C can be explained.

At higher temperatures, the rest of the organic APTMS framework starts to be oxidized, which is indicated by a constant increase of the mass traces 18, 28, 30 and 44 until 300°C. This is also supported by the observation of a second exothermic peak around 290°C in the DSC curve and an accelerated weight loss around that temperature. At higher temperatures the mass traces decrease and reach the level before decomposition at approximately 550°C, which indicates that the organic framework has been oxidized and removed from the silica matrix.

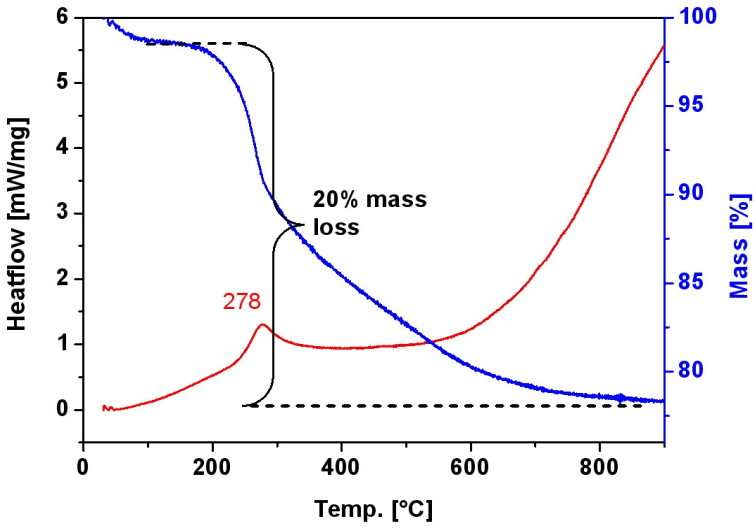

Fig. 4.4: TG and DSC during decomposition of APTMS/SBA-15.

The decomposition behaviour of AHM is influenced by the organic APTMS framework. Therefore, a comparison with pure AHM [112] is relatively difficult as the elements forming volatile products in AHM contribute only 1.5 wt.% to the uncalcined sample,

whereas the organic APTMS framework has a contribution of 15 wt.%. Additionally, as already mentioned, the APTMS framework contains also ammonium groups, which makes it difficult to distinguish between oxidation products from ammonium groups in the framework and free ammonium ions. Nevertheless, the decomposition process seems to have some differences from bulk AHM [112].

For example, in contrast to bulk AHM during decomposition of APTMS/SBA-15 after ionexchange with AHM (AHM/APTMS/SBA-15) the evolution of ammonia (m/z = 15) has almost not been observed. Furthermore, the maximum of ammonia evolution for bulk AHM is at 260°C, while the maximum of the ammonia and NO evolution for the AHM/APTMS/SBA-15 decomposition is at 200°C. The little exothermic transition at 190°C in the DTA curve of bulk AHM may possibly be associated with the exothermic transition at 209°C in the DSC curve of decomposition of AHM and APTMS/SBA-15. But the two endothermic transitions at 130 and 260°C, which are relatively intense in the DTA curves of bulk AHM are not resolved in the DSC curve.

The decomposition of a reference sample containing potassium oxalate and APTMS/SBA-15 is shown in Fig. 4.3. As discussed previously first adsorbed water is removed at 65°C. The feature at 180°C can be associated with oxalate decomposition. [113,114] The decomposition process of the organic APTMS framework starts at approximately 260°C and finishes at 650°C, which is slightly higher than for the sample containing AHM. The total mass loss is about 20% and the exothermic feature in the DSC curve at 304 °C is slightly shifted to higher temperatures, compared to the AHM containing sample. These results seem to indicate that molybdenum oxides formed from the AHM have a catalytic behaviour in the decomposition of the organic framework.

The mass loss for pure APTMS/SBA-15 is about 20% (see Fig. 4.4). The weight loss during the decomposition of the organic APTMS framework and has been used to correct the theoretical expected loading of molybdenum oxide on SBA-15 after calcination.

4.5. Characterization of the Minority Phase

The minority phase found by Raman spectroscopy, which is described in chapter 6.2., has also been analysed by XRD and Electron diffraction. Figure 4.5 depicts the XRD of a Mo_xO_y/SBA-15 sample with a loading of 13.9 wt.% Mo (6.8 Mo/nm^2), which contains X-ray amorphous molybdenum oxide and crystalline MoO_3. A fit of the diffractogram with the ICSD database [ICSD: 35076] shows that the majority of the crystalline phase is composed of α-MoO_3. [115] For the minority phase monoclinic β-MoO_3 [ICSD: 202324], β'-MoO_3 [ICSD: 86426] and MoO_3 II [ICSD: 80577], a

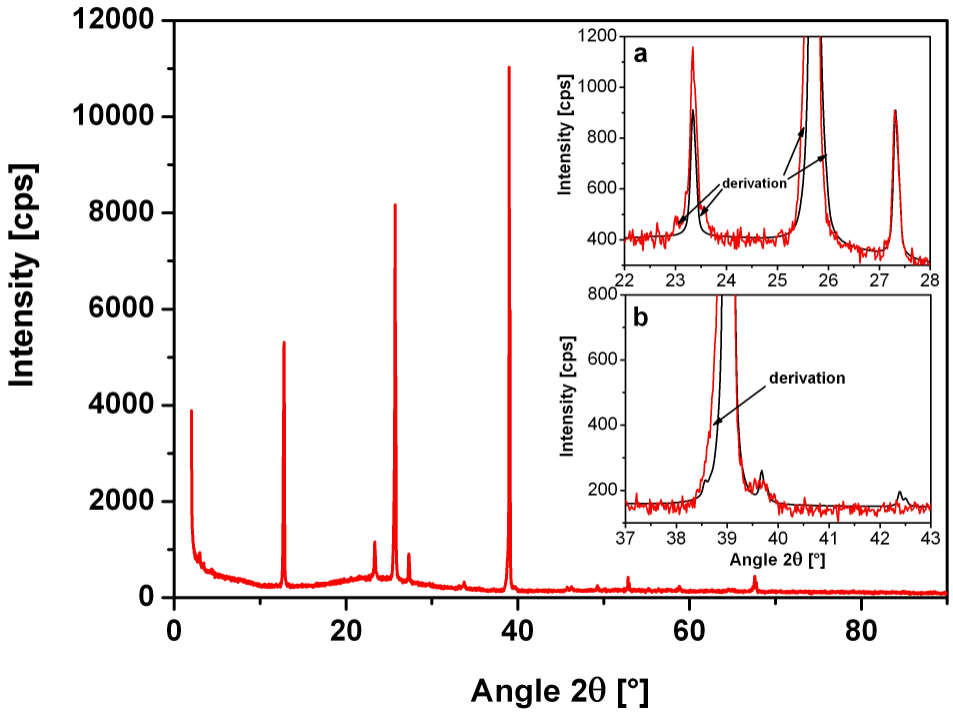

Fig 4.5: XRD of Mo_xO_y/SBA-15 with 13.9 wt.% Mo (6.8 Mo/nm^2); Insets a and b: Details of XRD of Mo_xO_y/SBA-15 with 13.9 wt.% Mo (6.8 Mo/nm^2) (red), α-MoO_3 Fit (black)

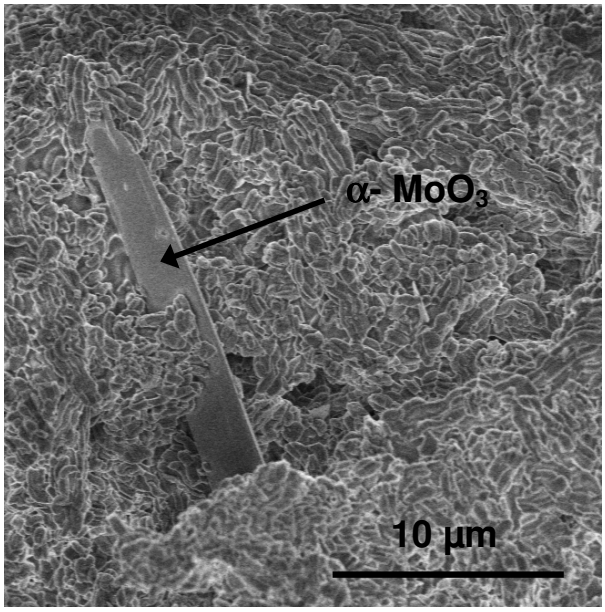

Fig. 4.6: SEM picture of Mo_xO_y/SBA-15 with 14.0 wt.% Mo (6.8 Mo/nm^2) showing of α-MoO_3 crystallites beside SBA-15 particles with dispersed molybdenum oxide.

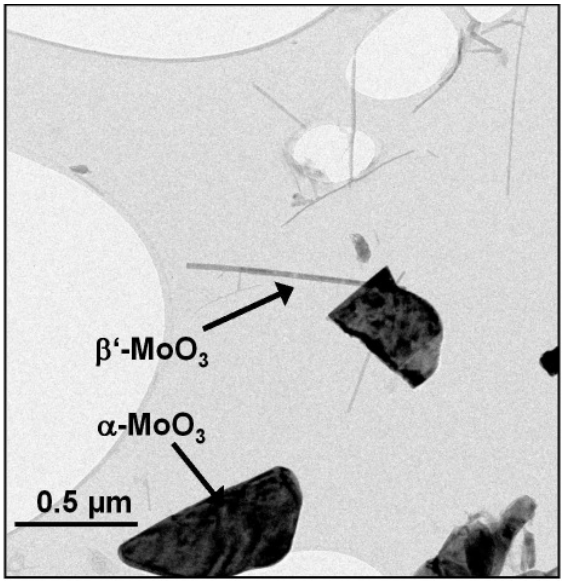

Fig. 4.7: HRTEM micrograph of plate like α- and needle like β'-MoO_3 crystallites on Mo_xO_y/SBA-15 with 14.0 wt.% Mo (6.8 Mo/nm^2).

monoclinic α-MoO_3 related structure, have been considered for a fit of the residue intensity, not covered by the α-MoO_3-Fit. [116-118]. The best description is obtained by

a monoclinic β'-MoO_3 phase, while the β-MoO_3 should be excluded according to XRD results.

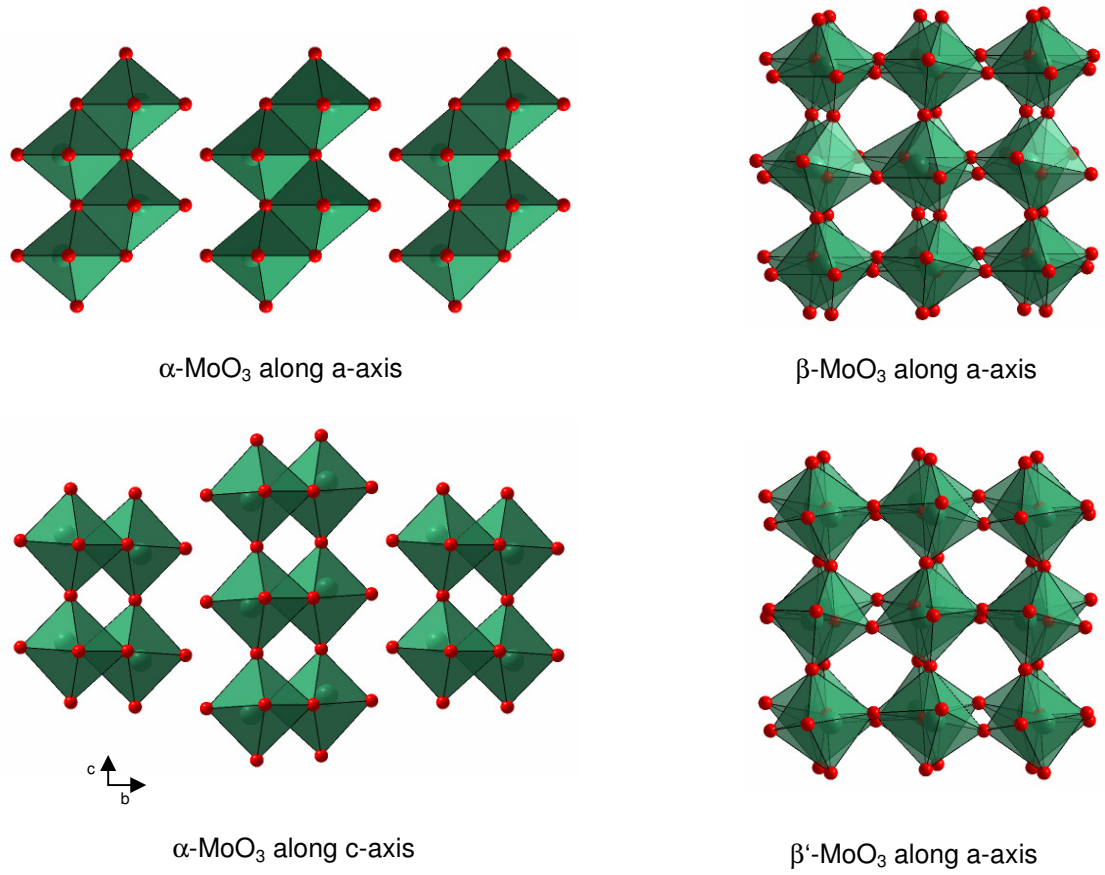

Fig 4.8: Structures of α, β and β'-MoO_3

The MoO_3-crystallites causing the reflexes in XRD have also been found by electron microscopy. On the one hand, big needle like α-MoO_3 crystallites (see Fig. 4.6) with an extension of approx. 20 µm and 2 µm diameter have been found among the SBA-15 particles supporting the dispersed Mo_xO_y phase. On the other hand, two kinds of different, smaller MoO_3-crystallites with a plate and a needle like structure (see Fig. 4.7) have been detected by high resolution transmission electron microscopy (HRTEM). The crystallites with a plate like structure have a diameter of approx. 0.5 to 1 µm and have

been identified as orthorhombic α-MoO_3 by electron diffraction. The needle like crystallites have a length of 0.3 to 1 µm and can be assigned by electron diffraction to β-MoO_3.

For further interpretation of the result it should be taken into account that the β- or β'-MoO_3 minority phase represents only 1 to 3 % of the crystalline phase. Besides that the amount of crystalline MoO_3 present on the sample is about 2 wt.% Mo (see chapter 4.5.). Therefore, only 0.06 wt.% Mo of the minority phase are present at maximum. In addition to that, as can be seen in Fig. 4.8, the structures of β- and β'-MoO_3 are very similar. Both structures represent a distorted ReO_3 structure, where the molybdenum oxide octahedrals in the β-MoO_3 structure exhibit smaller disorder than the β'-MoO_3 structure.

As the electron beam in HRTEM can easily induce transitions between β- and β'-MoO_3 the results of Raman spectroscopy and XRD are maybe more reliable than electron diffraction. Therefore it can be concluded that the minority phase is with higher probability β'-MoO_3.

4.6. Distribution of Crystalline and Disperse Molybdenum Oxide

The Mo loading of the Mo_xO_y/SBA-15 samples has been determined by X-ray fluorescence (XRF) and energy dispersive X-ray spectroscopy (EDX). Fig. 4.10 shows the loading measured by XRF and EDX versus the theoretical loading that is expected. EDX was used to probe only sections of the sample with 0.5 μm^2 size, which have been free of crystalline MoO_3. (see Fig. 4.9) As EDX is a local method, 25 measurement points have been chosen per sample to determine the average Mo loading of dispersed molybdenum oxide and to minimize the statistical error.

As can be seen in Fig. 4.10, up to 14.0 wt.% Mo the Mo loadings determined by XRF are in very good agreement with the expected theoretical loading. This is also indicated by a linear regression of the data points in this loading range, which shows a regression coefficient and a slope of the trend line of almost 1 (see Fig. 4.10). The maximum deviation from the theoretical loading in this range is about 0.1 wt.% Mo. Thus it can be concluded, that the ion-exchange procedure leads to a quantitative insertion of the molybdenum oxide into the SBA-15 structure.

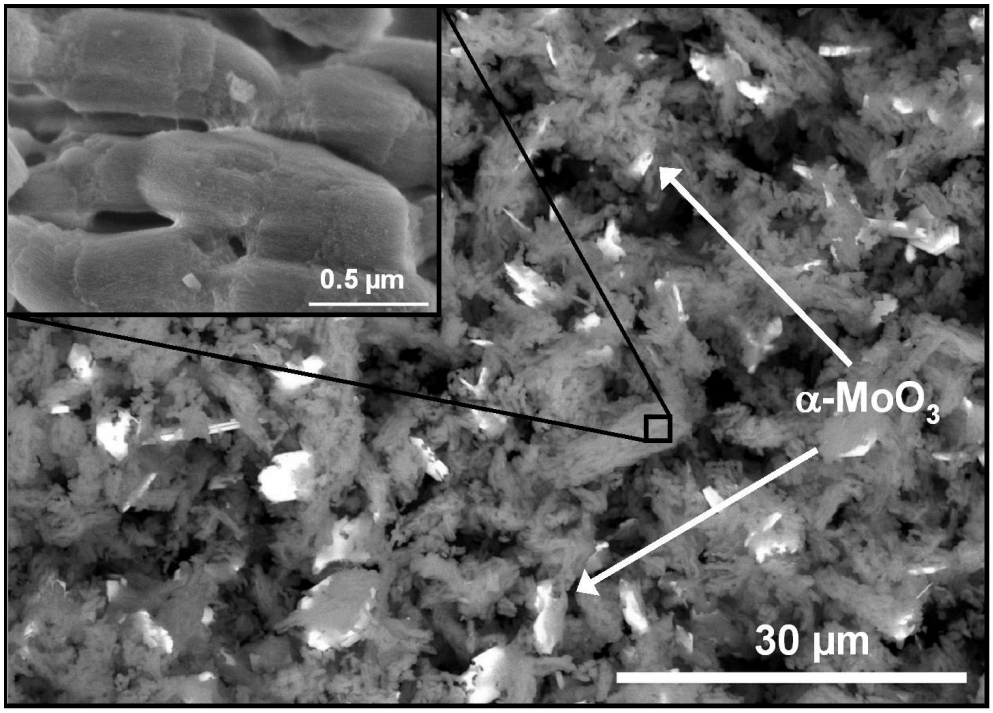

Fig. 4.9: SEM picture of a Mo_xO_y/SBA-15 sample with a Mo loading of 21.1 wt.% Mo (9.8 Mo/nm²). The inset indicates the size of a EDX sampling spot, which is well separated from surrounding MoO_3 crystallites.

The loading determined by EDX shows a higher deviation from the theoretical loading than XRF and overestimates the Mo-loading by 0.2 to 0.3 wt.% Mo up to a loading of 12.0 wt.% Mo (3.2 Mo/nm²). Above this loading, the XRF and EDX loading curves separate. This is in agreement with the observation of Raman spectroscopy (chapter 6.2)

and XRD that above 12.1 wt.% Mo crystalline MoO_3 is formed beside dispersed molybdenum oxide. On the one side, the EDX curve stays almost constant at 12 to 13 wt.% Mo. This indicates that the amount of molybdenum oxide, which can be present in a dispersed state on the SBA-15 has an upper limit and is not increasing further when crystalline MoO_3 starts to be formed with increasing total Mo-loading. On the other side, the total Mo loading represented by the XRF loading curve also starts to deviate from the theoretical loading and reaches a maximum at 21.1 wt.% Mo. Beyond this loading a decrease of the total loading has been observed. This behaviour can be explained by saturation, as the SBA-15 structure has a finite capacity for the uptake of the molybdenum precursor in the ion-exchange procedure.

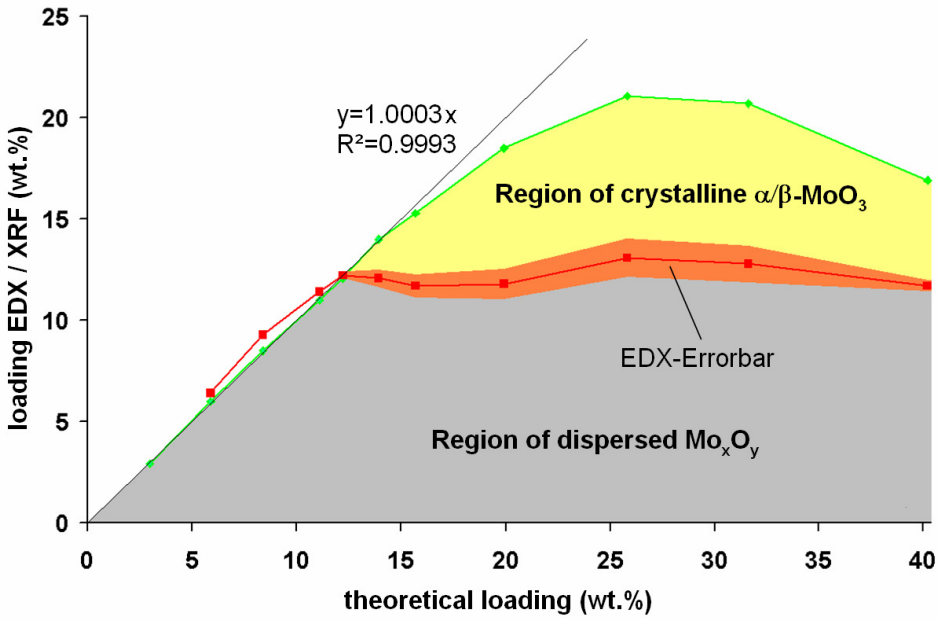

Fig. 4.10: Loading-dependent distribution of dispersed and crystalline molybdenum oxide. The total Mo-loading has been measured by XRF (green). The Mo loading of the dispersed Mo_xO_y-species has been measured by EDX (red).

A determination of the crystalline to dispersed molybdenum oxide ratio with other spectroscopic techniques is rather difficult. Raman spectroscopy for example has the disadvantage that the cross sections of the signal depend on the crystallinity and

hydratization of the sample, which may be an individual property of each sample, so that there is no fixed relation between molybdenum amount and signal intensity. Additionally, in the dehydrated state, there is a significant overlap of the molybdyl bands of the dispersed (960 to 991 cm^{-1}) and the crystalline phase (995 cm^{-1}) which are used for the quantification. Furthermore, Raman as a method is to local, because the spot diameter of the laser beam depending on the used objective is about 1 to 30 µm and the size of the hugest crystals 20 µm. Hence, the homogeneity of the sample is not good enough to get a statistically sufficient low error. IR spectroscopy is not possible, as the sample is strongly absorbing below 1300 cm^{-1} due to the silica support. TPO and TPR is not possible as well, as the structure of SBA-15 supported molybdenum oxide starts to be altered at temperatures above 550°C. UV/Vis spectroscopy or XAS for the distinction of the two phases might work, but has a low precision for the determination of the phase ratio. If XPS is employed synchrotron radiation should be used to get a better resolution of the Mo 3d peaks maybe than ratio of dispersed and crystalline molybdenum oxide can be determined with sufficient precision. Therefore the combination of EDX and XRF seems to be the most precise solution to distinguish the two contributions.

4.7. Conclusions

Raman spectroscopy demonstrates that during the ion exchange step the heptamolybdate precursor is introduced intact into the APTMS-functionalized SBA-15 structure. The TG-MS results show that the decomposition of the organic framework during calcination of Mo_xO_y/SBA-15 is completed at 550°C. Moreover, the weight of the silica for the determination of the molybdenum loading should be corrected by 20%, because of the removal of the organic framework during the calcinations processes. Furthermore by XRD and electron diffraction in HRTEM the presence of a minority β-

MoO_3 phase besides a α-MoO_3 and dispersed molybdenum oxide at Mo-loadings higher than 13.9 wt.% Mo (3.5 Mo/nm^2) has been detected. The fractions of the crystalline and dispersed molybdenum oxide phase in dependence of the total loading were determined by a combination of XRF and EDX. The results show that the fraction of dispersed molybdenum oxide is almost constant at 12 to 13 wt.% Mo. The maximum total loading of molybdenum oxide was determined to be 21.1 wt.% Mo with a crystalline MoO_3 content of approximately 8 wt.% Mo.

5. Catalysis of Mo_xO_y/SBA-15

5.1. Propylene Oxidation

The Mo_xO_y/SBA-15 (5.9 wt.% Mo, 0.8 Mo/nm^2) has been tested for its catalytic properties in propane and propylene oxidation at atmospheric pressure and temperatures between 400 and 500°C. The reaction products were analyzed by GC-MS. As the catalyst shows only little activity in selective propane oxidation to propylene or other oxygenates the examination has been focused on propylene oxidation. According to the literature the activation energy for propane oxidation should be higher for molybdenum oxide (117 kJ/mol) than for vanadia (99 kJ/mol), which implies that higher temperatures for propane oxidation by molybdenum oxide are needed. As the activation energy for consecutive oxidation of the formed propylene is much lower as the temperatures

Tab. 5.1.: Propylene oxidation on 5.9 wt.% Mo (0.8 Mo/nm^2) Mo_xO_y/SBA-15, ($C_3H_6/O_2/N_2$ = 3/7/90)

Temp. [°C]	GHSV [ml·h^{-1}·g^{-1}]	Conversion [%] C_3H_6	Selectivity [%] PA	ACR	ACE	AA	ACA	CO_2	CO
400	2000	3	53	10	8	0	1	11	18
450	1250	10	36	19	9	1	1	11	22
450	1500	8	39	19	9	1	0	11	21
450	2000	5	39	16	9	1	0	13	21
500	1000	29	21	20	9	1	0	14	34
500	2000	12	31	23	11	1	0	11	23
500	3000	7	37	25	10	1	0	9	18

* PA = propionaldehyde, ACR = acrolein, ACE = acetone, AA = acrylic acid, ACA = acetic acid

required for the oxidation primarily total oxidation is observed. [119] Solymosi and coworkers for instance reported that a silica supported catalyst with 0.4 Mo/nm^2, showed almost no propane selective conversion to oxygenates at 500°C. [120] Oyama used a silica supported catalyst with a Mo density of 1.2 Mo/nm^2 for propane oxidation at a pressure 4.5 atm and 336°C and observed the formation of oxygenates. The Mo_xO_y/SiO_2 catalysts were tested at high reactant concentrations (C_3H_8/O_2/He=10/5/10 ml/min) and high catalyst quantities (1.0 g). [8]

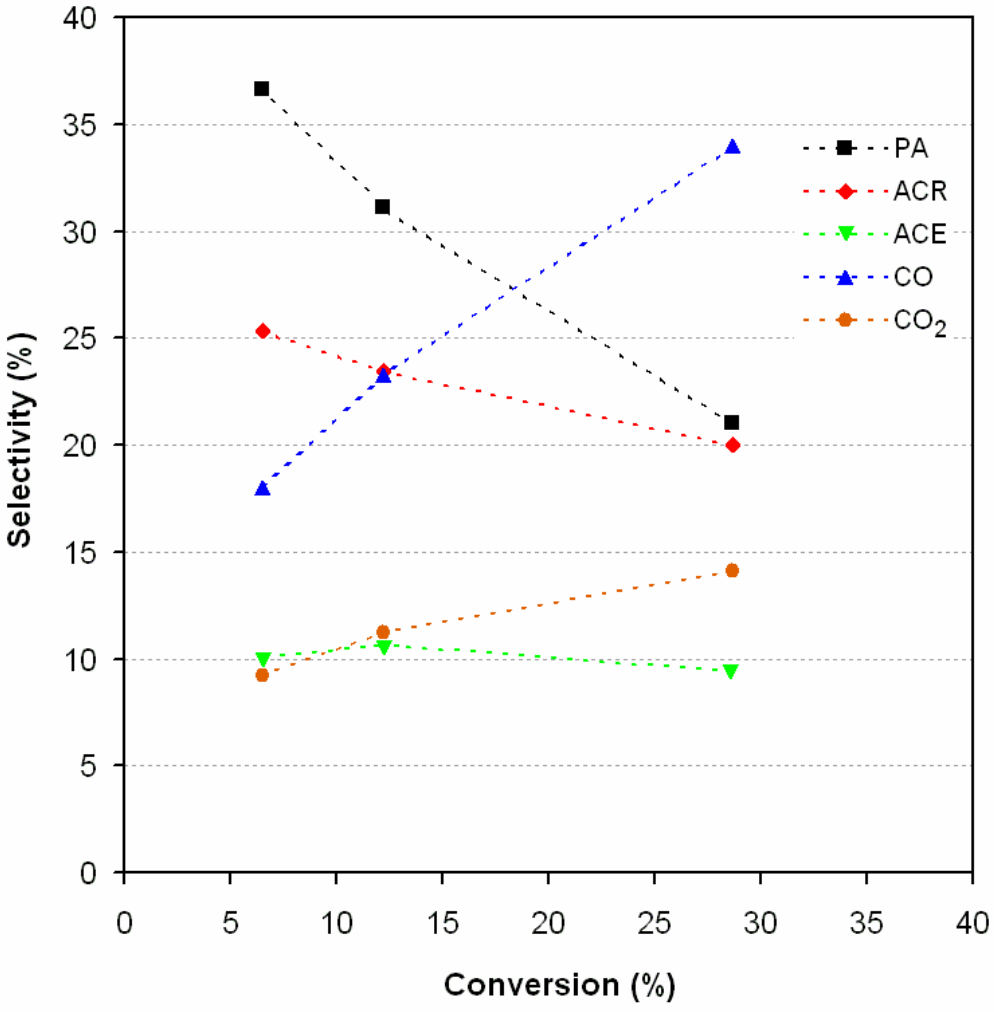

Fig. 5.1: Conversion versus selectivity plot for propylene oxidation ($C_3H_6/O_2/N_2$ = 3/7/90) over 5.9 Mo wt.% Mo (0.8 Mo/nm^2) Mo_xO_y/SBA-15 at 500°C and a GHSV of 1000, 2000 and 3000 ml·h^{-1}·g^{-1}. (PA = propionaldehyde, ACR = acrolein, ACE = acetone, AA = acrylic acid, ACA = acetic acid)

For propylene oxidation on Mo_xO_y/SBA-15 catalysts (0.8 Mo/nm^2) propionaldehyde, acetone and acrolein have been observed as main products, whereas acrylic acid and acetic acid are only minor products (Table 5.1 and Fig. 5.1). Additionally, also ethylene, formaldehyde, propylene oxide and acetaldehyde are formed, but have not been quantified, as their yield is small compared to the other products. With increasing conversion, as shown for instance for 500°C in Fig. 5.1, the total oxidation increases while the selective oxidation towards acrolein and even more for propionaldehyde decreases. In contrast the selectivity for acetone as the third of the major oxygenates stays almost constant, which supports the idea that acetone is formed in a different kind of mechanism than acrolein and propionaldehyde. [5] The selectivity for acrylic acid is relatively low as steam is absent, which is required for a deeper oxidation of propylene. [5] Furthermore, from the distribution of C_1, C_2 and C_3 products it can be derived that the oxygen species on the surface should be more nucleophilic than electrophilic, as the quantities of oxygenates which require carbon bond cleavage is lower. [58, 121-123] A comparison with catalysis data of Liu et al. for silica supported molybdenum oxide catalyst with 0.8 (1.1) Mo/nm^2 and 0.5% (3%) conversion at 400°C shows that the selectivity pattern is close to the values reported in Table 5.1. Propionaldehyde and CO_2 is produced with the same selectivity like on the Mo_xO_y/SBA-15 catalysts, whereas acrolein is produced with a higher selectivity. Furthermore acetaldehyde is reported as major product. [124] In contrast, Oyama and coworkers observed at 400°C and the same conversion level for a Mo-catalyst (0.5 Mo/nm^2) the formation of acrolein and CO_x as major product beside minor amounts of propionaldehyde and acetaldehyde. [121] Additionally, acrolein, acetaldehyde and CO_x have been reported by Vaghi to be the major products besides the minor products propionaldehyde, acetone and acetic acid. [125] The occurance of propylene oxide quantity has been observed at pressures of 4.5 atm and 300°C on Mo_xO_y/SiO_2 samples, which contained trace amounts of MoO_3. A pressure reduction led for those catalysts to a selectivity change to acrylic acid and acetone as major products. [9] The oxa/SBA-15 as silica support reference is not

catalytically active and only the formation of CO_x has been observed at higher temperatures.

5.2. Conclusion

The Mo_xO_y/SBA-15 system is active in selective propylene oxidation, whereas propane oxidation only leads to total oxidation. Propionaldehyde, acetone and acrolein have been observed as main oxidation products. Acrylic acid has been detected only as minor product. From the product distribution it can be concluded that the catalyst possesses electrophilic as well as nucleophilic oxygen species and that several kinds of active sites are present on the catalyst surface. Furthermore, the observed products are in agreement with catalytic data found in the literature.

6. Detailed Structural Characterization of Mo_xO_y/SBA-15

6.1. Introduction

In this chapter the attempt for a structural assignment of the silica SBA-15 supported dispersed molybdenum oxide in the hydrated and dehydrated state is made. Therefore, a combination of spectroscopic techniques like Raman-, IR-, UV/Vis-, Photoelectron- and X-Ray Absorption Spectroscopy are employed. One question of interest is whether, as proposed in the literature, only isolated monomeric molybdenum oxide species are present in the dehydrated state or whether di- or oligomeric species are also present. [30,31,126] Furthermore, it is examined how the catalyst changes under reaction conditions while propylene oxidation and how steam effects the catalyst structure. Additionally, also information about the dispersion of the supported molybdenum oxide is obtained by XPS.

6.2. Raman Characterization of Mo_xO_y/SBA-15

Figures 6.1 and 6.2 depict Raman spectra of hydrated and dehydrated Mo_xO_y/SBA-15 at different molybdenum loadings in comparison to bare SBA-15, respectively. The loadings and the surface characteristics of the samples are given in Table 6.1. Raman spectroscopy has been shown to be a very sensitive indicator for the presence of crystalline MoO_3 [127]. Interestingly, for the Mo_xO_y/SBA-15 samples prepared by grafting/ion-exchange the formation of crystalline MoO_3 is observed at a higher molybdenum density (3.5 Mo/nm^2) as compared to other silica supported systems

Table. 6.1: Surface and porosity characteristics of the Mo_xO_y/SBA-15 samples and bare SBA-15

sample	preparation	Mo (wt%)	Mo (Mo/nm^2)	S_{BET} (m^2/g)	d_P (Å)	V_p (cm^3/g)
SBA-15	---	0.0	0.0	770	73	1.00
SBA-15 (ox)	ion exchange	0.0	0.0	408	62	0.50
Mo_xO_y/SBA-15	ion exchange	1.0	0.2	520	63	0.62
		5.9	0.8	422	63	0.55
		8.4	1.5	345	70	0.46
		11.0	2.4	294	70	0.45
		12.1	3.5	217	69	0.35
		13.9	6.8	130	70	0.27
	incipient wetness	5.5	0.6	596	70	0.80

prepared by impregnation techniques (≤1.1 Mo/nm^2). [28,35,36] This behaviour can be attributed to a better control of the precursor dispersion on the functionalized support during synthesis. [90]

As shown in Fig. 6.1, the room temperature Raman spectra of hydrated Mo_xO_y/SBA-15 are characterized by bands at around 950, 875, 500, 422, 380 and 230 cm^{-1}. [128]

First the contribution of the bare support will be discussed. SBA-15 shows an intense band around 500 cm^{-1} which is attributed to cyclic tetrasiloxane rings (D1 defect mode). [107] The weaker bands at around 600, 800 and at 977 cm^{-1} can be assigned to cyclic trisiloxane rings (D2 defect mode), the symmetrical Si-O-Si and the Si-OH stretching mode of surface hydroxyl groups, respectively (see Fig. 6.1). [107,108,129,130]

Regarding the contribution from molybdenum oxide, the two dominant bands at 950 and 875 cm^{-1} are assigned to the molybdyl stretching mode and the Mo-O-Mo stretching mode by comparison with aqueous hepta- and octamolybdate solutions, respectively. [28] The position of the two bands is almost independent of the Mo loading on the

surface, whereas their intensity increases with loading. The Raman bands at 380 cm^{-1} and 230 cm^{-1} can be assigned to molybdyl bending and Mo-O-Mo deformation modes. [29,131] The room temperature spectra of the dehydrated samples are depicted in Fig. 6.2. and 6.3. The Raman band around 875 cm^{-1} is absent and the molybdyl

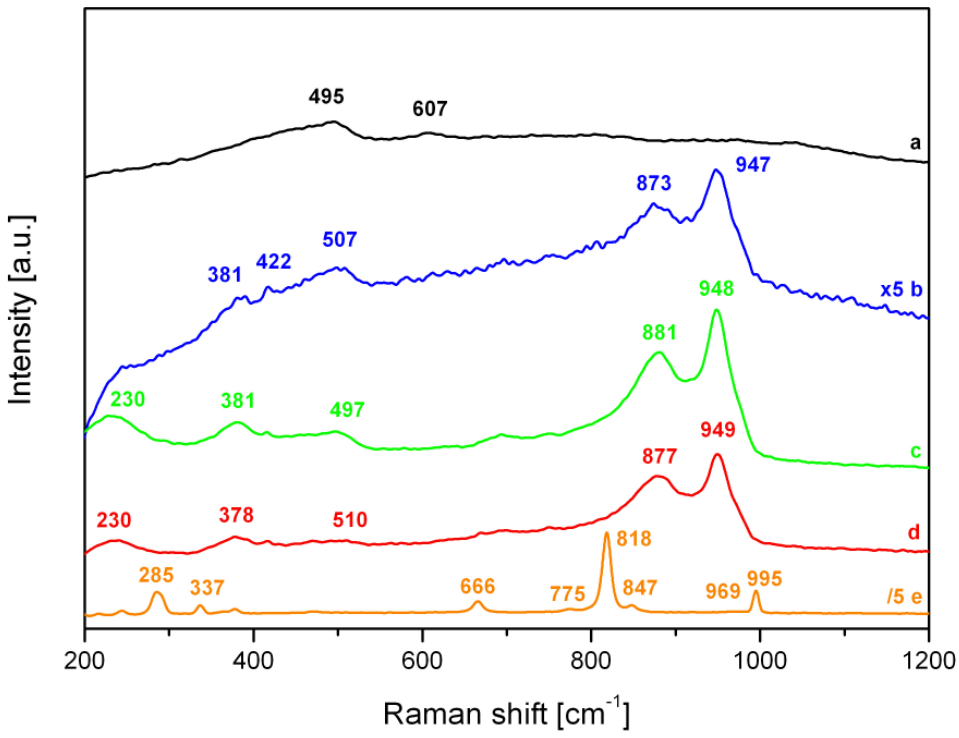

Fig. 6.1: Room temperature Raman spectra of hydrated (a) oxa/SBA-15 and Mo_xO_y/SBA-15 (b) 5.9 wt.% Mo / 0.8 Mo/nm^2; (c) 8.4 wt.% Mo / 1.5 Mo/nm^2 (d) 12.1 wt.% Mo / 3.5 Mo/nm^2 (e) 13.9 wt.% Mo / 6.8 Mo/nm^2. The spectra are offset for clarity.

vibration shifts to higher frequencies. Also the shape of the molybdyl band is altered. In the dehydrated state, it exhibits a flat top from 961 to 980 cm^{-1} at a Mo density of 0.8 Mo/nm^2. At higher Mo density a new band appears at 991 cm^{-1}, which shifts up to 996 cm^{-1} with increasing Mo density. The shift and the change of the band shape of the molybdenyl vibrations can be interpreted as an indication that the two bands belong to at least two different contributions of the present molybdenum oxide species. However,

there is no indication for the formation of crystalline MoO_3 as the characteristic bands at 666 and 819 cm^{-1} are missing up to 3.5 Mo/nm^2. The vibration of the molybdyl bending mode now appears at 361 cm^{-1}. At a high Mo density (6.8 Mo/nm^2), the characteristic

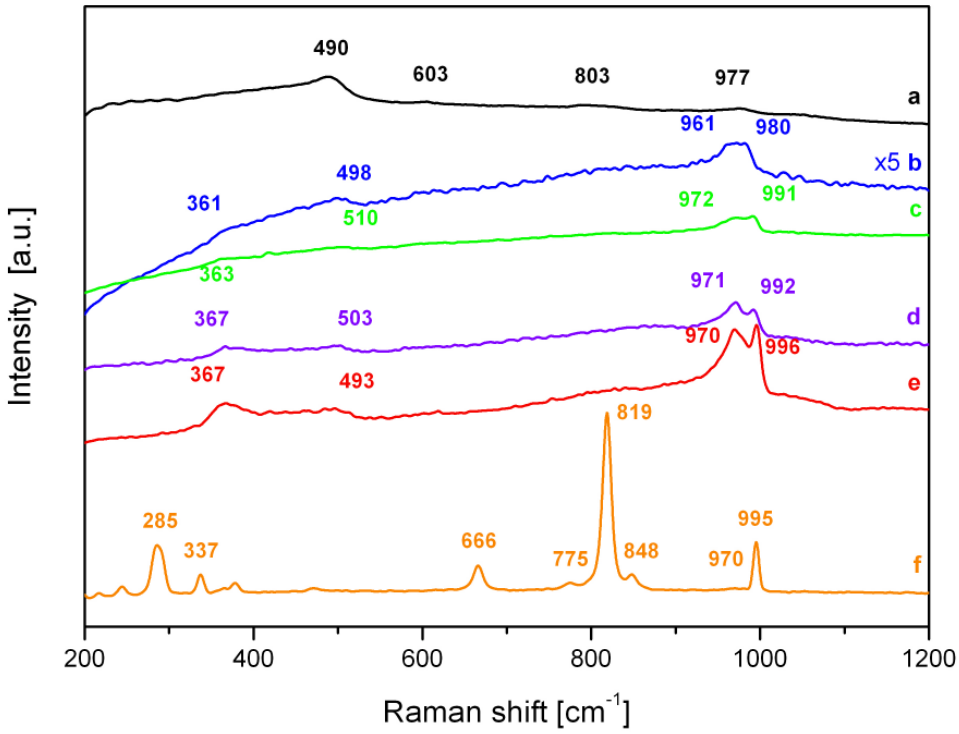

Fig. 6.2: Room temperature Raman spectra of dehydrated (a) oxa/SBA-15 and Mo_xO_y/SBA-15 (b) 5.9 wt.% Mo / 0.8 Mo/nm^2; (c) 8.4 wt.% Mo / 1.5 Mo/nm^2 (d) 11.0 wt.% Mo / 2.4 Mo/nm^2 (e) 12.1 wt.% Mo / 3.5 Mo/nm^2 (f) 13.9 wt.% Mo / 6.8 Mo/nm^2. The spectra are offset for clarity.

bands of crystalline α-MoO_3 [127] are clearly observed for both hydrated and dehydrated Mo_xO_y/SBA-15. Moreover, the bands at 775 and 847 cm^{-1} have previously been assigned to the presence small amounts of β'-MoO_3 [127] (see chapter 4.5.). In a study by Banares et al. the formation of β-MoO_3 has not been observed after synthesis, but during the performance of methanol oxidation on silica supported molybdenum oxide systems. [10]

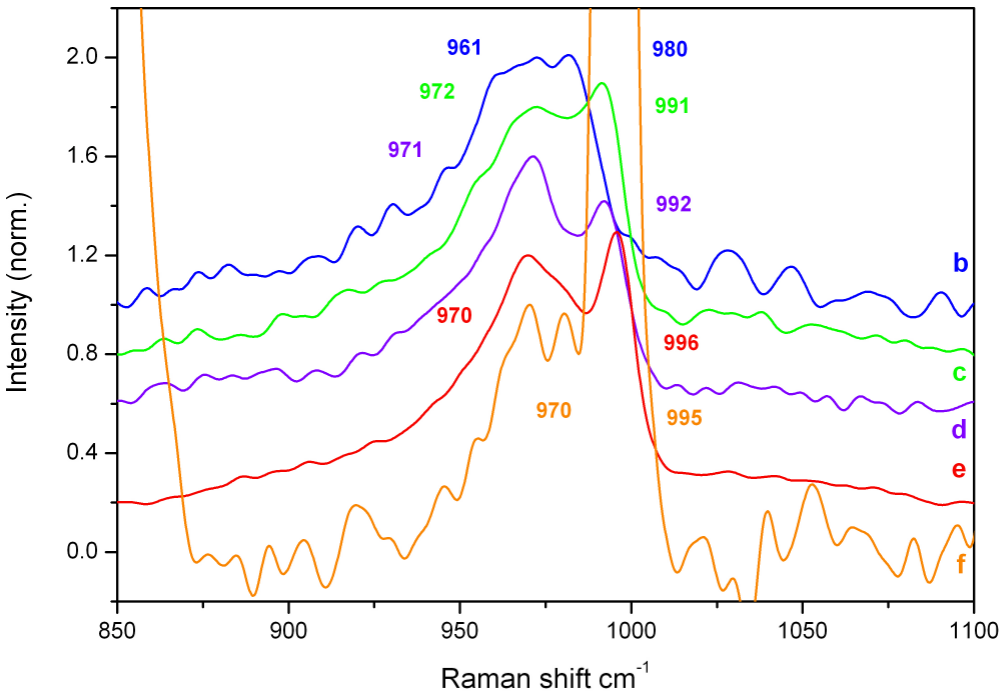

Fig. 6.3: Magnified region from 850 to 1100 cm^{-1} of Fig. 6.3. A linear background subtraction has been performed from 850 to 1100 cm^{-1}. The spectra are normalized with respect to the peak at 970 cm^{-1} and offset for clarity.

Figure 6.4 depicts the spectra of the dehydrated Mo_xO_y/SBA-15 samples at 500°C in dry flowing air. Below 900 cm^{-1}, the bands appear at the same positions as in case of room temperature spectra (see Fig. 6.1). As shown in Fig. 6.2 for a sample with a Mo density of 0.8 Mo/nm^2 (spectrum a) the region of the molybdyl band is characterized by a splitting into two components at 967 and 987 cm^{-1}. In case of the sample prepared by incipient wetness impregnation (0.6 Mo/nm^2, spectrum c), the molybdyl bands appear at very similar positions (965 and 983 cm^{-1}). Therefore, it can be concluded that the preparation procedure has only a small effect on the formed molybdenum oxide structures. If the Mo density is further decreased to 0.2 Mo/nm^2 only one band at 967 cm^{-1} with asymmetric shape is observed. Normalising the spectrum of oxa/SBA-15 as support reference at 500°C under dehydrated conditions to the D2 band at 605 cm^{-1} and

the symmetrical Si-O-Si stretching mode at 800 cm^{-1} of spectrum (b) reveals that the 967 cm^{-1} band has a large contribution of the Si-OH stretching mode at 965 cm^{-1}. The contribution of the Si-OH stretching mode has been fitted and plotted after re-addition of the linear background function into spectrum (b) for visualization.

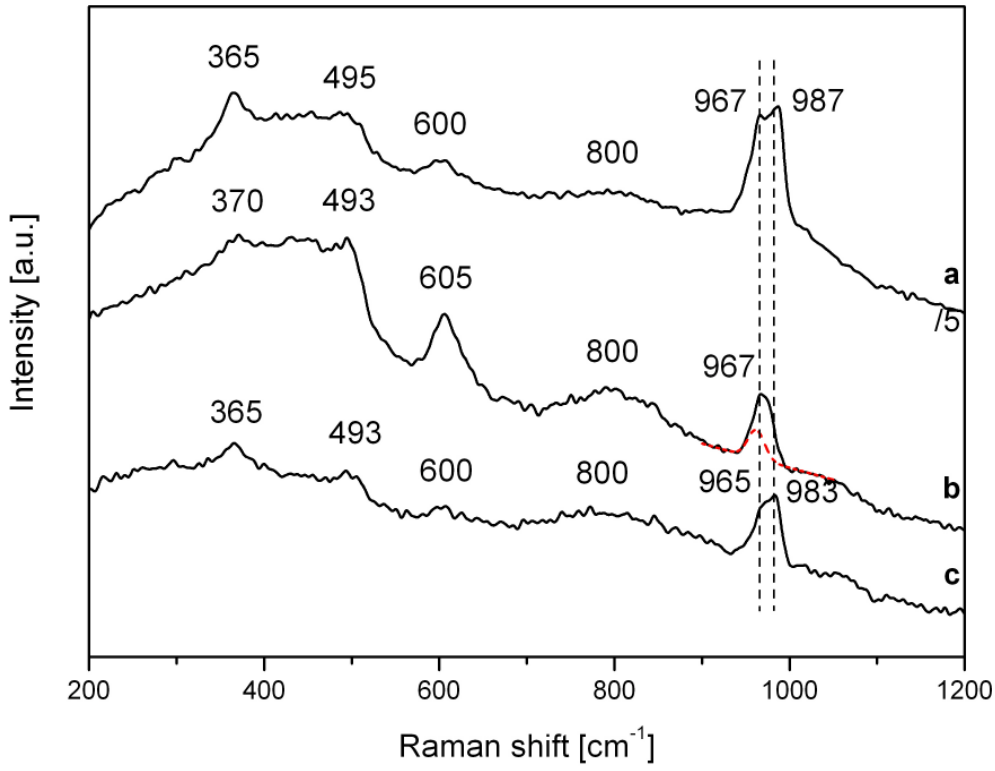

Fig. 6.4.: Raman spectra of Mo_xO_y/SBA-15 at 500°C in N_2/O_2 (80:20) flow at 50 ml/min (a) 5.9 wt.% Mo; 0.8 Mo/nm^2; (b) 1.0 wt.% Mo; 0.2 Mo/nm^2 (Fit of the Si-OH stretching (dotted red)) and (c) 5.5 wt.% Mo; 0.6 Mo/nm^2 (incipient wetness). The spectra are offset for clarity.

Previously, the two bands at 967 and 987 cm^{-1} have been assigned to the asymmetric and symmetric modes of a tetrahedral dimolybdyl species on the basis of DFT calculations. [31] Furthermore, a third mode at 1020 cm^{-1} was observed and assigned to the molybdyl vibration of a square pyramidal molybdenum oxide centre. [42] In a recent DFT study Gregoriades et al. used a more sophisticated, larger model to simulate silica supported mono molybdenum oxide centres and suggest instead that the assignment of

the two bands at 988 and 1020 cm^{-1} should be reversed. [132] Importantly, according to the latter assignment, the two main molybdyl bands at 967 and 987 cm^{-1} represent different molybdenum oxide species. An assignment of these two bands to different species is supported by the observation that the presence of steam significantly changes their intensity ratio. (chapter 6.8., Fig. 6.35) While detailed calculations for connected Mo_xO_y centres are not available and considering the fact that missing M-O-M Raman signatures do not necessarily mean the absence of connected centres, [46,47,133] the Raman spectra can not answer the question whether in the dehydrated state the surface molybdenum oxide species consist of isolated centres or connected centres or a mixture of both. Therefore, other techniques like X-ray absorption spectroscopy (XAS) (chapter 6.6. and 6.7.), IR Spectroscopy using nitric oxides as probe molecules (chapter 6.4.) and UV/Vis Spectroscopy (chapter 6.3.) have been employed.

6.3. UV/VIS Spectroscopy

Figures 6.5 and 6.6 show the UV/Vis spectra of hydrated and dehydrated Mo_xO_y/SBA-15 in the loading range of 5.9 to 19.9 wt.% Mo (0.8 to 6.2 Mo/nm^2). The absorption bands from 200 to 400 nm can be assigned to a ligand-metal charge transfer (O^{2-} to Mo^{6+}). [134] The hydrated samples (Fig 6.5) show a broad band with a maximum at 245 nm and an asymmetric shape towards higher wavelengths extending up to 370 nm. When the samples are first dehydrated at 400°C and cooled subsequently to room temperature for experiments, the shape of the spectra changes and their intensity decreases. For the dehydrated state the maximum of the CT-band is almost constant at 242 nm. (see Fig. 6.6) Additionally, a shoulder at 280 nm is visible, which is accompanied by a loss of relative intensity at wavelength over 300 nm compared to the band at 242 nm during dehydration.

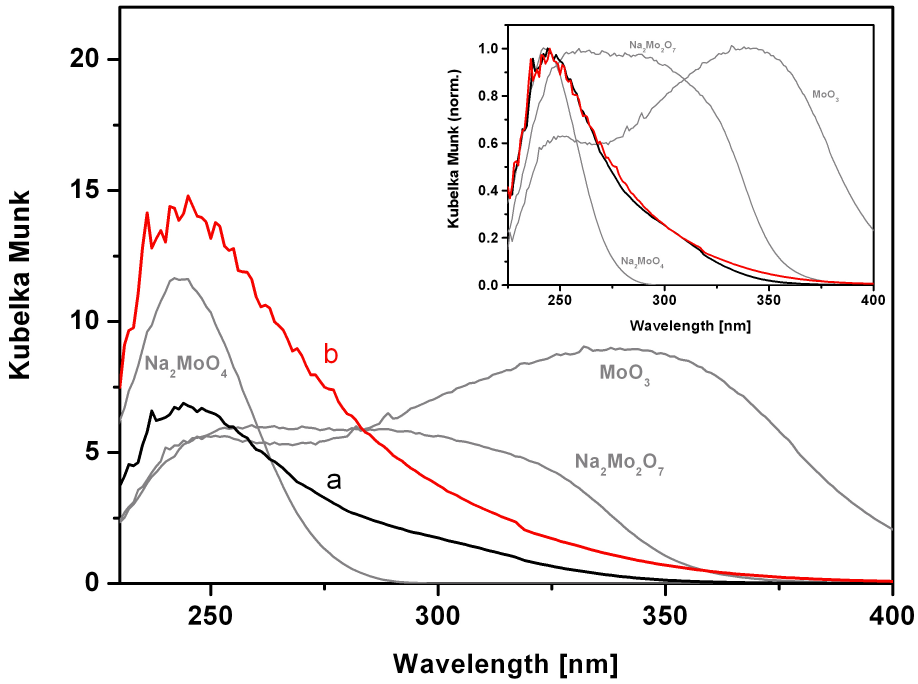

Fig. 6.5: UV/Vis spectra of Mo_xO_y/SBA-15 (a) 5.9 wt.% Mo (0.8 Mo/nm^2), (b) 11.1 wt.% Mo (2.0 Mo/nm^2) and reference compounds Na_2MoO_4 (e), $Na_2Mo_2O_7$ (f) and MoO_3 (g) in the hydrated state. The inset shows normalized spectra. [135]

The observed shape and band position in the hydrated and dehydrated spectra is in agreement with the literature. Lou et al. for instance reported for hydrated SBA-15 supported molybdenum oxide monomeric beside oligomeric species at a loadings of 0.6 Mo/nm^2. [36] The assignment was based on edge energies determined by a method proposed by Weber. [136] Wachs et al. examined dehydrated Cabosil supported molybdenum oxide in the Mo-density range of 0.1 to 2.2 Mo/nm^2 and reported also two typical bands at 230 and 275 nm, which have been assigned to isolated monomeric species [29,42]. The typical shape and band position is also frequently observed at lower densities of 0.1 to 0.4 Mo/nm^2 on other silica supports. [52,53]

Regarding the band assignment of silica supported molybdenum oxides several interpretations for the observed spectra can be found in the literature. As reference

compounds molybdates like ammonium heptamolybdate, sodium molybdate, sodium dimolybdate and crystalline molybdenum oxide have been used. In addition, the comparison with the molybdate species formed in aqueous solutions in dependence of the pH is quite common. Traditionally, absorption bands from 250 to 280 nm have been assigned to a tetrahedral and bands from 300 to 330 nm to an octahedral geometry of isolated molybdenum oxide centres [137]. If also connections between the centres are considered, the expected regions for both geometries may significantly deviate. Jezlorowski and Knözinger assigned the two contributions that have been observed at 230 to 240 nm to isolated tetrahedral and at 250 to 290 nm transitions to a bridging Mo-O-Mo structure. [138] Plyuto et al. attributed the region between 280 and 295 nm to octahedral species [139], while Song et al. assigned the region around 280 nm to tetrahedral species in the terminal position of oligomers. [9] Seyedmonir and Howe reported the region at 270 to 280 nm to be due to tetrahedral species, but were not able to distinguish between isolated and connected molybdenum oxide centres [140].

Thus there is a significant overlap of the spectral regions of tetrahedrally (230 to 295 nm) [138,141], octahedrally (270 to 330 nm) [137] coordinated species and connected molybdenum oxide centres (250 to 290 nm). [138] However, since the band gap between the HOMO and LUMO of the supported molybdenum oxide depends on the coordination sphere, condensation degree and dispersion UV absorption bands do not allow for a clear distinction of the local molybdenum oxide structures. [52,137,142]

Nevertheless, by comparison with reference substances, several exclusions for the present structures can be made. The spectra of Mo_xO_y/SBA-15 for the hydrated and dehydrated state show significant intensity at higher wavelength than the spectrum of Na_2MoO_4. Thus, even at Mo densities of 0.8 Mo/nm^2 it can be excluded that not only isolated tetrahedral species are present. The additional intensity at wavelengths ≥280 nm can be explained by the presence of a second species, which can be isolated octahedrals, connected tetrahedral or octahedral molybdenum oxide centres or a mixture of these

three species. The loss of intensity over 300 nm upon dehydration can be due to larger dispersion of the molybdenum oxide species.

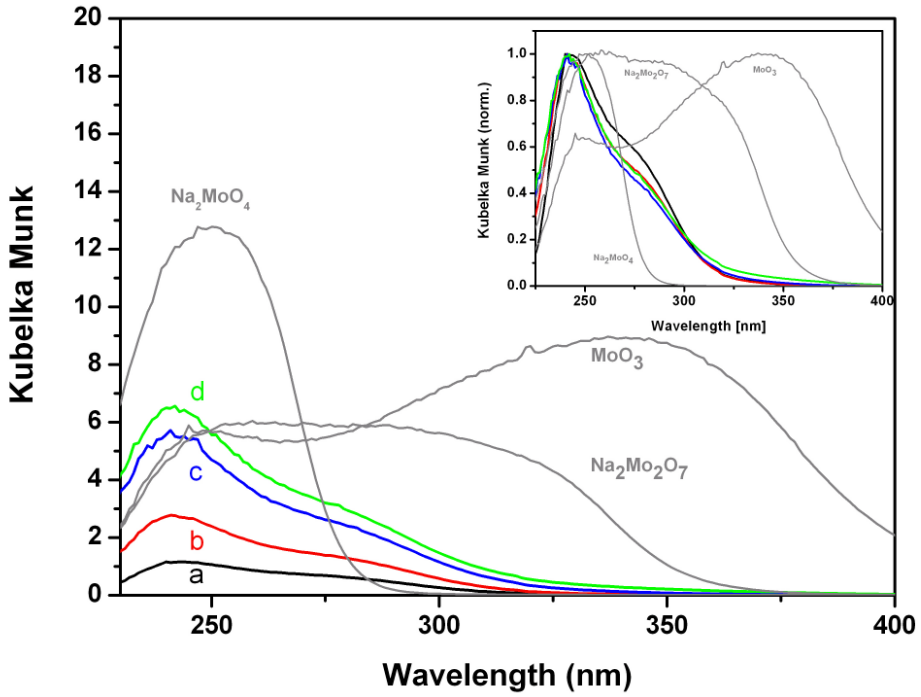

Fig. 6.6: UV/Vis spectra of Mo_xO_y/SBA-15 a) 5.9 wt.% Mo (0.8 Mo/nm^2), b) 11.1 wt.% Mo (2.0 Mo/nm^2), c) 13.9 wt.% Mo (3.2 Mo/nm^2), d) 19.9 wt.% Mo (6.2 Mo/nm^2) and reference compounds Na_2MoO_4 (e), $Na_2Mo_2O_7$ (f) and MoO_3 (g) in the dehydrated state. The inset shows normalized spectra.

Interestingly, the presence of crystalline MoO_3 at loadings of 13.9 and 19.9 wt.% Mo, as detected by Raman spectroscopy (see chapter 6.2.) has only a small contribution to the UV/Vis spectra as indicated by the absence of an intense band at 330 nm. The fraction of crystalline MoO_3 for these samples is approximately 2 and 8 wt.% Mo (see chapter 4.4.). Also the relative intensity and band position of the two contributions at 240 and 280 nm with the exception of the dehydrated spectra with a Mo density of 0.8 Mo/nm^2 is almost constant as can be seen in the insets of Fig. 6.5 and 6.6. An interpretation for the observed behaviour can be that the distribution of the present molybdenum oxide species is not changing significantly.

6.4. Electronic Structure Characterization by XPS

Figure 6.7 depicts a survey spectra of a dehydrated Mo_xO_y/SBA-15 sample with a loading of 5.7 wt.% Mo (0.8 Mo/nm^2). The most intense peaks at 103.6, 155.1, 234.0, 533.6, 747.6 can be assigned to the expected elements such as silicon, molybdenum and oxygen, respectively.

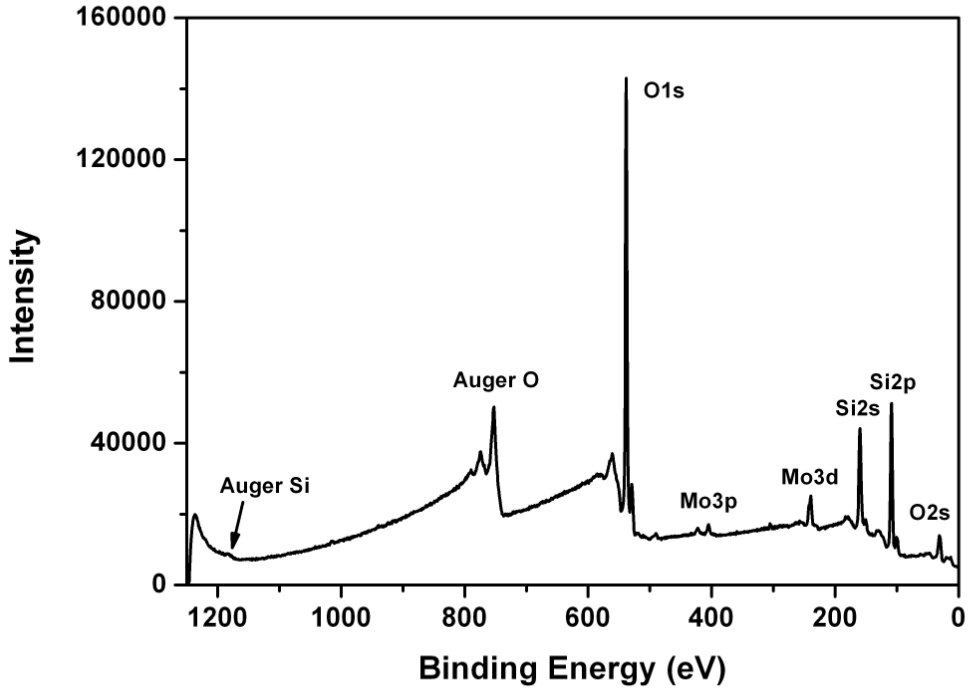

Fig 6.7: XP survey spectrum of 5.9 wt.% Mo (0.8 Mo/nm^2) Mo_xO_y/SBA-15 in the dehydrated state

The minor peaks at 529.3, 490.7 and 305.8 eV can be attributed to O $K_{\alpha,\beta}$ and Al K_α satellites from the X-ray source. Furthermore, only very little intensity was found in the C1s region around 285 eV, which shows that the tested samples are almost free of carbon impurities after the removal of the organic APTMS layer.

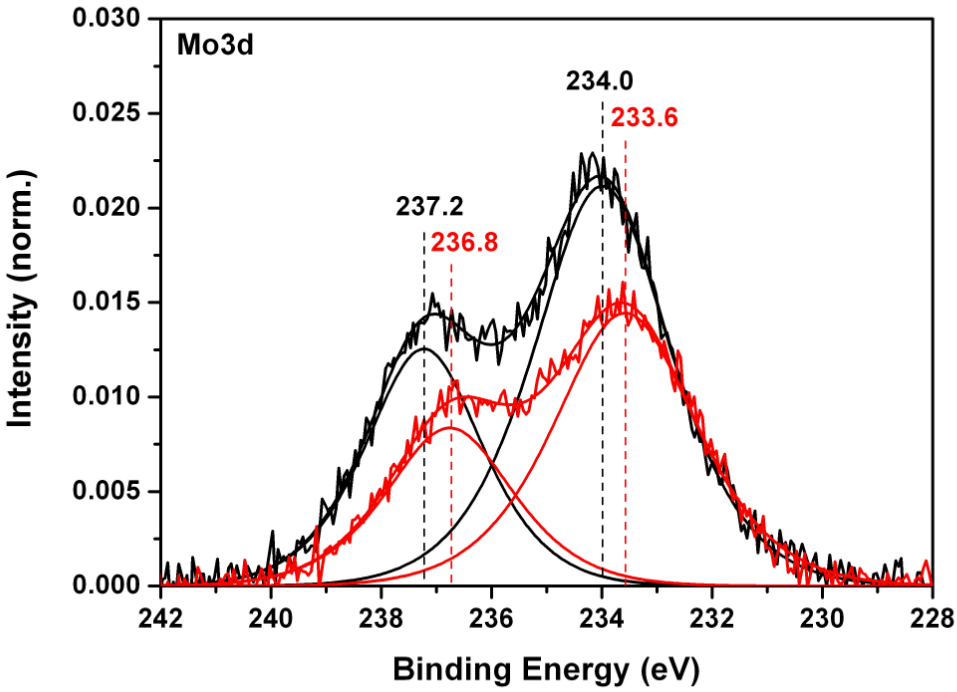

Fig 6.8: XP spectrum of the Mo 3d region of 5.7 wt.% Mo (0.8 Mo/nm^2) Mo_xO_y/SBA-15 in the dehydrated (black) and the hydrated state (red).

The Mo 3d region in the hydrated and dehydrated state of the Mo_xO_y/SBA-15 catalyst is depicted in Fig. 6.8. A good fit to the experimental data was obtained by using a single spin-orbit doublet, since the presence of another phase like crystalline MoO_3 was excluded by Raman spectroscopy. (see chapter 6.2) The area ratio of the fit curves was fixed to 3 : 2 ($3d_{5/2}$: $3d_{3/2}$) and the spin orbit splitting to 3.13 eV. [143] The FWHM was constrained to be the same for both components, but set free during the fitting procedure, being determined to be 2.8 eV. Since the spectrum shows a symmetric line shape and no shoulders at lower binding energies the presence of reduced Mo^{5+} (~231 eV) and Mo^{4+} (~229.5 eV) oxidation states seems to be negligible for supported Mo_xO_y species in hydrated and dehydrated state. [143-145] Furthermore, a shift to higher binding energies of 1.0 eV in the hydrated and 1.4 eV in the dehydrated state was observed compared to

bulk α-MoO_3 (Mo $3d_{5/2}$: 232.6 eV). [143] Since peaks of other elements like oxygen and silicon do not show a similar change of position, broadening or asymmetry charging and differential charging can be largely excluded to be the reason for the observed shift to higher binding energies. The shift is also detected for higher loaded samples. (see Table 6.2) A probable explanation for this behaviour can be the higher dispersion of the present Mo_xO_y species. [145,146] Moreover, the higher shift for the dehydrated state of the Mo 3d peaks indicates an increase of the dispersion during dehydration. A similar behaviour has also been observed for the V_xO_y/SBA-15 system. [147,148] The relatively broad FWHM of the peaks can be explained if a Mo_xO_y species distribution of different size is assumed.

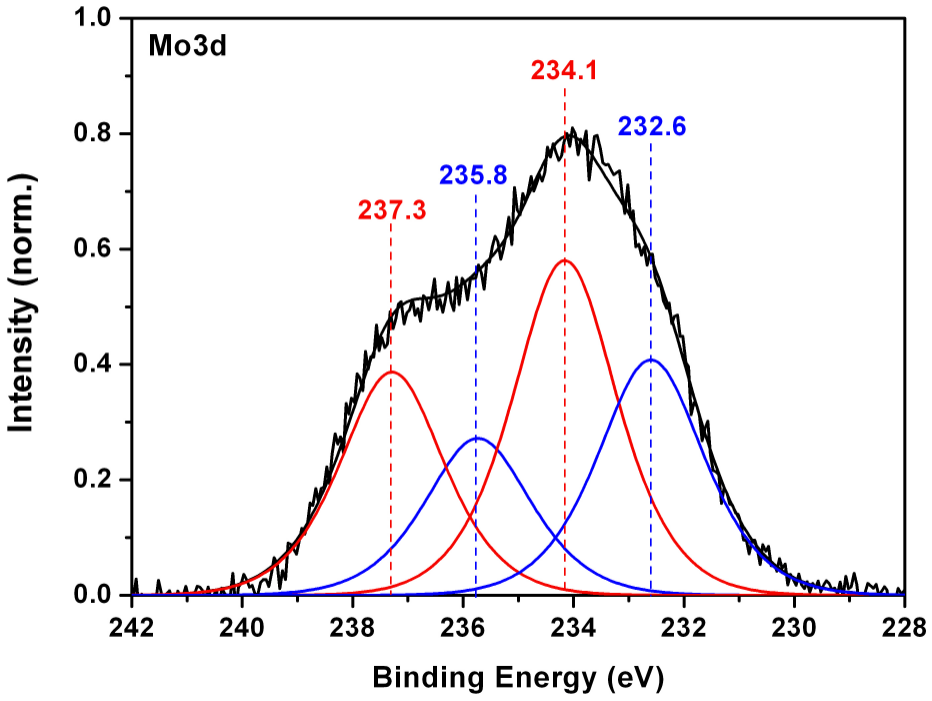

Fig 6.9.: XP spectrum of the Mo 3d region shows the contributions of dispersed Mo_xO_y species (red) and crystalline MoO_3 (blue) of 21.1 wt.% Mo (9.8 Mo/nm^2) Mo_xO_y/SBA-15 in the dehydrated state.

Table 6.2: Comparison of the Mo:Si ratios and Binding Energies of the Mo 3d 5/2 peak detected by XPS of Mo_xO_y/SBA-15 in the hydrated and dehydrated state.

Mo_xO_y/SBA-15	hydrated		dehydrated	
Mo loading [wt.%]	BE (Mo 3d 5/2) [eV]	Mo:Si ratio	BE (Mo 3d 5/2) [eV]	Mo:Si ratio
5.7	233.6	0.027	234.0	0.039
11.0	233.5	0.040	234.1	0.091
14.0	233.4	0.051	234.0	0.108
21.1	232.5	0.065	233.9	0.123

The described effects of dispersion and the shift after dehydration are also found for Mo_xO_y/SBA-15 samples with higher loadings. For samples like 21.1 wt.% Mo (9.8 Mo/nm^2) Mo_xO_y/SBA-15 (see Fig. 6.9), which contain crystalline MoO_3 the doublet structure of the Mo 3d peak is less distinct. Additionally, the formation of a shoulder in the Mo $3d_{5/2}$ peak can be observed. The shoulder can be explained by the presence of approximately 8 wt.% Mo crystalline MoO_3, which has been detected by Raman spectroscopy (chapter 6.1.) and quantified by a combination of XRF and EDX (chapter 4.4.). Thus a second doublet of fitting curves is necessary to obtain a good fit to the XP spectrum. The FWHM of the fitting curves was again a free parameter and found to be 2.5 eV. The area ratio of the dispersed Mo_xO_y species and the crystalline MoO_3 determined by XPS in the dehydrated state deviates about 15% from the ratio determined by XRF and EDX. The deviation may be a result of the larger error of the determination by curve fitting. The Mo:Si ratio is increasing linearly with Mo loading in the hydrated and dehydrated state. (Table 6.2) The only deviation from the linearity is observed for the sample with 21.1 wt.% Mo loading, which exhibits large α-MoO3 particles that can not be penetrated completely by XPS. (see chapter 4.5.) Furthermore the Mo:Si ratio of the dehydrated state is higher than in the hydrated state, which can be explained by a small moisture layer on the hydrated sample lowering the escape depth of the electrons from the Mo_xO_y/SBA-15 material.

6.5. Nitric oxide Adsorption and Oxidation on SBA-15 Supported Molybdenum Oxide Studied by Transmission IR Spectroscopy

6.5.1. Introduction

Alternatively to other frequently used classical spectroscopic techniques for the characterization of Mo_xO_y/SBA-15 like UV/VIS-, X-Ray Absorption- and Raman Spectroscopy, IR-Spectroscopy can give new insights into the structure of dispersed silica supported molybdenum oxides at low loadings (≤1.0 Mo/nm^2). [54] The direct observation of their IR bands is difficult due to intensive support bands and high absorption of most supports below 1300 cm^{-1}. [149] For this reason the adsorption of probe molecules, which have intense vibrations at wavenumbers higher than 1300 cm^{-1} is employed to study the structures of the supported molybdenum oxide species. It is known that on pre-reduced supported molybdenum oxides the adsorption of nitric oxide leads to the formation of molybdenum mono- and dinitrosyls. [37] The intensities of the molybdenum dinitrosyls [Mo^{4+}-$(NO)_2$] for instance can be used to calculate the angle between the nitrosyl ligands and therefore can give insight into the coordination state of the supported molybdenum oxide centres. [150] It is also possible to obtain further information about the coordinative environment by the adsorption of a NO/O_2 mixture or NO_2. In this manner nitrites and nitrates can be formed, which show characteristic well separated vibrations for the possible coordination geometries (monodentate, bidentate and bridging). [38]

6.5.2. Results and Discussion

For the IR examination of Mo_xO_y/SBA-15 samples with 5.9 wt.% Mo (0.8 Mo/nm^2) and 10.2 wt.% Mo (2.2 Mo/nm^2) loading were examined. Figure 6.10 shows a series of room temperature IR spectra of the reduced Mo_xO_y/SBA-15 sample during exposure to NO (max. 2 mbar). New bands are observed at 1806 and 1702 cm^{-1}, which increase in intensity with time. In case of isotopically labelled ^{15}NO the same behaviour is observed (see Fig. 6.11). However, the two bands are now shifted to 1779 and 1682 cm^{-1}, respectively.

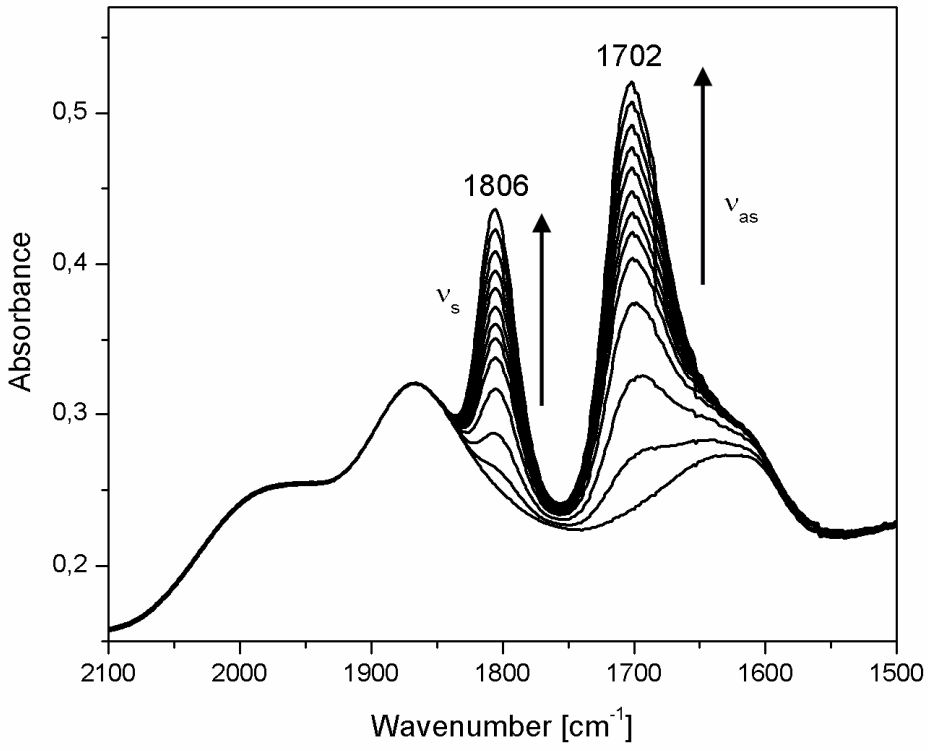

Fig. 6.10: Transmission IR spectra showing the formation of molybdenum dinitrosyl species [Mo^{4+}-$(NO)_2$] on reduced 5.9 wt.% Mo (0.8 Mo/nm^2) Mo_xO_y/SBA-15 during exposure to ^{14}NO at room temperature

The isotopic shifts of 27 and 20 cm^{-1} are consistent with expected shifts calculated within the harmonic oscillator approximation of 31 and 32 cm^{-1} for the ^{15}N-O stretching vibration. [38] Furthermore, ^{15}N labelled molybdenum dinitrosyls on alumina show similar vibrations at 1780 and 1675 cm^{-1}. [37] Therefore, in agreement with the literature, the bands at 1806 and 1779 cm^{-1} are assigned to the symmetric stretching vibrations $\nu_s(NO)$ and the bands at 1702 and 1682 cm^{-1} to the antisymmetric stretching vibrations $\nu_{as}(NO)$ of molybdenum dinitrosyls [Mo^{4+}-$(NO)_2$], respectively. [38] The bands at 1980, 1870 and 1630 cm^{-1} can be attributed to overtones of lattice vibrations of the SBA-15 support (see Fig. 6.10). [151]

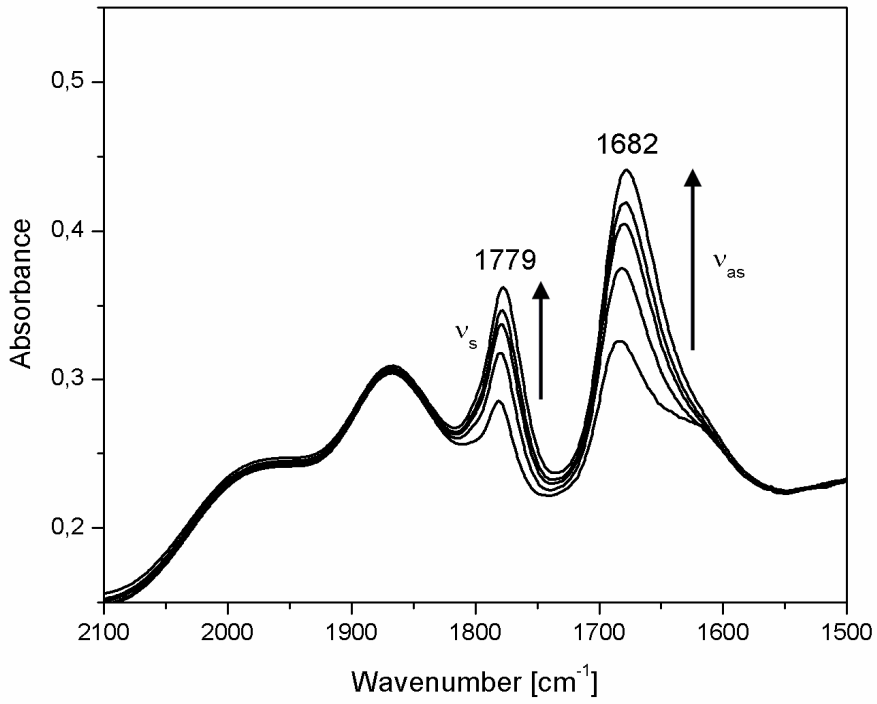

Fig. 6.11: Transmission IR spectra showing the formation of molybdenum dinitrosyl species [Mo^{4+}-$(NO)_2$] on reduced 5.9 wt.% Mo (0.8 Mo/nm^2) Mo_xO_y/SBA-15 during exposure to ^{15}NO at room temperature

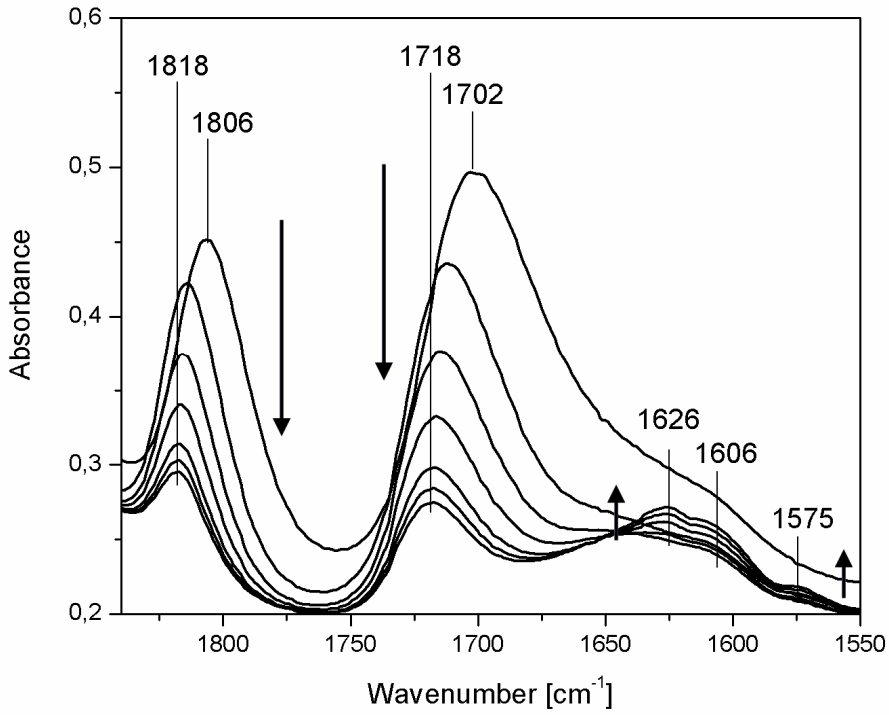

Fig. 6.12: Transmission IR spectra during exposure of the molybdenum dinitrosyl species $[Mo^{4+}\text{-}(NO)_2]$ on 5.9 wt.% Mo (0.8 Mo/nm^2) Mo_xO_y/SBA-15 to a mixture of NO (2 mbar) and O_2 (7.4 mbar). Note: The band at 1606 cm^{-1} is due to gas phase NO_2.

When the sample with the molybdenum dinitrosyl species is exposed to a mixture of ^{14}NO (2 mbar) and O_2 (7.4 mbar) the dinitrosyl bands decrease significantly in intensity and new bands appear at 1626, 1606 and 1575 cm^{-1} (see Fig. 6.12). As demonstrated previously for other silica supported transition metal oxide systems, [133] the presence of oxygen at room temperature may lead to the oxidation of nitrosyls accompanied by the formation of bands due to oxidation products of nitric oxide.

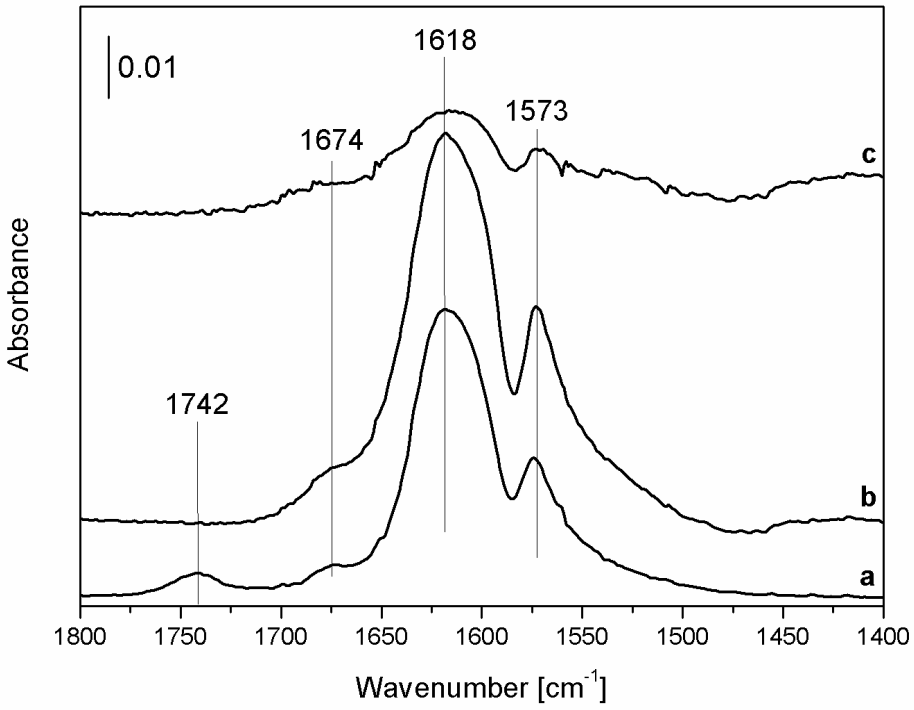

Fig. 6.13: Transmission IR difference spectra of oxidized 5.9 wt.% Mo (0.8 Mo/nm^2) Mo_xO_y/SBA-15 (a) after treatment with NO (2.0 mbar) and O_2 (7.3 mbar) at room temperature, (b) after treatment at 150°C followed by evacuation to 10^{-5} mbar at room temperature, (c) after treatment at 100°C at 10^{-5} mbar and subsequent cooling to room temperature. The spectra are offset for clarity.

As shown in Fig. 6.13, similar bands can also be formed directly on oxidized Mo_xO_y/SBA-15 samples in a NO/O_2 atmosphere without first generating intermediate molybdenum dinitrosyl species. The reaction of the silica hydroxyl groups with the NO/O_2 mixture causes also the formation of water, which leads to an intensity increase of the broad band due to hydrogen-bonded OH stretching of water around 3500 cm^{-1} (see Fig. 6.14) as well as the water bending mode contributing to the band at 1618 cm^{-1} (see Fig. 6.13), respectively. [152]

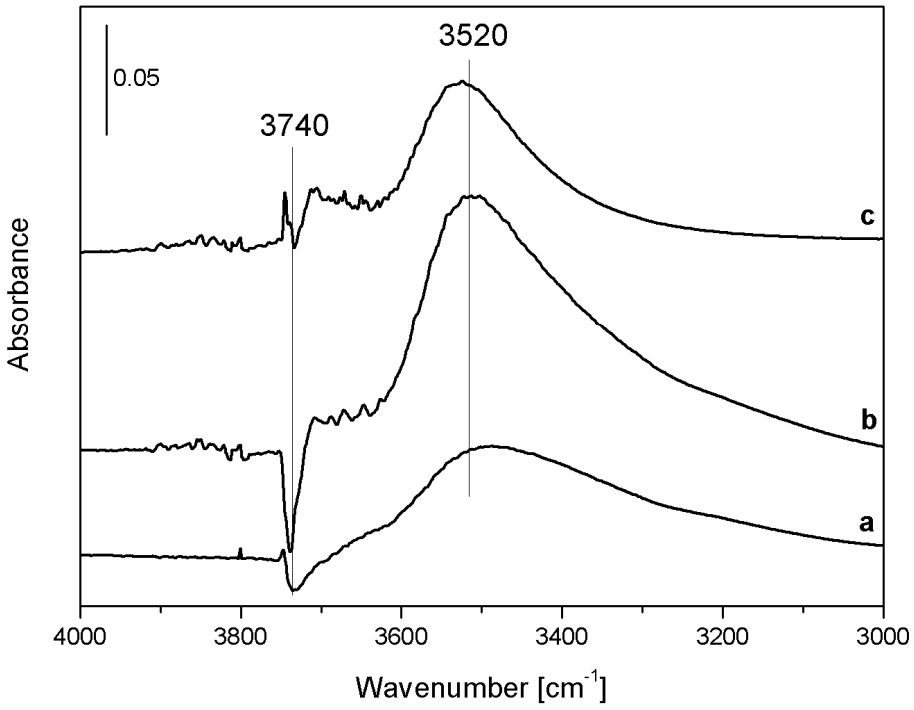

Figure 6.14: Transmission IR difference spectra of oxidized 5.9 Mo wt.% (0.8 Mo/nm^2) Mo_xO_y/SBA-15 (a) after treatment with NO (2.0 mbar) and O_2 (7.3 mbar) at room temperature, (b) after treatment at 150°C followed by evacuation to 10^{-5} mbar at room temperature, (c) after treatment at 100°C at 10^{-5} mbar and subsequent cooling to room temperature. The spectra are offset for clarity.

In the following, the assignment of the new IR bands at 1573, 1618, 1674 and 1742 cm^{-1} will be discussed. Table 6.3 summarizes spectral regions of nitrates and nitrites in different coordination geometry on supported transition metal oxide centres. [38] Table 6.3 is a literature survey of nitrogen oxide species, that may have been created on the Mo_xO_y/SBA-15 surface by oxidation in a NO/O_2 atmosphere.

Comparison with the data presented in Table 2 suggests that the new bands observed at 1573 and 1618 cm^{-1} (see Fig. 6.13) can possibly be associated with coordinated nitrates.

The presence of nitrites can readily be excluded as nitrites show no bands above 1520 cm^{-1}.

Table 6.3: Survey of IR signatures of NO_2^- and NO_3^- coordinated to supported metal oxide centres (Reproduced from Ref. 38)

Structure	ν_3 [cm^{-1}]		ν_1 [cm^{-1}]
free NO_3^--ion	1380		1050[a]
M-O-NO_2 (monodentate nitrate)	1480-1530	1250-1290	970-1035
M-O_2NO (bidentate nitrate)	1500-1565	1260-1300	1010-1040
$(M\text{-}O)_2$=NO (bridging nitrate)	1600-1650	1170-1225	1000-1030
free NO_2^--ion	1260		1330
$(M\text{-}O)_2$=N (bridging nitrite)	1205-1220		
M-NO_2 (nitro compound)	1335-1440		1315-1350
M-O-N-O (monodentate nitrite)	1450-1470		1050-1065
M-O | M-N-O (chelating nitro compound)	1390-1520		1180-1260

[a] not IR-active

However, there may be interference with other nitrogen oxides formed during the oxidation process. Characteristic bands of weakly bonded NO_2 and N_2O_4 have been detected at 1674 and 1742 cm^{-1} while treating the catalyst with NO and O_2 (see Fig. 6.13). The adsorption of other gaseous products like N_2O, N_2O_3 and N_2O_5 is not observed. As shown in Fig. 6.13, NO_2 and N_2O_4 largely desorb under reduced pressure conditions. The residual intensity around 1670 and 1520 cm^{-1} can be explained by insufficient background subtraction and does not occur in the experiment with isotopically labelled ^{15}NO (Fig. 6.16). In contrast, the bands at 1618 and 1573 cm^{-1} are stable under vacuum conditions and decrease only after heating to 100°C.

Table 6.4: Literature survey of IR bands of nitrogen oxides

Compound	Bands [cm^{-1}]	Ref.
N_2O	1285, 2224	153, 154
NO^-	1352-54	153, 154
$N_2O_2^-$ (cis)	1030, 1120, 1419	153, 154
(trans)	857, 1057, 1314	153
NO	1876	154
NO dimers:		
cis-$(NO)_2$	1760-85, 1863-70	153
trans-$(NO)_2$	1764	153
NO-NO	1690, 1778	153
NO^+	2390	153, 155
NO_2	1315, 1574, 1608, 1630	156
(weakly bonded)	1681	151
N_2O_3		
(O=N-NO_2)	1305, 1652, 1832	157
(O=N-O-N=O)	880, 970, 1660, 1690	157
N_2O_4	1710, 1745	151, 158
N_2O_5	743, 1338, 1728	159
NO^{2+}	2360-2392	153, 160

As depicted in Fig. 6.15 treatment of the bare silica oxa/SBA-15 support with ^{14}NO and O_2 leads to the occurrence of several nitrogen oxide bands. By comparison with the data shown in Table 6.3, the IR features at 1751 and 1716 cm^{-1} can be associated with adsorbed N_2O_4. The bands at 1625 and 1574 cm^{-1} are attributed to adsorbed NO_2, whereas the band at 1677 cm^{-1} is assigned to weakly adsorbed NO_2 (see Table 6.4). The origin of the feature at 1511 cm^{-1} is still under investigation. It is not observed in the case of Mo_xO_y/SBA-15. All these support-related bands disappear immediately under vacuum conditions except the band at 1574 cm^{-1}, which shows some residual intensity.

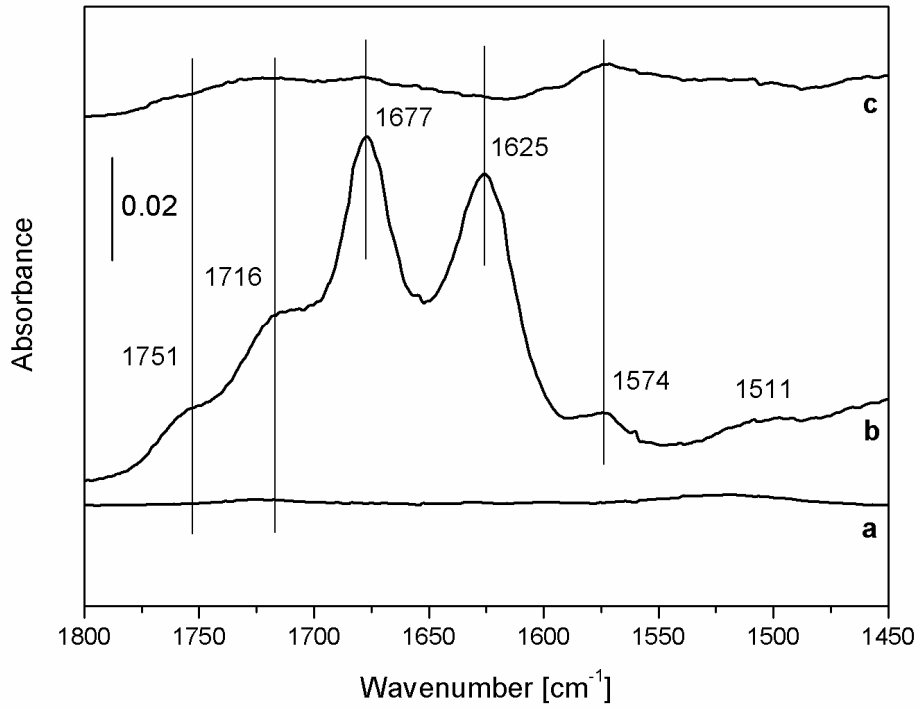

Fig. 6.15: Transmission IR difference spectra of oxidized oxa/SBA-15 (a) after treatment with NO (10.0 mbar), (b) after treatment with NO (2.0 mbar) and O_2 (8.0 mbar) at room temperature and (c) after evacuation to 10^{-5} mbar at room temperature. The spectra are offset for clarity.

However, in case of the bare silica support the intensity of this band is much smaller as for the Mo_xO_y/SBA-15 sample under the same vacuum conditions.

To exclude that the band at 1618 cm^{-1} is dominated by the bending mode of water, experiments with D_2O and ^{15}NO have been carried out. A D_2O exchange leads to a decrease of the H_2O bending mode at 1620 cm^{-1} and an increase of the HDO or D_2O bending modes at 1455 and 1200 cm^{-1}, respectively. [161] The total exchange of hydrogen with deuterium in the hydroxyl groups of Mo_xO_y/SBA-15 using D_2O was not possible even after six subsequent D_2O treatment and evacuation cycles. This is probably due to the porous structure of SBA-15, which besides mesoporous also

contains a significant amount of micropores. [76] Some of those pores might be sealed and not accessible for the deuterium exchange.

Table 6.5: Survey of IR adsorbate bands after exposure of 5.9 wt.% Mo (0.8 Mo/nm^2) Mo_xO_y/SBA-15 to $^{14}NO/O_2$ and $^{15}NO/O_2$

$\nu(^{14}N\text{-}O)$ [cm^{-1}]	$\nu(^{15}N\text{-}O)$ [cm^{-1}]	exp. shift [cm^{-1}]	calc. shift [cm^{-1}]	assignment
1742	1702	40	31	N_2O_4
1674	1640	34	30	NO_2
1618	1585	33	29	bridging nitratesa
1573	1534	39	28	bidentate nitrates

[a]Note: interference with the water bending mode at 1618 cm^{-1} has been excluded (for details see text).

As depicted in Fig. 6.16, adsorption of a ^{15}NO and O_2 mixture results in the appearance of IR bands at 1534, 1585, 1640 and 1702 cm^{-1}. The observed isotopic shifts of 31 to 39 cm^{-1} for ^{15}N-O stretching vibration are in agreement with the isotopic shifts of 28 to 31 cm^{-1} expected by the harmonic oscillator approximation for an isolated ^{15}N-O stretching mode (see Table 6.5). [37] The deviations result from the anharmonicity of the real potential curve and couplings with other modes within the formed molecules of nitrogen oxides. Also the intensity pattern of the bands is relatively similar to that after the adsorption of ^{14}NO and O_2.

Therefore, the feature at 1702 cm^{-1} can be assigned to $^{15}N_2O_4$. [162] The band at 1640 cm^{-1} is attributed to $^{15}NO_2$ as it shows an isotopic shift of 34 cm^{-1}, which is in the same range like that observed for gas phase nitrogen dioxide of 38 cm^{-1}. [163] The shoulder of the band at 1585 cm^{-1} to higher wavenumbers can be explained by a contribution of the water bending mode at 1620 cm^{-1}. However, as the feature is not pronounced after $^{15}NO/O_2$-treatment and decreases significantly after evacuation, it can be concluded that

the water bending mode can be excluded as the primary source for the band observed in case of $^{14}NO/O_2$ adsorption.

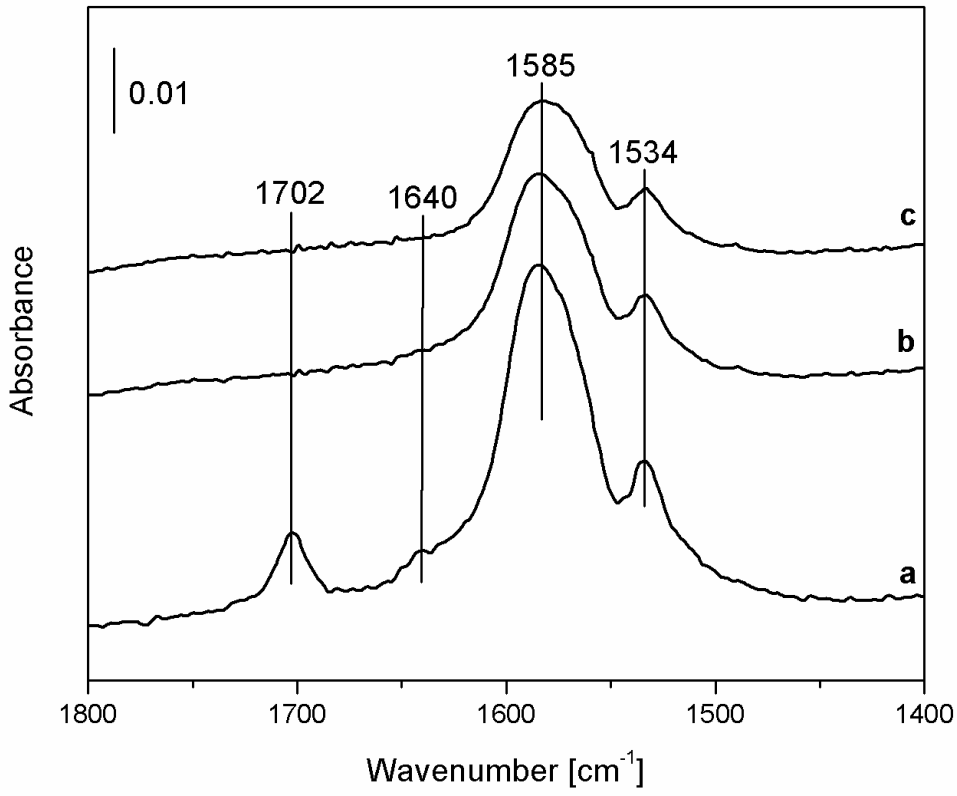

Fig. 6.16: Transmission IR difference spectra of oxidized 5.9 wt.% Mo (0.8 Mo/nm^2) Mo_xO_y/SBA-15 (a) after treatment with ^{15}NO (6.1 mbar) and O_2 (2 mbar), (b) after evacuation to $4 \cdot 10^{-5}$ mbar at room temperature (c) after evacuation to $1.4 \cdot 10^{-5}$ mbar at room temperature. The spectra are offset for clarity.

For the bands at 1618 and 1573 cm^{-1} (see Fig. 6.13) isotope shifts to 1585 and 1534 cm^{-1} are observed, respectively. While the isotope shifts prove the presence of nitrogen containing species, their magnitude is fully consistent with the presence of nitrogen oxide species. By comparison with the data shown in Table 2, the bands at 1618 cm^{-1} (see Fig. 6.12) and 1585 cm^{-1} (see Fig. 6.16) can readily be attributed to bridging nitrates and the bands at 1573 cm^{-1} (see Fig. 6.14) and 1534 cm^{-1} (see Fig.

6.16) to bidentate nitrates. [162] The findings and interpretation for the sample with 5.9 wt.% Mo (0.8 Mo/nm^2) loading are also supported by results for a higher loaded sample with 10.2 wt.% Mo (2.2 Mo/nm^2), which shows bands in similar position like the low loaded sample. (see Fig. 6.16) A scheme of the possible bridging and bidentate nitrates, which have been detected by FTIR spectroscopy is given in Fig. 6.18. Table 6.4 summarizes the assignments discussed above.

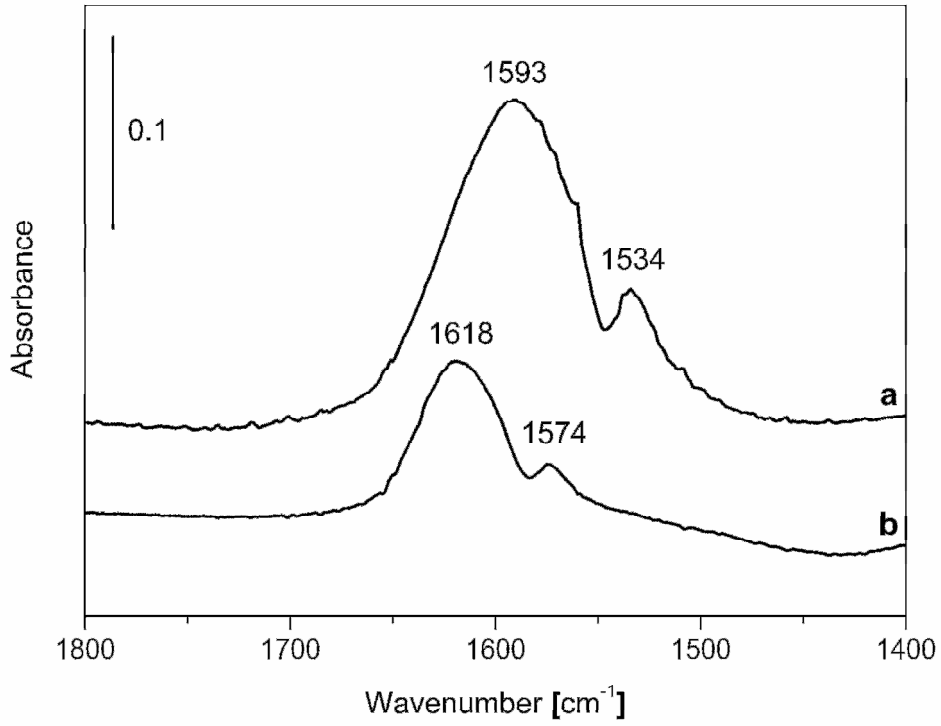

Fig. 6.17: Transmission IR difference spectra of oxidized MoxOy/SBA-15 with a loading of 10.2 wt.% Mo (2.2 Mo/nm^2) (a) after treatment with ^{15}NO (6.1 mbar) and O_2 (2 mbar) and evacuation to $1.4 \cdot 10^{-5}$ mbar at room temperature (b) after treatment with ^{14}NO (6.1 mbar) and O_2 (2 mbar) and evacuation to $2.2 \cdot 10^{-5}$ mbar at room temperature. The spectra are offset for clarity.

The formation of bridging nitrates on oxidized Mo_xO_y/SBA-15 is a valuable hint for the existence of proximate, connected MoO_x species. Thus, our data reveals that on SBA-15

a distribution of surface molybdenum oxide species of different size is present even at low Mo densities. Such a scenario also resolves the issue of partly conflicting literature results on the structure of silica supported molybdenum oxide as described in the introduction. Similarly, the presence of dimeric/oligomeric besides monomeric centers has recently been reported for SBA-15 supported vanadium oxide (0.7 V/nm^2). [45,46,133]

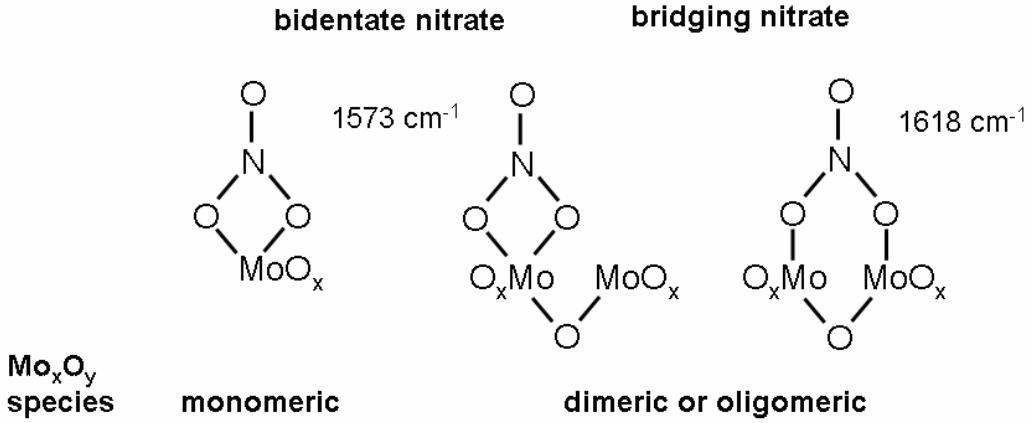

Fig. 6.18: Coordinated nitrates present on Mo_xO_y/SBA-15 after exposure to a $^{14}NO/O_2$ mixture and evacuation

The above results demonstrate that transmission IR spectroscopy using probe molecules is a valuable tool to indicate connectivity between supported metal oxide centres and to contribute to the ongoing discussion about the structure(s) of supported metal oxide species at low metal oxide densities.

6.5.3. Conclusions

The coordination geometry of NO and nitric oxides formed in the oxidation of NO by O_2 on silica SBA-15 supported dispersed molybdenum oxide with a loading of 5.9 wt.% Mo (0.8 Mo/nm^2) and 10.2 wt.% Mo (2.2 Mo/nm^2) have been studied by IR

transmission spectroscopy. NO treatment of previously reduced Mo_xO_y/SBA-15 in hydrogen leads to the formation of molybdenum dinitrosyl complexes [Mo^{4+}-$(NO)_2$]. The use of ^{15}NO results in a shift of the dinitrosyl bands from 1806 and 1702 cm^{-1} to 1779 and 1682 cm^{-1}, respectively. Using a NO/O_2 mixture to generate higher nitric oxides leads to the formation of bands at 1618 and 1573 cm^{-1}, which are stable under vacuum conditions. After treatment with $^{15}NO/O_2$ these bands show an isotope shift to 1585 and 1534 cm^{-1}, respectively. By comparison with the literature, the interference with other nitric oxides can be excluded. Besides the isotopic shift shows that the water bending mode at 1620 cm^{-1} can be excluded as source for the band at 1618 cm^{-1}. The bands at 1618 and 1585 cm^{-1} are assigned to bridging nitrates, whereas the bands at 1573 and 1534 cm^{-1} to bidentate nitrates. The presence of bridging surface nitrates implies the existence of dimeric or oligomeric molybdenum oxide surface species besides monomers on Mo_xO_y/SBA-15.

Table 6.6: Survey of all observed IR adsorbate bands on Mo_xO_y/SBA-15

	ν [cm^{-1}]	vacuum stability	assignment
Fig. 6.9	1806	yes	$Mo(NO)_2$ (ν_s)
	1702	yes	$Mo(NO)_2$ (ν_{as})
Fig. 6.10	1779	yes	$Mo(NO)_2$ (ν_s)
	1682	yes	$Mo(NO)_2$ (ν_{as})
Fig. 6.11	1806	yes	$Mo(NO)_2$ (ν_s)
	1802	yes	$Mo(NO)_2$ (ν_{as})
	1626	yes	mixture of NO_2 and bridging nitrates[a]
	1606	no	NO_2
	1575	yes	mixture of NO_2 and bidentate nitrates
Fig. 6.12	1742	no	N_2O_4
	1674	no	NO_2
	1618	yes	bridging nitrates[a]
	1573	yes	bidentate nitrates
Fig. 6.13	3740	yes	Si-OH
	3520	yes	H_2O
Fig. 6.14	1751	no	N_2O_4
	1716	no	N_2O_4
	1677	no	weakly adsorbed NO_2
	1625	no	NO_2
	1574	no	NO_2
	1511	no	n.a.[b]
Fig. 6.15	1702	no	N_2O_4
	1640	no	NO_2
	1585	yes	bridging nitrates
	1534	yes	bidentate nitrates

Fig. 6.16	1618	yes	bridging nitrates[a]
	1574	yes	bidentate nitrates
	1593	yes	bridging nitrates
	1534	yes	bidentate nitrates

[a]Note: interference with the water bending mode at 1618 cm^{-1} has been excluded (for details see text).
[b]Assignement of this band is still under investigation.

6.6. Structure of Silica SBA-15 Supported Molybdenum Oxide Studied by X-Ray Absorption Spectroscopy

6.6.1. Introduction

For the structure of silica supported molybdenum oxide at low Mo densities (≤1.0 Mo/nm^2), on the basis of EXAFS analysis, several somehow contradictory results are found in the literature. On the one hand, it is reported that only isolated molybdenum oxide species should be present in the dehydrated state. The discussion in those publications for the present species is mainly focused on the point whether isolated dioxo, monooxo or octahedral centres are present on the support. [30,31,33,131] On the other hand, the detection of connected molybdenum oxide centres is reported in other studies. Bensch and Ressler for instance concluded that on SBA-15 supported molybdenum oxide (0.9 Mo/nm^2) hexagonal MoO_3 like species should be present. [34,35] Moreover, Iwasawa et. al. described a dimeric molybdenum oxide structure (0.1 and 0.3 Mo/nm^2) to be present on silica. [48,49]

The following section shows that the literature picture about the structure of silica supported dispersed molybdenum oxide is incomplete and gives some substantial new insight to the debate. Therefore, the molybdenum oxide structure at a very low Mo density of 0.2 compared to 0.8 Mo/nm^2 and the dependence of the final structure from the molybdenum precursor used preparation is discussed.

6.6.2. Results and Discussion

The XAS χ(k) data of dehydrated Mo_xO_y/SBA-15 with a loading of 1.0 and 5.5 wt.% Mo (0.2 and 0.6 Mo/nm^2) are depicted in Figure 6.19. The good signal-to-noise ratio of the XAS data allowed a detailed XAFS analysis of the sample with 5.5 wt.% Mo loading in the k range from 4 to 14 Å^{-1} which will be described in the following.

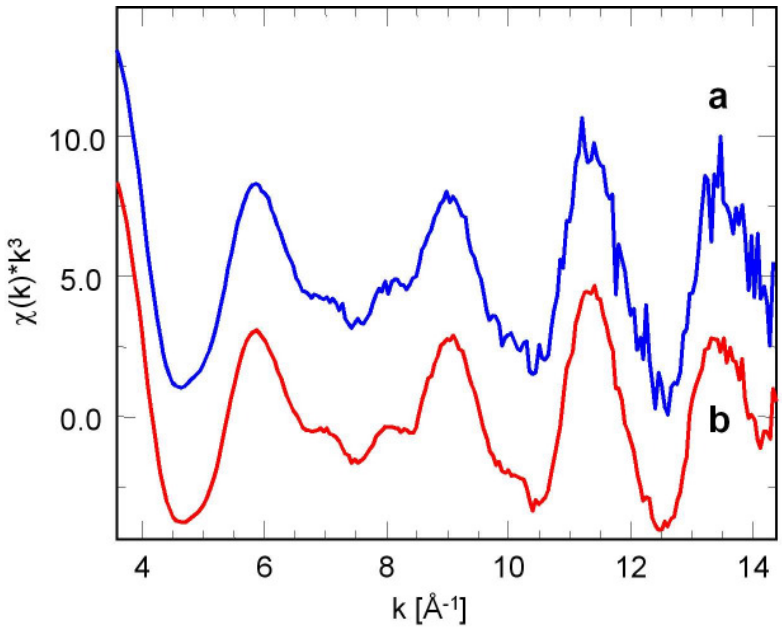

Fig. 6.19: Mo K edge XAFS χ(k) of dehydrated Mo_xO_y/SBA-15 with (a) 1.0 Mo wt.%; 0.2 Mo/nm^2 and (b) 5.5 Mo wt.% (0.6 Mo/nm^2) after thermal treatment in 20 vol.% O_2 in He at 623 K. The spectra are offset for clarity.

Figure 6.20 shows the Mo K near-edge (XANES) spectra of the two Mo_xO_y/SBA-15 with 1.0 and 5.5 Mo wt.% loading in the dehydrated state. A comparison of the XANES and XAFS regions of the spectra in Figure 6.19 and 6.20 shows that the spectra appear to be very similar for both loadings, which indicates that the local structure around the Mo centres is similar as well. Therefore, in this density range, according to XAS, the

local structure of the molybdenum oxide species seems to be independent of the molybdenum loading. For vanadium oxide species supported on SBA-15 at a comparable density range, a similar behaviour was described. [47] Because of the better XAFS data quality, the discussion of the structural analysis will be focused on the sample with 5.5 Mo wt.% loading in the following.

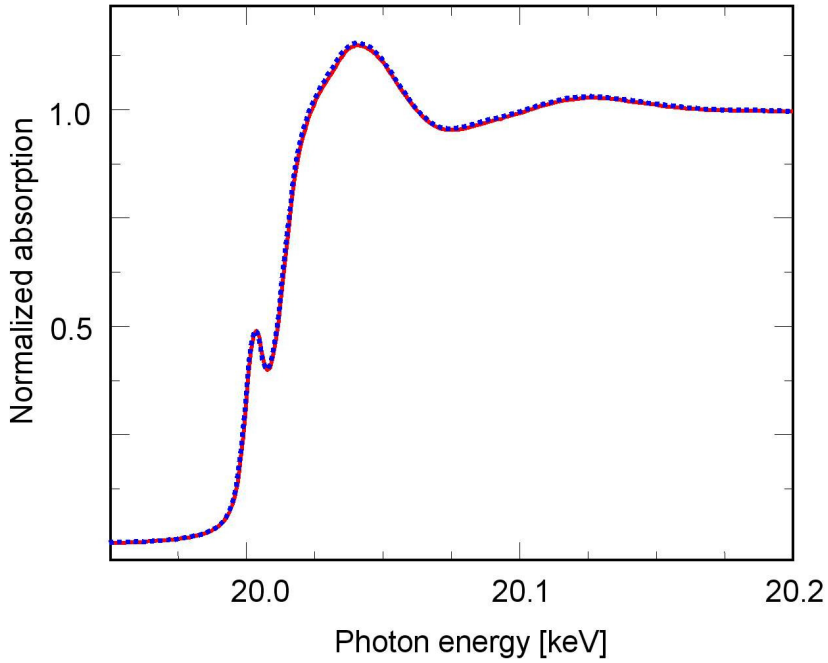

Fig. 6.20: Mo K edge XANES spectra of dehydrated Mo_xO_y/SBA-15 with 5.5 Mo wt.% (0.6 Mo/nm^2) [solid] and 1.0 Mo wt.% (0.2 Mo/nm^2) [dotted].

Figure 6.21 shows the development of Mo K edge Fourier transformed XAFS χ(k) functions (FT(χ(k)·k^3)) of Mo_xO_y/SBA-15 during thermal treatment in oxygen. The dehydration was done at a heating rate of 5 K/min in 20 vol.% O_2 in He in a temperature range of 300 to 623 K.

During thermal treatment, a characteristic structural transformation from the hydrated into the dehydrated state of Mo_xO_y/SBA-15 was observed, which was accompanied by the loss of water at ~100°C (see Fig. 6.22). [34] In the first Mo-O coordination sphere, distinct changes can be observed, which indicate a change in coordination geometry or

Mo-O distance distribution. Furthermore, higher Mo-Mo shells show a decrease in amplitude, which can be interpreted as an increase in dispersion of the supported molybdenum oxide species after thermal treatment. In the dehydrated state of Mo_xO_y/SBA-15, the pronounced peak at ~3 Å in the FT(χ(k)·k^3) indicates that Mo-Mo distances of oligomeric Mo_xO_y species supported on SBA-15 are still present. Therefore, the exclusive presence of isolated tetrahedral MoO_4 units in the local structure of the dehydrated Mo_xO_y/SBA-15 can be excluded.

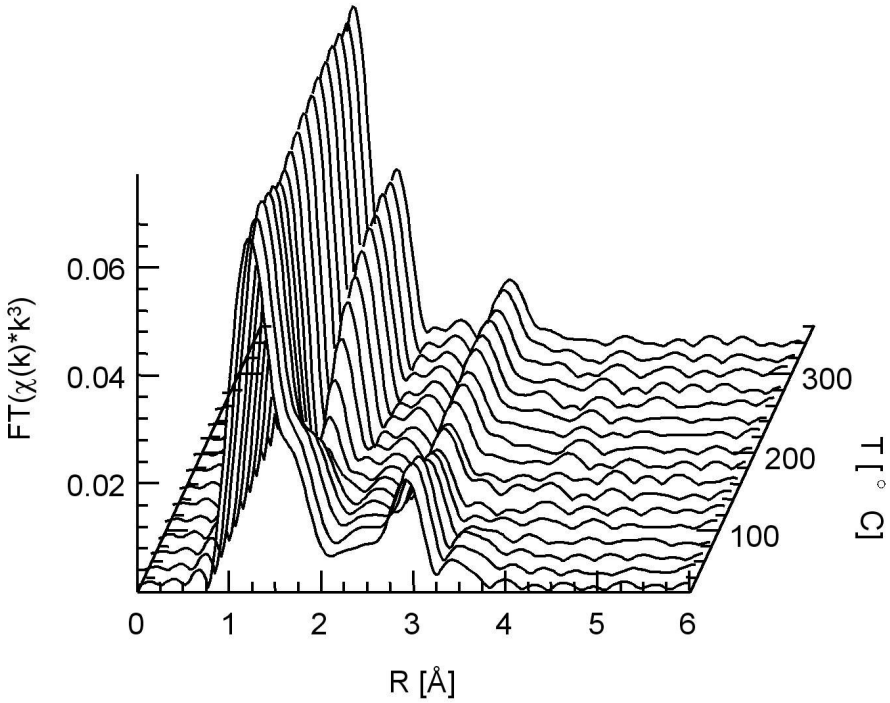

Fig. 6.21: Evolution of Mo K edge FT(χ(k)·k^3) of Mo_xO_y/SBA-15 with 5.5 Mo wt.% (0.6 Mo/nm^2) during thermal treatment in 20 vol.% O_2 in He in the temperature range from 300 to 623 K (5 K/min).

In Figure 6.23 the Mo K XANES and FT(χ(k)·k^3) of Mo_xO_y/SBA-15 in the hydrated and dehydrated state are compared to bulk molybdenum oxide references. As no phase shift correction has been carried out for the Fourier transformed XAFS χ(k)·k^3, the distances in the FT(χ(k)·k^3) are shifted by ~0.4 Å to lower values compared to crystallographic distances.

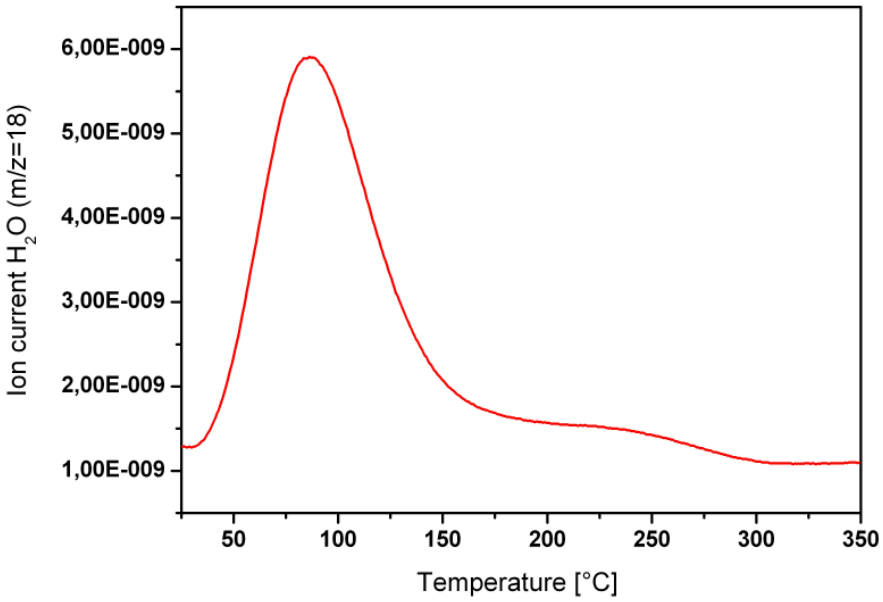

Fig. 6.22: Mass trace of water (m/z=18) during thermal treatment of Mo_xO_y/SBA-15 with 5.5 Mo wt.% (0.6 Mo/nm^2) in 20 vol.% O_2 in He in the temperature range from 300 to 623 K (5 K/min).

The XANES spectrum of the hydrated Mo_xO_y/SBA-15 was found to be similar to that of α-MoO_3 and the corresponding FT(χ(k)·k^3) to that of hexagonal MoO_3. A similar result has also been reported by Ressler et al..[34] In comparison to the reference oxide, the reduced amplitude may be explained by an increased disorder of the Mo_xO_y-phase or a reduced extension of the SBA-15 supported molybdenum oxide species.

The XANES spectrum of dehydrated Mo_xO_y/SBA-15 show an increased pre-edge peak which is comparable to references containing tetrahedral MoO_4 building blocks like Na_2MoO_4 or $Na_2Mo_2O_7$. Therefore, the pre-edge peak indicates a contribution of tetrahedrally coordinated molybdenum oxide centres present on the SBA-15 support. The FT(χ(k)·k^3) of dehydrated Mo_xO_y/SBA-15 shows a significant amplitude at higher Mo-Mo shells and a clear splitting of the first Mo-O shell. In contrast, the FT(k)·k^3) of Na_2MoO_4, which consists of tetrahedral MoO_4 building blocks, shows almost no signal at Mo-Mo distances and only one single Mo-O peak. Thus, it can be concluded that the

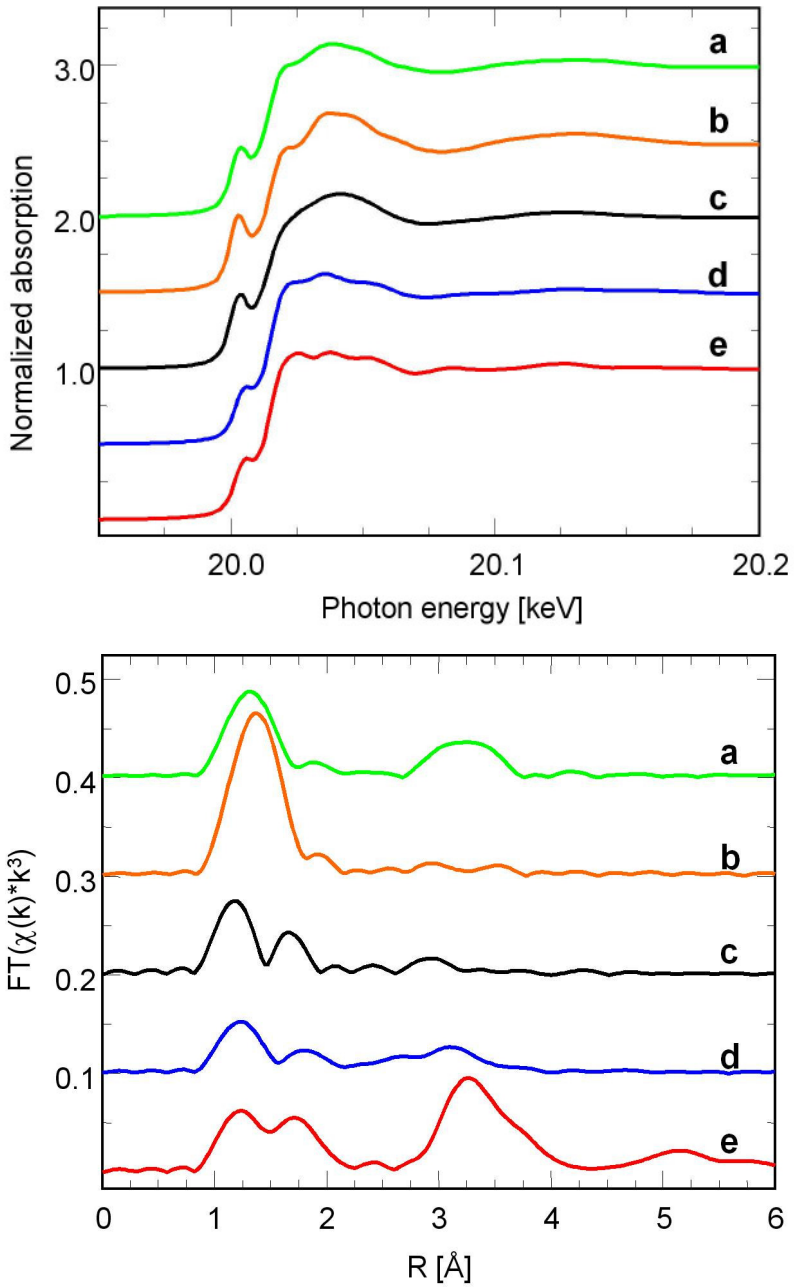

Fig. 6.23: Mo K edge XANES spectra [top] and Mo K edge FT($\chi(k)\cdot k^3$) [bottom] of (c) dehydrated and (d) hydrated Mo_xO_y/SBA-15 (5.5 Mo wt.% / 0.6 Mo/nm^2) together with reference oxides (a) $Na_2Mo_2O_7$, (b) Na_2MoO_4, (e) α-MoO_3. The spectra are offset for clarity.

characteristic FT($\chi(k)\cdot k^3$) of dehydrated Mo_xO_y/SBA-15 originates from a mixture of MoO_4 tetrahedrons and polymeric Mo_xO_y species.

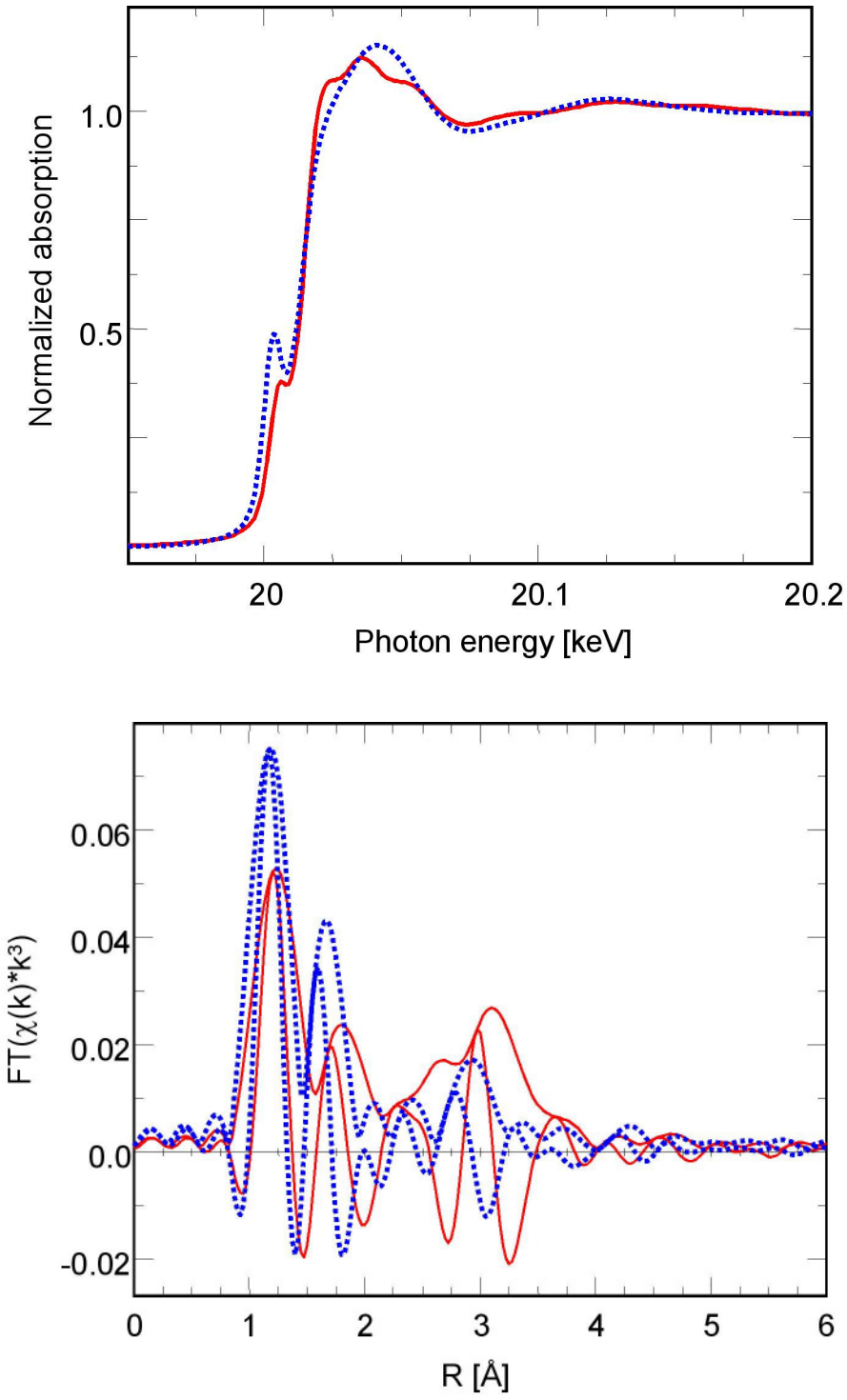

Fig. 6.24: Direct comparison of [top] Mo K edge XANES spectra and Mo K edge FT(χ(k)·k^3) [bottom] of hydrated [solid] and dehydrated Mo_xO_y/SBA-15 with 5.5 Mo wt.% (0.6 Mo/nm^2) [dotted].

A comparison of the Mo K edge XANES and FT(χ(k)·k^3) of Mo_xO_y/SBA-15 in the hydrated and dehydrated state is depicted in Figure 6.23. A transition from a α-MoO_3 type XANES in the hydrated state to a XANES similar to that of Na_2MoO_4 or $Na_2Mo_2O_7$ is observed. In contrast, the XANES in the dehydrated state is almost featureless, which can be attributed to an increased dispersion of the molybdenum oxide species on the support. The pre-edge peak in the Mo K edge XANES of hydrated Mo_xO_y/SBA-15 and α-MoO_3 is assigned to distorted octahedral MoO_6 units in both structures. The increase of the pre-edge peak of dehydrated Mo_xO_y/SBA-15 indicates in contrast the presence of tetrahedrally coordinated Mo centres in the Mo_xO_y species. On the one hand the observed decreased of amplitude at higher Mo-Mo shells in the FT(χ(k)·k^3) of the dehydrated state indicates an increased dispersion of the molybdenum oxide species on the support. This is probably accompanied by an increased disorder and therefore also a broader distance distribution in molybdenum oxide species. On the other hand, the presence of tetrahedral MoO_4 units and a decreased average distances in the distance distribution contribute to the increased amplitude in the first Mo-O shell. Furthermore, a XANES simulation with a tetrahedral (Na_2MoO_4) and a octahedral (α-MoO_3) reference substance was attempted by assuming that a phase mixture of molybdenum oxides is present on the SBA-15 support. The result of the refinement with the sum of the XANES spectra of the references to that of dehydrated Mo_xO_y-SBA-15 is depicted in Figure 6.25. A very good agreement is observed in the pre-edge region, whereas the post-edge region, which is almost featureless, is not matched as good. It is not surprising that the long-range ordered references are less suited to simulate the XANES of the dispersed and disordered SBA-15 supported dehydrated molybdenum oxide species. Despite this it is possible to quantify the contribution of tetrahedral MoO_4 units and distorted octahedral MoO_6 units by the pre-edge peak height. The ratio found by fitting is 3 : 1 for the tetrahedral to the distorted octahedral units.

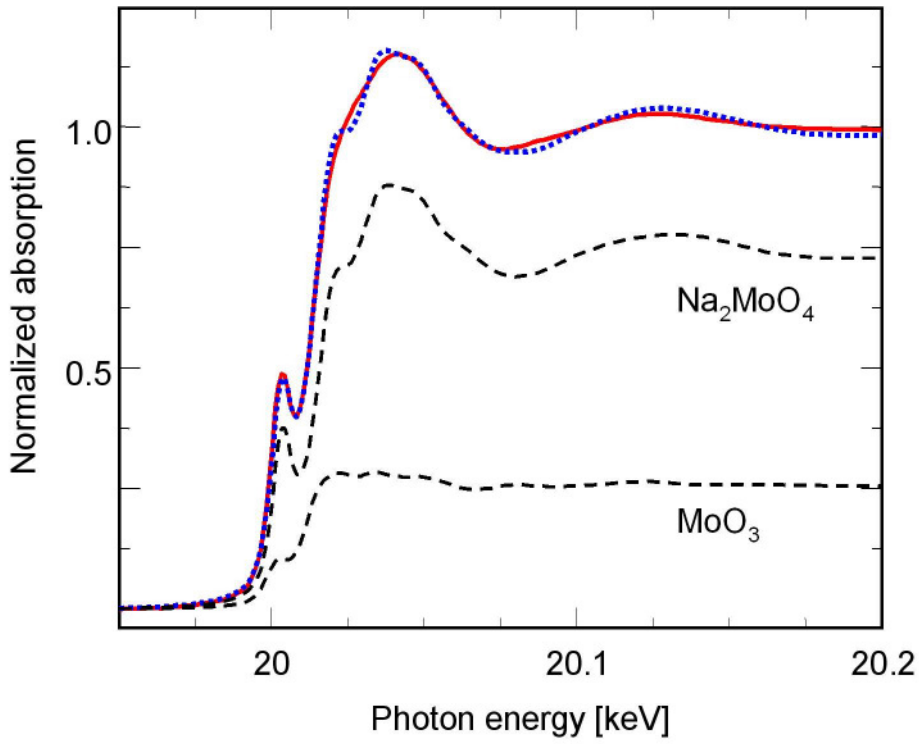

Fig. 6.25: Refinement of sum [dotted] of XANES spectra of references MoO_3 and Na_2MoO_4 [dashed] to Mo K edge XANES spectrum of dehydrated Mo_xO_y/SBA-15 with 5.5 Mo wt.% (0.6 Mo/nm^2) [solid].

Finally, the local structure around the Mo centres of Mo_xO_y/SBA-15 (5.5 wt.% Mo) in the dehydrated state was determined by a detailed EXAFS analysis. During the search to find a suitable model system, it became obvious that for the simulation of the experimental FT(χ(k)·k^3) of dehydrated Mo_xO_y/SBA-15 by one or two Mo-Mo distances was insufficient. Even though the amplitude at higher shells (see Fig. 6.26) was reduced, three Mo-Mo distances were required to describe the particular amplitude shape and imaginary part of the FT(χ(k)·k^3) from 2.5 to 3.5 Å. Hence, for EXAFS refinement amplitudes and theoretical phases calculated for three Mo-Mo distances and different Mo-O distances in hexagonal MoO_3 as reference were used. In Figure 6.24 theoretical and experimental Mo K edge FT(χ(k)·k^3) of dehydrated Mo_xO_y/SBA-15 are depicted. Table 6.7 shows structure parameters being derived from the XAFS refinement.

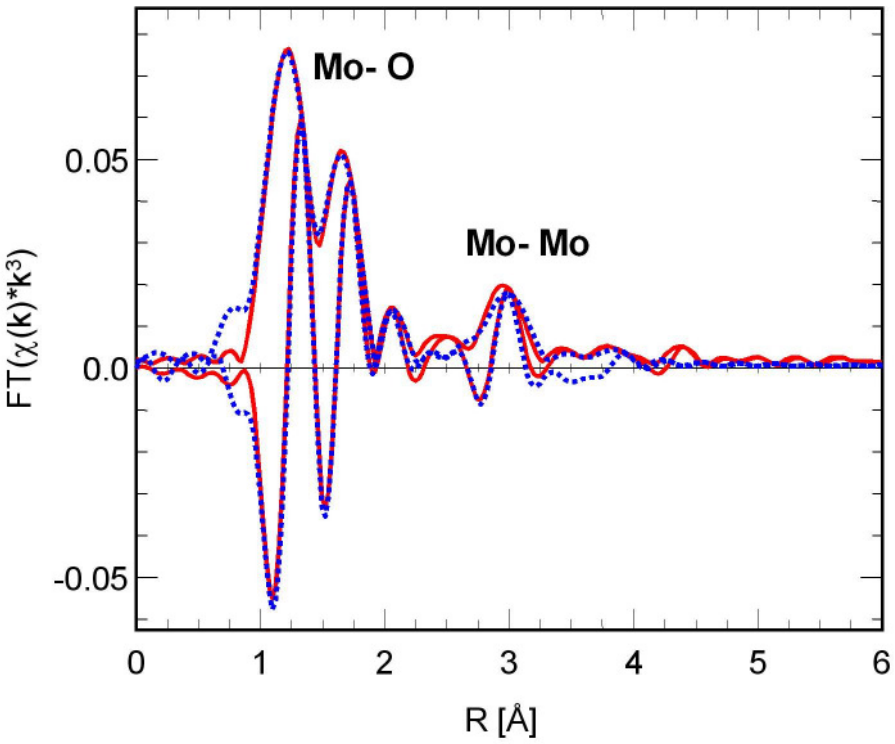

Fig. 6.26: Theoretical and experimental Mo K edge FT(χ(k)*k^3) of dehydrated Mo_xO_y/SBA-15 with 5.5 Mo wt.% (0.6 Mo/nm^2). Mo-O and Mo-Mo distances are indicated.

A sufficient simulation of the first Mo-O shell is reached by using four Mo-O distances. In contrast to the reference hexagonal MoO_3, an increased contribution of Mo-O distances at ~1.67 Å was observed. The origin of the contribution are tetrahedral Mo_xO_y species in addition to the distorted octahedral MoO_6 units of polymeric Mo_xO_y species on the SBA-15 support, which confirms the interpretation of the increased Mo K pre-edge peak in the XANES spectrum of dehydrated Mo_xO_y/SBA-15 (see Fig. 6.21). At higher shells, the reduced amplitude of the FT(χ(k)·k^3) indicates a higher disorder or small extension of the SBA-15 supported Mo_xO_y species. Nonetheless, the used fitting procedure did not allow an independent variation of coordination numbers (N) and σ^2 parameters. As a result, no reliable distinction of static disorder, particle size effects and

Table 6.7: Type, number (N), and XAFS disorder parameters (σ^2) of atoms at distance R from the Mo atoms in Mo_xO_y species in dehydrated Mo_xO_y/SBA-15. Experimental parameters were obtained from a refinement of a hexagonal MoO_3 model structure to the experimental Mo K edge XAFS $\chi(k)$ of dehydrated Mo_xO_y/SBA-15 (Fig. 6.24) (k range from 3.6 to 14.4 $Å^{-1}$, R range from 0.9 to 4.0 Å, E_0 = 8.0 eV, residual ~ 10.6, N_{ind} = 23, N_{free} = 13). Confidence limits in distances and σ^2 parameters are indicated. Subscript C indicates parameters that were correlated in the refinement.

Type	N	R [Å]	σ^2 [$Å^2$]
Mo-O	2	1.67 ± 0.002	0.0010 ± 0.0001
Mo-O	2	1.87 ± 0.005	0.0029 ± 0.0002
Mo-O	1	2.25 ± 0.016	0.0029_C
Mo-O	1	2.41 ± 0.002	0.0025 ± 0.0009
Mo-Mo	2	3.52 ± 0.012	0.0060 ± 0.001
Mo-Mo	2	3.67 ± 0.014	0.0060_C
Mo-Mo	2	3.82 ± 0.019	0.0101 ± 0.002

morphology can be reached. Nevertheless, at different distances the number of nearest Mo neighbours is correctly determined and can be interpreted. Apparently, under reaction conditions at elevated temperatures, the present dehydrated Mo_xO_y phase can be described as a mixture of tetrahedrally and octahedrally coordinated MoO_4 and MoO_6 units. Additionally, it may be assumed, that the present octahedral MoO_6 units are connected in a similar manner like the α-MoO_3 building blocks. Tetrahedral MoO_4 units are connected to other MoO_x units, which does not exclude the presence of isolated MoO_4 units on the support.

6.6.3. Conclusions

Two silica SBA-15 supported highly dispersed molybdenum oxide samples with a loading of 1.0 and 5.5 Mo wt.% (0.2 and 0.6 Mo/nm^2) have been examined by XAS in

their hydrated (as is) and their dehydrated state after thermal treatment at elevated temperatures (>300°C) in O_2 and He (20:80). The results show that the surface molybdenum oxide structures created at low loadings do not depend on the preparation procedure. The XAS results reveal that the hydrated state has similarities with structure motifs of bulk α- or hexagonal MoO_3. The dehydrated state is found to consist of a mixture of monomeric and connected molybdenum oxide centres. While the presence of crystalline MoO_3 can be excluded by Raman spectroscopy (chapter 6.1), tetrahedrally and octahedrally coordinated MoO_4 and MoO_6 units are identified by XAS. The MoO_6 units possess a connectivity similar to that of MoO_3 building blocks, whereas the MoO_4 units are isolated or connected to other Mo_xO_y units.

An important outcome of this study is that the structure of silica SBA-15 supported molybdenum oxide both in its dehydrated state consists of di- or oligomeric molybdenum oxide centres as well as isolated centres.

6.7. Structure of Silica Supported Molybdenum Oxide Studied by O K-Edge NEXAFS

6.7.1. Introduction

The analysis of the O K edge NEXAFS is another possibility to obtain information about the connectivity of the molybdenum oxide centres. On the basis of reference compounds a detailed interpretation of the O K edge NEXAFS spectra is usually due to their complexity not possible. To understand the each contributions of different bonded oxygen species of NEXAFS spectrum theoretical calculations on DFT level are necessary.

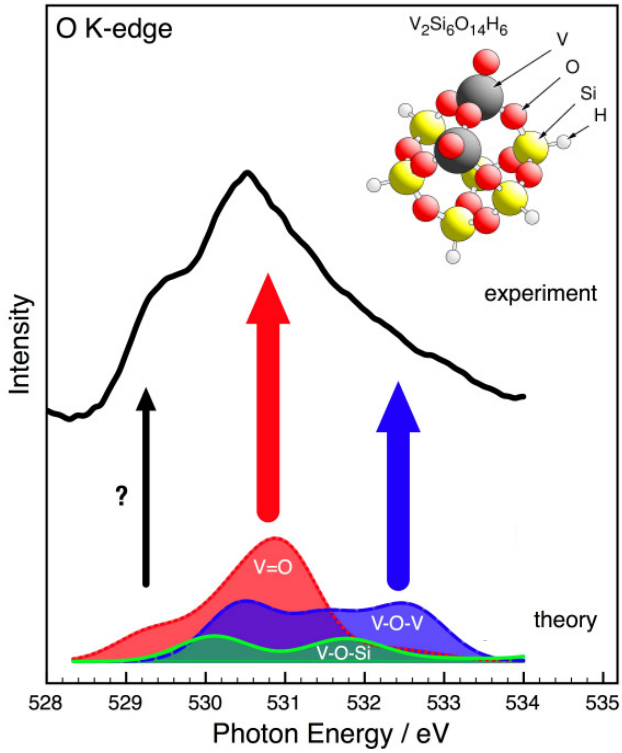

Fig. 6.27: Comparison of theoretical data with contributions of different vanadia structures (V=O, V-O-V, V-O-Si) and experimental data of the O K-edge NEXAFS of 8.0 wt.% V_xO_y/SBA-15. [46]

Recently, this technique has already been successfully employed by Cavalleri and Hävecker to understand important details of silica supported vanadia at low V densities (≤1.0 V/nm^2). [45,46] They found that the vanadia oxygen resonances are well separated from the silica support oxygen resonances and the V $L_{2,3}$ edge. Based on theorical DFT calculations it is described that the contributions of oxygen containing vanadia structures (V=O, V-O-V, V-O-Si) have maxima at different photon energies in the O K edge (see Fig. 6.27). Furthermore, a region in the vanadia resonance was identified which is dominated by the contribution of the V-O-V structure. By comparison of the theoretical and experimental data it was concluded that connected vanadia centres are present on the silica support at low V densities (≤1.0 V/nm^2). Additionally, no change of the shape of the O K edge NEXAFS with increasing V loading from 2.7 to 10.8 Mo wt.% was observed, which indicates that the present distribution of dispersed vanadia species is not influenced by the loading. [46]

6.7.2. Results and Discussion

Figure 6.28 shows a comparison of the O K-edge NEXAFS of 11.1 Mo wt.% Mo_xO_y/SBA-15 and oxa-SBA-15 in the hydrated state at room temperature and in the dehydrated state at 350°C in 0.5 mbar O_2. As can be seen the Mo 4d - O 2p orbital interaction (530-536 eV) and the oxygen of the silica support (>534 eV) are showing almost no overlap. In the hydrated state the Mo-O region (530-536 eV) is characterized by a peak at 530.4 eV and a second unresolved peak at higher energy. Dehydration causes a change of the Mo-O region (530-536 eV) and a doublet-like structure becomes visible for the supported Mo_xO_y species. The peak at 530.4 shifts slightly to 530.2 eV and a new peak at 532.5 eV is observed. The shape and intensity of the shoulder observed in the spectrum of the silica SBA-15 support shows a small variation of the absorption onset at approximately 535 eV.

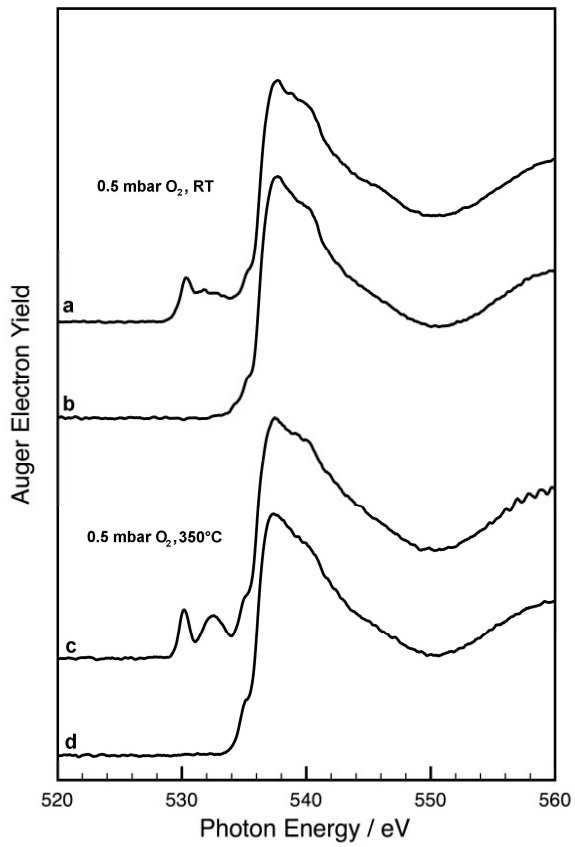

Fig. 6.28: Comparison of the O K-edge NEXAFS spectra of Mo_xO_y/SBA-15 at room temperature in the hydrated state (a) 11.1 wt.% Mo (2.4 Mo/nm^2), (b) oxa-SBA-15 and at 350°C in the dehydrated state (c) 11.1 wt.% Mo (2.4 Mo/nm^2), (d) oxa-SBA-15.

Figure 6.29 displays the O K-edge NEXAFS spectra of silica supported molybdenum oxide with Mo densities of 0.8 and 2.4 Mo/nm^2 at 350°C in 0.5 mbar O_2 showing similar features. Furthermore, NEXAFS spectra of α-MoO_3, hexagonal MoO_3 and $Na_2MoO_4 \cdot 2H_2O$ as reference compounds are shown. The purity of the references was verified by XRD and Raman spectroscopy. The distinct differences of the reference compounds spectra most likely reflects the different local geometric structure. The observed doublet like structure can be explained within a simple orbital hybridization picture of the Mo 4d and the O 2p orbital by transitions between the O 1s to the unoccupied Mo 4d orbitals (t_{2g}, e_g for octahedral or e, t_g for tetrahedral ligand field

splitting). [164] The intensity reflects the number of unoccupied states in these orbitals, while the energy difference between the two peaks is a measure of the crystal field splitting, which is influenced by the local geometry. Therefore, a small value of the crystal field splitting (e.g. 2 eV) is maybe associated with a tetrahedral arrangement and a larger value with a (distorted) octahedral structure (e.g. 3.5 eV).

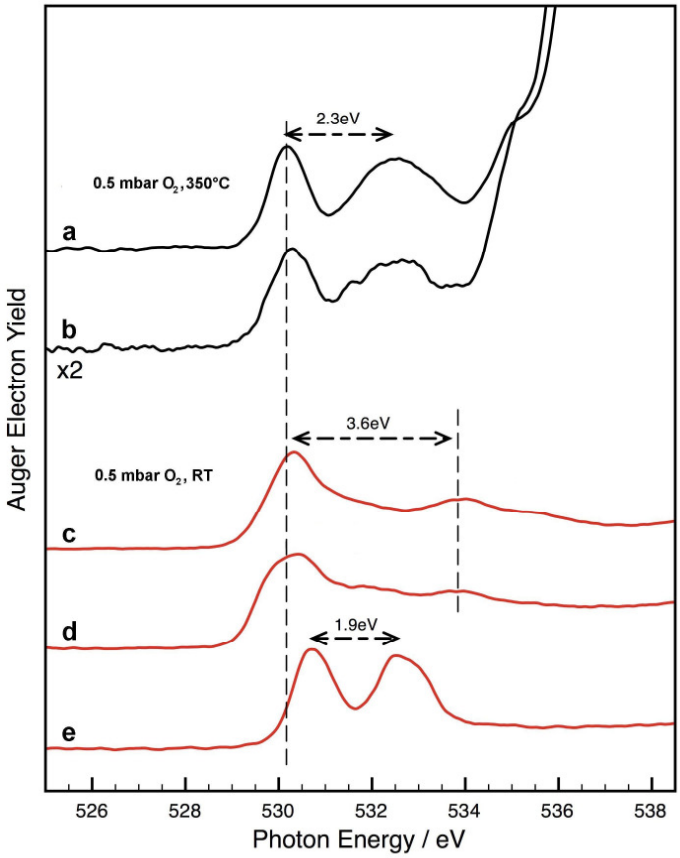

Fig. 6.29: O K-edge NEXAFS spectra of Mo_xO_y/SBA-15 at 350°C in the dehydrated state (a) 11.1 wt.% Mo (2.4 Mo/nm^2), (b) 5.9 wt.% Mo (0.8 Mo/nm^2) and at room temperature with reference compounds (c) α-MoO_3, (d) hexagonal MoO_3 and (e) $Na_2MoO_4 \cdot 2H_2O$.

The present structures on the silica supported molybdenum oxide catalyst are different from bulk α- and hexagonal MoO_3, although it is not possible to exclude the presence of small amounts of MoO_3-like structures on the support due to the overlap of the MoO_3 peak at approximately 530.3 eV with the feature at 530.2 eV of the supported catalyst.

The doublet-like peak structure of the supported molybdenum oxide shows more similarities with the sodium molybdate reference ($Na_2MoO_4 \cdot 2H_2O$) which might be an indication for a more tetrahedral arrangement or a reduced number of coordinated oxygen to the molybdenum.

To obtain a more detailed understanding of the present O K-edge NEXAFS features and to answer the question, which kind of molybdenum oxide centre geometries are present on the support and whether those centres are connected more sophisticated DFT calculations are necessary. [165] In that way the different contribution of molybdyl oxygen (Mo=O) and bridging oxygen (Mo-O-Mo, Si-O-Mo) can be separated and maybe spectral regions identified, which are dominated by the contribution of bridging oxygen between two molybdenum oxide centres (Mo-O-Mo). Based on the input of possible structures for Mo_xO_y by Raman-, UV/Vis-, IR- and X-Ray Absorption Spectroscopy the NEXAFS spectra of a number of reference structures should be calculated. Those structures should comprise the structure motif of tetrahedral and octahedral molybdenum oxide centres, which are present as monomers and dimers. Furthermore, dimers with a connection of tetrahedral and octahedral molybdenum oxide centres should also be considered.

A good starting point for calculation of the monomeric and dimeric tetrahedral species are the structures being used for the analogous vanadia system by Cavalleri et al.. [45,46] The modelling of the silica supported octahedral species is slightly more challenging as no crystal structure of a free molybdenum (i.e. not ligand stabilized) molybdenum oxide octahedral exists in nature. Therefore, it is difficult to create a realistic silica surface sight to stabilize it. Some of the obstacles can be overcome by reference substances. The Keggin structure of silico molybdic acid ($H_4[SiMo_{12}O_{40}]$) for instance comprises octahedral connected molybdenum oxide centres and a Si-O-Mo structure with Si-O and O-Mo bond lengths, which can also be found in α-quartz and α-MoO_3, respectively. Furthermore, the NEXAFS spectra of $Na_2Mo_2O_7$ should be calculated as the crystal structure exhibits connections between tetra- and octahedral

centres. Additionally, the calculation of the spectra of α-MoO_3 or hexagonal MoO_3 should also be useful as they comprise edge and corner shared connected octahedrals.

6.7.3. Conclusions

The resonances of molybdenum oxide and silica support at resonances of the O K edge are well resolved and separated. Unfortunately it is not possible to have a reliable conclusion on to the present molybdenum oxide structures on the basis of bulk reference compounds. Therefore sophisticated DFT calculations on model structures are necessary to separate the contributions molybdyl (Mo=O), bridging (Mo-O-Mo) and interface (Mo-O-Si) oxygen. With these results it is may be possible to determine an energy region in the spectra which can be assigned to Mo-O-Mo and is relatively undisturbed by other contributions.

6.8. *In situ* Raman Spectroscopy during Propylene Oxidation and in the Presence of Steam

6.8.1. Introduction

In this chapter, the Mo_xO_y/SBA-15 catalyst is examined for its structural dynamics under *in situ* conditions to determine, whether the molybdenum oxide structure at elevated temperatures has similarities with the structures of the hydrated or dehydrated state at room temperature. (chapter 6.2) The knowledge of the catalyst structure under *in situ* conditions can reveal valuable information about the active sites. Therefore, the catalyst was treated in a home made *in situ* Raman-MS setup (chapter 2.2.) in synthetic air, under propylene oxidation conditions, and in the presence of steam. In parallel, the *in situ* Raman-MS setup allowed the monitoring of catalytic activity.

6.8.2. *In situ* Examination of Mo_xO_y/SBA-15

Under *in situ* conditions, the structure of Mo_xO_y/SBA-15 catalysts was examined in dependence of temperature and the in the presence of steam and propylene in the feed gas mixture. Mo_xO_y/SBA-15 catalysts with loadings of 5.9, 10.1 and 19.9 wt.% Mo (0.8, 2.0, 7.6 Mo/nm^2) and an oxa/SBA-15 reference sample without molybdenum oxide were compared. The tests were conducted at a temperature of 500°C and a total flow rate of 90 ml/min (GHSV = 1800 ml·g^{-1}·h^{-1}). The sequence of testing conditions was oxidative ($C_3H_6/O_2/N_2$ = 0/7/93 (**A**)), reactive ($C_3H_6/O_2/N_2$ = 3/7/90 (**B**)) and oxidative ($C_3H_6/O_2/N_2$ = 0/7/93 (**C**)) again. For a better comparison and interpretation of the spectra, a linear background subtraction was performed in the range of 800 to 1150 cm^{-1}

and normalized afterwards. Because of strong fluorescence, the background of the catalyst with 5.9 wt.% Mo was determined by a polynominal fit of sixth order and removed in the same range. The accumulation time for the spectra was 30 min unless stated otherwise.

The catalysts with 5.9 and 10.1 wt.% Mo show that the conversion of propylene does not lead to a substantial change of the molybdenum oxide structure, which can be detected with Raman spectroscopy (Fig. 6.30 and 6.32).

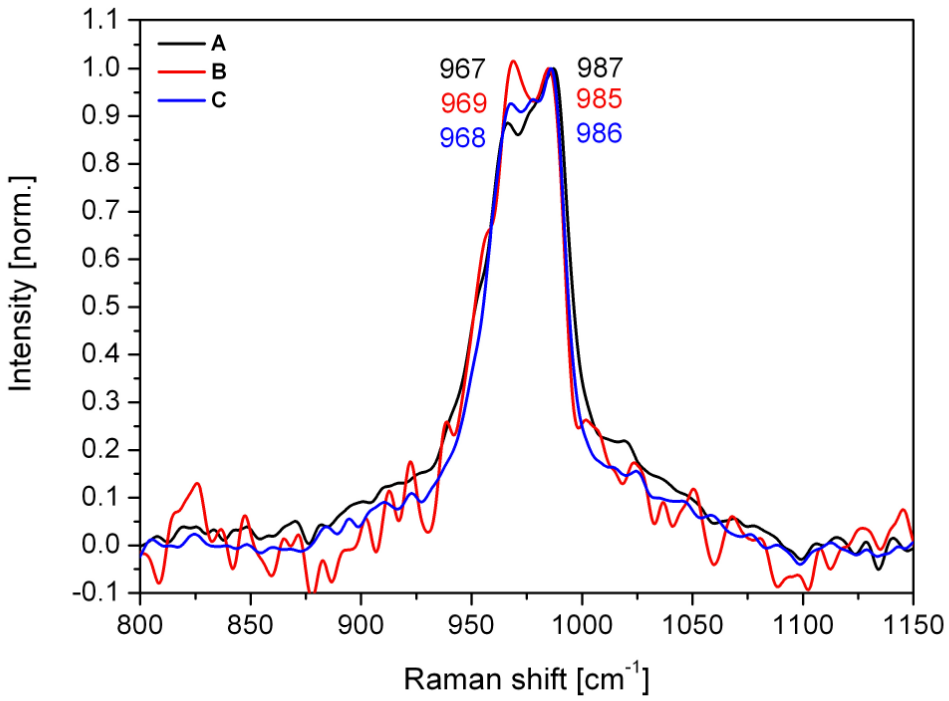

Fig. 6.30: *In situ* Raman spectra of Mo_xO_y/SBA-15 (5.9 wt.% Mo, 0.8 Mo/nm^2) at 500°C in (**A**) $C_3H_6/O_2/N_2$ = 0/7/93, (**B**) $C_3H_6/O_2/N_2$ = 3/7/90, (**C**) $C_3H_6/O_2/N_2$ = 0/7/93 and 90 ml/min total. The spectra have been normalized with respect to the Peak at 986 cm^{-1}.

The position of the molybdyl bands is basically comparable to the band positions in the spectra of dehydrated molybdenum oxide measured a room temperature (chapter 6.2.). A more detailed view of Mo_xO_y/SBA-15 with 5.9 wt.% Mo shows that the molybdyl band exhibits the same band shape, but is red shifted by 6 cm^{-1} in comparison to the room temperature spectra. Furthermore the stretching vibrations of the hydroxyl groups

at 3740 cm^{-1} were detected. (not shown) A distinction of the Si-OH and Mo-OH contribution was not possible. Ohler and coworkers observed also during methane oxidation on silica supported molybdenum oxide (0.44 Mo/nm^2) that the spectra do not change while switch between reaction conditions and synthetic air. [32] A similar result has been reported by Banares who also performed methane oxidation on silica supported molybdenum oxide. [6]

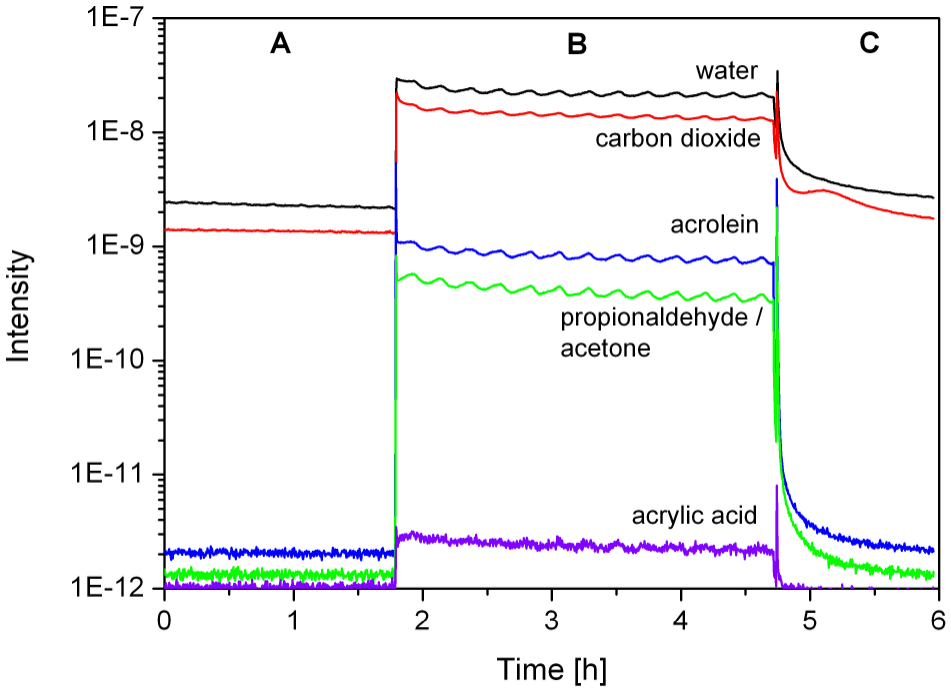

Fig. 6.31: Mass traces of the reaction products during propylene oxidation on Mo_xO_y/SBA-15 (5.9 wt.% Mo, 0.8 Mo/nm^2) at 500°C in (**A**) $C_3H_6/O_2/N_2$ = 0/7/93, (**B**) $C_3H_6/O_2/N_2$ = 3/7/90, (**C**) $C_3H_6/O_2/N_2$ = 0/7/93 and 90 ml/min total flow.

A tracing of the reaction products by mass spectrometry during the spectroscopic analysis shows that propylene is converted at 500°C. The reaction conditions were chosen to be similar to the ones used in the catalytic test in the reactor described in chapter 5 (T: 500°C, GHSV: 2000 $ml \cdot h^{-1} \cdot g^{-1}$, $C_3H_6/O_2/N_2$ = 3/7/90). Hence, the conversion in the Raman cell was calculated to be 13 % with approximately the same

selectivity as shown in Tab. 5.1. Typical reaction products like CO_2, acetone/propionaldehyde, acrolein, acidic acid, acrylic acid, and propionic acid have been found like in the catalytic test in the reactor. Within the first hour under propylene oxidation conditions the mass traces of the products decreased by 25% and remained afterwards at a constant level. The reduction of the conversion had no effect on the Raman spectra recorded under reaction conditions.

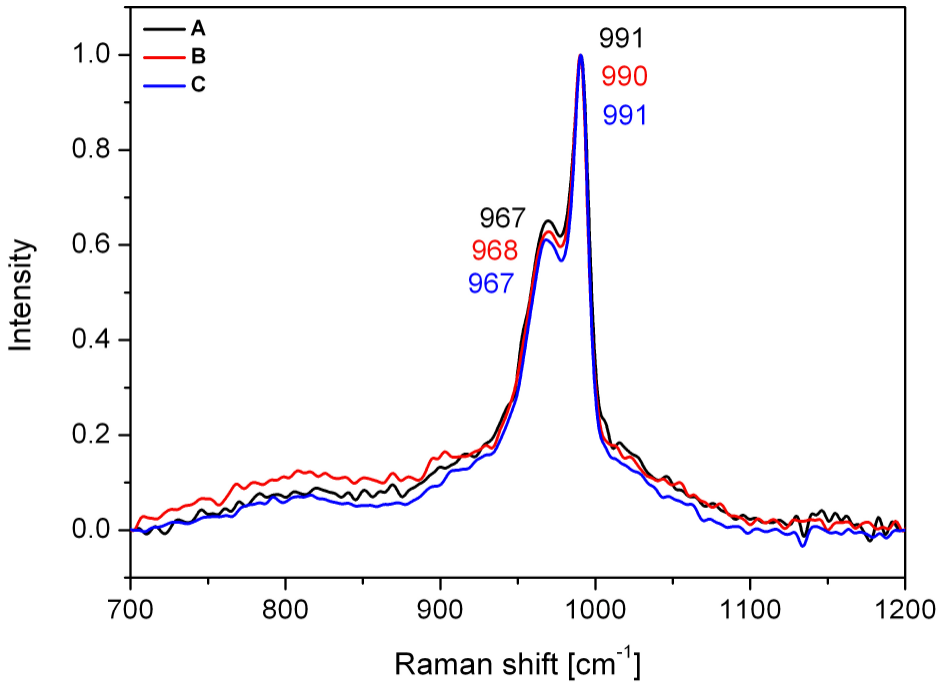

Fig. 6.32: *In situ* Raman spectra of Mo_xO_y/SBA-15 (10.1 wt.% Mo, 2.0 Mo/nm^2) at 500°C in (**A**) $C_3H_6/O_2/N_2$ = 0/7/93, (**B**) $C_3H_6/O_2/N_2$ = 3/7/90, (**C**) $C_3H_6/O_2/N_2$ = 0/7/93 and 90 ml/min total flow. The spectra have been normalized with respect to the peak at 990 cm^{-1}.

The Mo_xO_y/SBA-15 with 10.1 wt.% Mo loading in contrast to the one with 5.9 wt.% Mo does not show a shift of the molybdyl band as compared to the spectra at room temperature. However, a change of the ratio of the two molybdyl bands at 970 cm^{-1} to the one at 990 cm^{-1} compared to those at room temperature is observed, which indicates

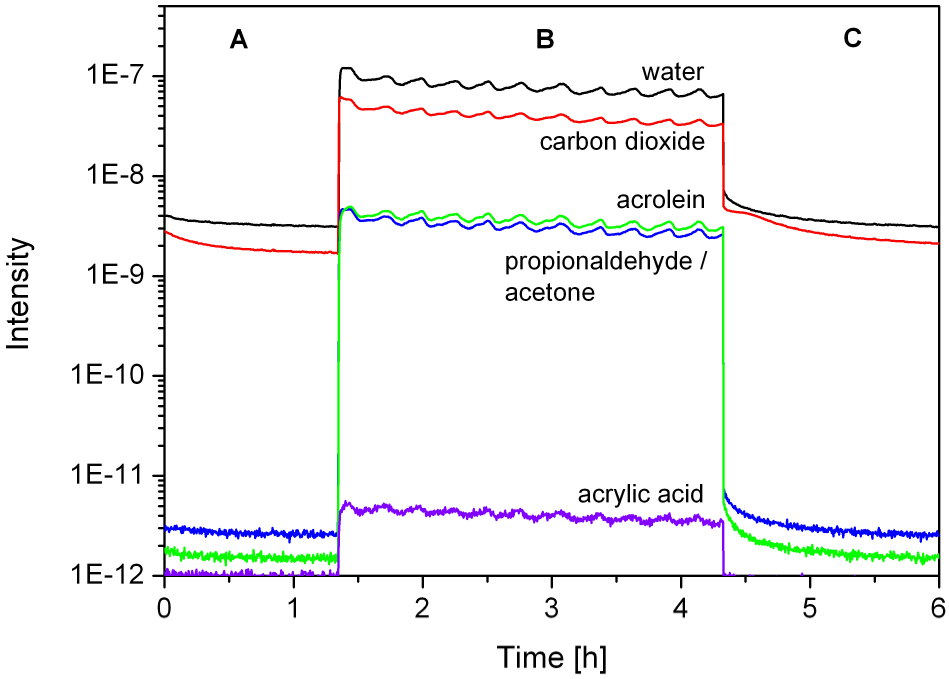

Fig. 6.33: Mass traces of the reaction products during propylene oxidation on Mo_xO_y/SBA-15 (10.1 wt.% Mo, 2.0 Mo/nm^2) at 500°C in (**A**) $C_3H_6/O_2/N_2$ = 0/7/93, (**B**) $C_3H_6/O_2/N_2$ = 3/7/90, (**C**) $C_3H_6/O_2/N_2$ = 0/7/93 and 90 ml/min total flow.

a change of the surface species ratio. Those species may be for instance monomeric tetrahedral and square pyramidal species, like discussed by Gregorianes and coworkers. [132] Wachs et al. also studied the structure of silica supported molybdenum oxide with a Mo density of 1.5 Mo/nm^2 in air at room temperature and 550°C, but a comparison of the spectra does not show a change of the molybdyl band ratio as observed for sample (**2**). [29] On the catalytic side, an increase of the propylene conversion to approximately 30 % is observed.

The *in situ* Raman spectra of Mo_xO_y/SBA-15 with 19.9 wt.% Mo are dominated by crystalline α-MoO_3, as can be seen by the presence of the characteristic bands at 995, 819, and 666 cm^{-1}. Besides, the sample contains also dispersed dehydrated molybdenum

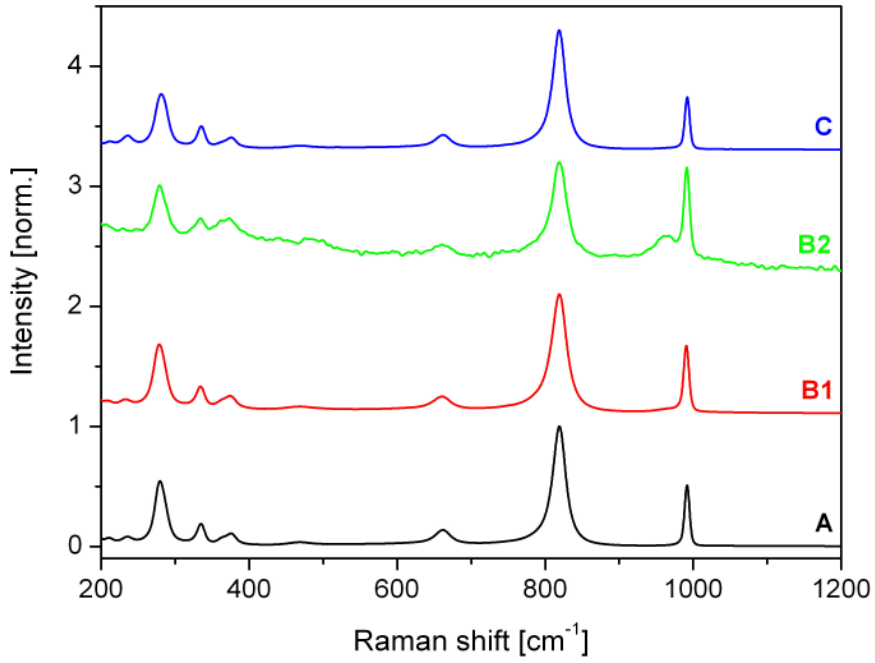

Fig. 6.34: *In situ* Raman spectra of Mo_xO_y/SBA-15 (19.9 wt.% Mo, 7.6 Mo/nm^2) at 500°C in (**A**) $C_3H_6/O_2/N_2$ = 0/7/93, (**B1/2**) $C_3H_6/O_2/N_2$ = 3/7/90, (**C**) $C_3H_6/O_2/N_2$ = 0/7/93 and 90 ml/min total flow. The spectra have been normalized with respect to the peak at 819 cm^{-1} and are offset by 1.1 (B1) 2.2 (B2) and 3.,3 (C) for clarity.

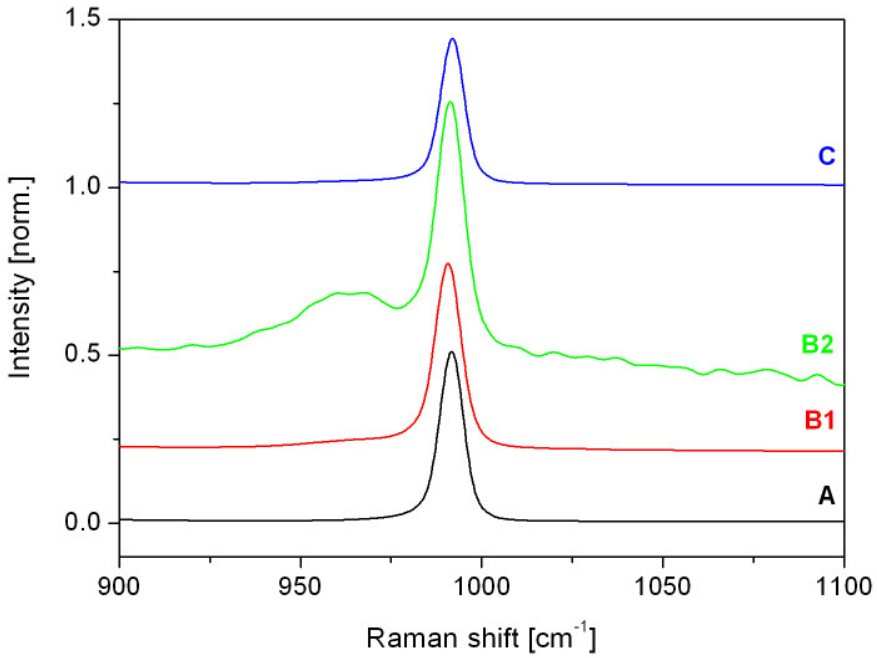

Fig. 6.35: Detailed view of the *in situ* Raman spectra shown in Fig. 6.34. The spectra have been normalized with respect to the peak at 819 cm^{-1} and are offset by 0.2 (B1) 0.4 (B2) and 1.0 (C) for clarity.

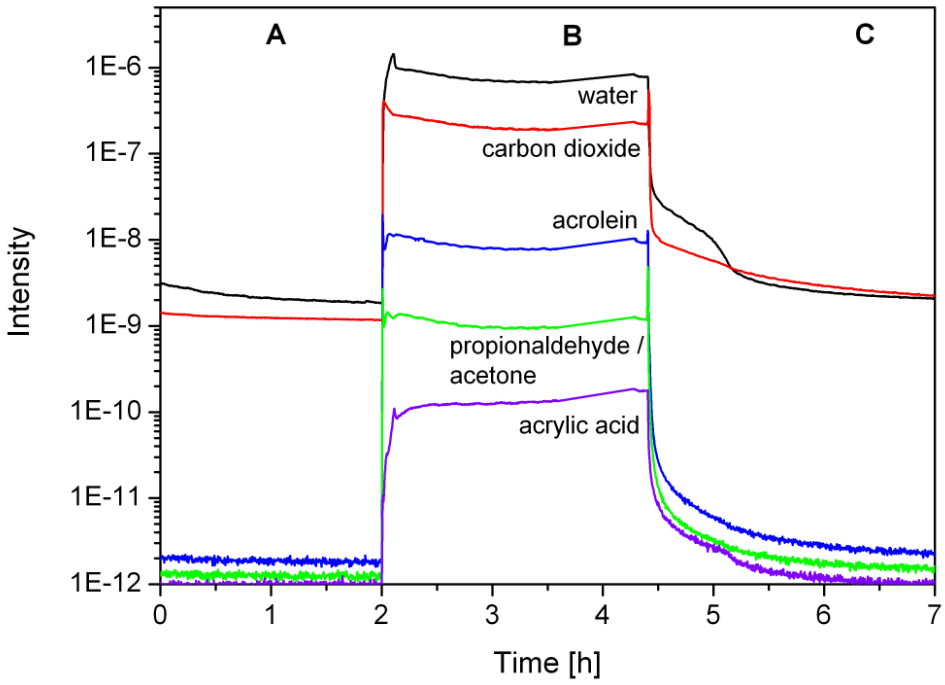

Fig. 6.36: Mass traces of the reaction products during propylene oxidation on Mo_xO_y/SBA-15 (19.9 wt.% Mo, 7.6 Mo/nm^2) at 500°C in (**A**) $C_3H_6/O_2/N_2$ = 0/7/93, (**B**) $C_3H_6/O_2/N_2$ = 3/7/90, (**C**) $C_3H_6/O_2/N_2$ = 0/7/93 and 90 ml/min total flow.

oxide, which can be identified by the shoulder next to the α-MoO_3 molybdyl vibration at 960 to 980 cm^{-1}. The fraction of α-MoO_3 is approximately 8 wt.% Mo as discussed in chapter 4.4. Hence, the different intensity of both bands can be attributed to the largely different cross sections of dispersed and crystalline molybdenum oxide.

Under reaction conditions a decrease of the α-MoO_3-bands can be observed, which is distributed inhomogeneously over the catalyst bed and increases with time. This leads to a formation of islands that remain practically unchanged (Fig. 6.34 B1, 6.35 B1) and regions, where the α-MoO_3 bands almost disappeared and those of dispersed molybdenum oxide are detected more pronounced (Fig. 6.34 B2, 6.35 B2). The observation can be interpreted as conversion of crystalline α-MoO_3 into dispersed Mo_xO_y or selective reduction of α-MoO_3 by propylene. On the catalytic side, an increase of the propylene conversion up to 100% is observed. Indications for the

formation of carbon deposits, which have characteristic bands at 1350 and 1580 cm^{-1} were not found. [166] Besides, also no Raman bands of reactants and products for instance C-H vibrations near 3000 cm^{-1} or C=O vibrations around 1700 cm^{-1} have been detected during propylene oxidation on all three catalysts.

6.8.3 The Influence of Steam

As already discussed in chapter 6.8.2., the conversion of propylene ($C_3H_6/O_2/N_2$ = 3/7/90 (**B**)) at 500°C on samples containing only disperse molybdenum oxide has almost no effect on the structure observed by Raman spectroscopy as compared to the one observed in synthetic air ($C_3H_6/O_2/N_2$ = 0/7/93 (**A**)). As steam is frequently used in catalysed oxidation reactions in industrial scale to improve the yield of the oxygenates, its influence on the structure of Mo_xO_y/SBA-15 has also been studied.

Therefore the following experiment was conducted. At first, an initial spectrum of the catalyst (10.1 wt.% Mo) without the presence of steam ($C_3H_6/O_2/N_2/H_2O$ = 0/10/90/0 (**D**)) was recorded. Afterwards the catalyst was exposed to a steam containing atmosphere ($C_3H_6/O_2/N_2/H_2O$ = 0/10/45/45 (**E**)) for 4.5 h. While doing so, a decrease of the relative intensity of the band at 991 cm^{-1} compared to the band at 969 cm^{-1} was observed. Additionally, the band is shifts from 991 to 983 cm^{-1}. For the reapplication of non steam conditions (**D**), for 2 h no regeneration of the band at 983 cm^{-1} that means an increase in intensity or a shift of the band, was observed. The final treatment of the catalyst with steam and propylene ($C_3H_6/O_2/N_2/H_2O$ = 3/7/45/45 (**F**)) for 2 h (total time stream: 9.4 h) also did not led to a further change of the structure.

The bands observed at 969 and 983-991 cm^{-1} can be assigned to two different molybdenum species, as discussed in chapter 6.2.. [132] Therefore, the changing intensity ratio of the two bands in the presence of steam can be explained by a ratio change of these species, as assuming that the sections of the Raman signals are constant

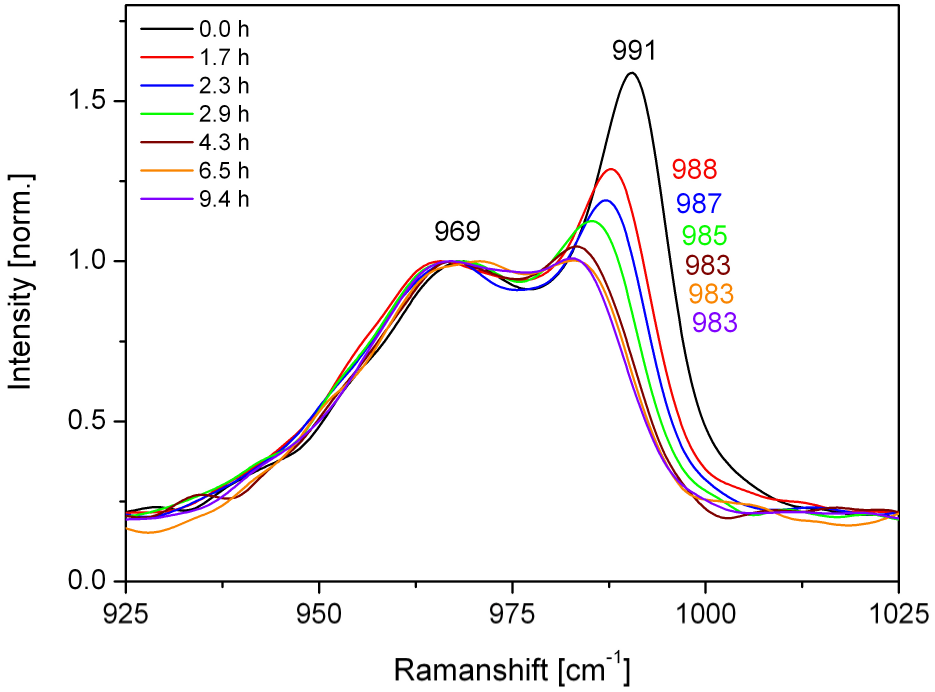

Fig. 6.37: *In situ* Raman spectra of Mo_xO_y/SBA-15 (10.1 wt.% Mo, 2.0 Mo/nm^2) at 500°C in (**D**) $C_3H_6/O_2/N_2/H_2O$ = 0/10/90/0, (**E**) $C_3H_6/O_2/N_2/H_2O$ = 0/10/45/45, (**F**) $C_3H_6/O_2/N_2/H_2O$ = 3/7/45/45 and 90 ml/min total flow. The spectra have been normalized with respect to the peak at 969 cm^{-1}. For a detailed description see text.

under steam conditions. Another possible explanation is that parts of the Mo_xO_y structure changed. A larger distortion or disorder of the structure may have occurred, which can also influence the Raman cross section and the band position. If a distortion of the structure is assumed, the observed red shift of the band at 991 by 9 cm^{-1} corresponds to a change of the molybdyl bond length of 0.04 pm according to the model of Hardcastle and coworkers. [167] Interestingly, this process seems to be irreversible. Furthermore, it can be excluded that the change of the relative intensity of the bands at 970 and 990 cm^{-1} is due to the Si-OH mode at 970 cm^{-1}, as its contribution to the total band is at higher Mo loadings relatively low. (see chapter 6.2.)

For a similar examination of a Mo_xO_y/SBA-15 with a lower Mo loading (5.9 wt.% Mo) almost no effect has been found. The band at 987 cm^{-1} shifts to 981 cm^{-1} and a small gain of intensity is detected after switching from non steam (**D**) to steam conditions (**E**).

Again no reversibility as for the catalyst with 10.1 wt.% Mo loading has been observed.

Studies on the influence of steam onto silica supported disperse molybdenum oxide have also been conducted by Banares et al. Therefore, a Cabosil supported sample with a Mo density of 0.6 Mo/nm^2 was used and treated with water saturated air at 500°C and measured at a laser wavelength of 514 nm. [41,168] The observed molybdyl band had a maximum at approximately 980 cm^{-1} and a shoulder at 960 cm^{-1}. The spectrum has been described as identical to a spectrum of a sample dehydratized in synthetic air. [29,131]

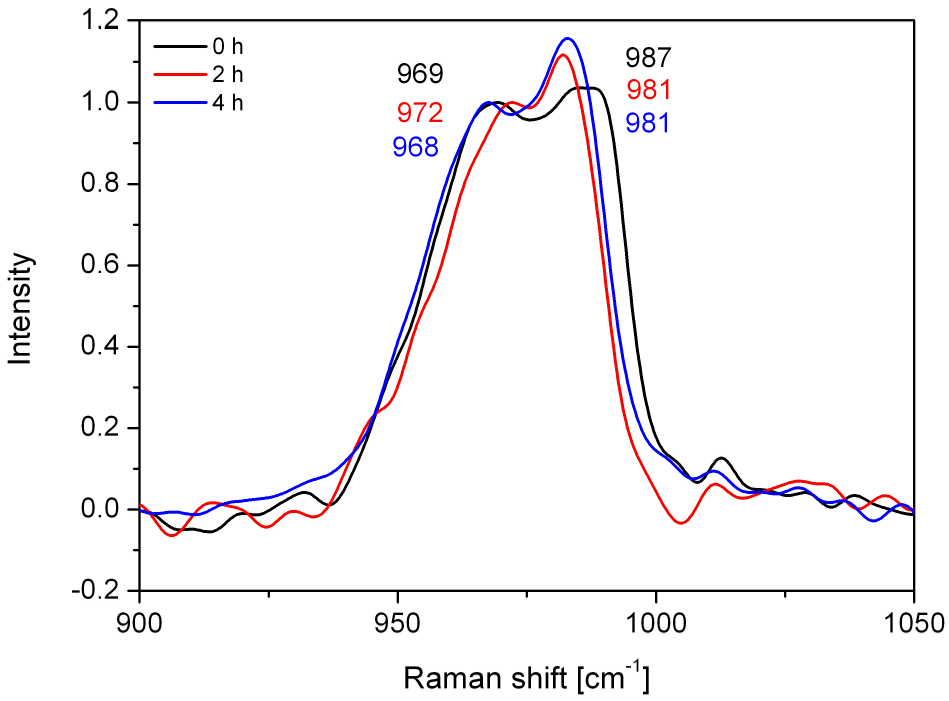

Fig. 6.37: *In situ* Raman spectra of Mo_xO_y/SBA-15 (5.9 wt.% Mo, 0.8 Mo/nm^2) at 500°C with (**D**) $C_3H_6/O_2/N_2/H_2O$ = 0/10/90/0; (**E**) $C_3H_6/O_2/N_2/H_2O$ = 0/10/45/45 after 2 h and (**D**) $C_3H_6/O_2/N_2/H_2O$ = 0/10/45/45 after 4 h at 90 ml/min total flow. The spectra have been normalized to the peak at 969 cm^{-1}.

Furthermore, Wachs et al. also conducted experiments at a laser wavelength of 325 nm with samples of a Mo density of 0.6 and 1.5 Mo/nm^2 in water saturated air (2 %) at 500°C. [126] The spectra of these samples seem to be similar to the dehydrated state at

500°C in dry air [42], which can be interpreted that way that at low steam concentration a shift of the band ratio and the position of the band at higher wavelength is not induced. Additionally, in that study isotopic labelling experiments with $H_2{}^{16}O$ and $H_2{}^{18}O$ were performed. The oxygen isotope exchange led to a shift of 50 cm^{-1} for the molybdyl bands of the sample with 1.5 Mo/nm^2 Mo density from 970 and 988 cm^{-1} to 920 and 930 cm^{-1}. A similar shift of 48 cm^{-1} has been observed for the sample with 0.6 Mo/nm^2 density, too. [126] The observed similar shift of both bands combined with results from theory [31] was interpreted by Wachs et al. as proof that both bands can be assigned to the symmetrical (988 cm^{-1}) and antisymmetrical (970 cm^{-1}) stretching mode of isolated molybdenum oxide centres in tetrahedral coordination. This interpretation is not in agreement with the steam induced shift and change of intensity ratio discussed above. Furthermore, the presence of isolated species also contradicts with the results from UV/Vis (chapter 6.3.), XAS (chapter 6.5.) and IR (chapter 6.4.) spectroscopy.

6.8.4. Conclusions

Under *in situ* conditions, the Raman spectra of the Mo_xO_y/SBA-15 system, which contains only dispersed molybdenum oxide, resembles in principal the spectra of the dehydrated state at room temperature. For a loading of 10.1 Mo wt.%, a more intensive band at 991 cm^{-1} was observed at 500°C than for the same sample and conditions at room temperature. The conversion of propylene does not have an influence on to shape and position of the band under *in situ* conditions. In contrast to that, the presence of steam in the feed mixture changes the signal area ratio of the bands at 969 and 991 cm^{-1}. Additionally, a red shift of the band from 991 to 983 cm^{-1} is observed. Both bands can therefore be assigned to different Mo_xO_y species. For samples with a high molybdenum loading containing disperse as well as crystalline molybdenum oxide a conversion of

crystalline MoO_3 into disperse Mo_xO_y or selective reduction under in situ conditions with high conversion of propylene was observed.

As products of the propylene oxidation, CO_2, H_2O, acrolein, acetone/propionaldehyde, acidic acid, acrylic acid, and propionic acid have been observed. Similar conditions like in the previous experiments in the reactor (chapter 5.) have been chosen in the *in situ* Raman cell, so that the propylene conversion for the sample with 5.9 Mo wt.% was about 13 % with comparable selectivities like in the reactor experiment. For all products, an increasing yield with increasing Mo loading was determined qualitatively.

6.9. Summary and Discussion of Results

In this chapter, the results from the different spectroscopic techniques for the structure assignment are summarized and discussed to propose a structural model of the hydrated and dehydrated state of the dispersed SBA-15 supported Mo_xO_y-phase.

6.9.1. The Hydrated State of Mo_xO_y/SBA-15

Dispersed molybdenum oxide species are detected with high sensitivity by Raman spectroscopy up to a loading of 12.1 wt.% Mo (3.5 Mo/nm^2) in the hydrated and dehydrated state. The Raman spectra of the Mo_xO_y/SBA-15 samples in their hydrated state are showing two specific molybdenum oxide bands at 880 (ν(Mo=O)) and 950 cm^{-1} (ν(Mo-O-Mo)). The two bands can be assigned by comparison with molybdenum oxide reference compounds to a structure, which largely resembles that of hepta or octa molybdates (chapter 6.2.). Furthermore, the spectra do not show any band shifts or new bands with increasing loading.

The XP spectroscopy results of hydrated Mo_xO_y/SBA-15 samples with loadings of 5.9 and 21.1 wt.% Mo (0.8 and 9.8 Mo/nm^2), respectively, show that molybdenum oxide is exclusively present in the +VI oxidation state. Additionally, a shift of the binding energies to 233.6 eV of the Mo 3d peak 5/2 has been detected, which is significantly higher than the binding energy found in bulk MoO_3 (232.6 eV) as reference material. The shift can be interpreted in that way that at least the molybdenum oxide is present in a dispersed state on the SBA-15 surface, which are smaller and different from bulk structures of molybdenum

oxide. The broadening of the Mo 3d peaks may indicate that a distribution of molybdenum oxide structure of different size is present on the support. (chapter 6.4.)

This conclusion is also supported by UV/Vis spectroscopy. (chapter 6.3.) The spectra of the samples with a 5.9, 11.1, and 13.9 wt.% Mo loading (0.8, 2.0, and 3.2 Mo/nm^2) show a maximum at 245 nm and an asymmetry towards higher wavelengths with intensities extending up to 370 nm. As discussed in chapter 6.3., no unambiguous assignment to a specific coordination geometry or structure can be made on the basis of the UV-Vis spectra. But by comparison with bulk references it is possible to make certain limitations for the present structures. For example, tetrahedral monomeric reference Na_2MoO_4 shows an absorption maximum at 250 nm and a sharp decrease of intensity up to a wavelength of 280 nm. In contrast, other reference substance like $Na_2Mo_2O_7$ or α-MoO_3, which consist of connected molybdenum oxide centres, possess significant intensity at wavelength well above 300 nm. Therefore, the additional intensity at wavelengths higher than 280 nm can be explained by the presence of other species than isolated monomers. Those species can, for instance, be isolated octahedrals, connected tetrahedral or octahedral molybdenum oxide centres. It is also possible that a mixture of these three species exists on the surface besides tetrahedral monomeric molybdenum oxide centres. Furthermore, the similar shape of the spectra in the loading range, where only dispersed molybdenum oxide is present on the support shows, that the distribution of the present molybdenum oxide species seems to be largely independent of loading.

The structure of Mo_xO_y/SBA-15 samples with loadings of 1.0 and 5.5 wt.% Mo (0.2 and 0.8 Mo/nm^2) has also been studied by Mo K-edge X-Ray absorption spectroscopy (chapter 6.5.). The comparison of XANES region of the spectra with bulk references shows similarities with α-MoO_3, whereas the FT(χ(k)·k^3) corresponds to that of hexagonal MoO_3. Also, a distinct peak in the FT(χ(k)·k^3) at Mo-Mo distances was found, which is a clear indication for the presence of connected molybdenum oxide structures.

The results of Raman spectroscopy and XAS seem to be a bit contradictory, as three different structures are reported by the two techniques. For the interpretation one has to keep in mind, what informations are obtained from the system by those spectroscopic techniques. Raman spectroscopy on the one hand is very sensitive to structural changes, but gives information about specific details of the structure (ν(Mo=O), ν(Mo-O-Mo)), which may then be used for the structural assignment. XAS on the other hand is an averaging technique, which may be blind to minority phases below 5 % and requires careful analysis in case of phase mixtures. That a mixture of molybdenum oxide with different geometry and size is present on the support surface can be deduced from the UV/Vis spectra. Furthermore, the size of molybdenum oxide species should be smaller as verified by the binding energy shift in XPS, which is also supported by the fact that SBA-15 has a specific pore size so that the aggregate size of the molybdenum oxide is limited. Therefore, the α-MoO_3 structure identified by the XANES fingerprint region and the hexagonal MoO_3 structure found by fitting of the EXAFS data only represent structure motifs of the present amorphous, dispersed molybdenum oxide. Further experiments will be needed to obtain a complete picture of the molybdenum oxide structure in the hydrated state.

The important finding of the applied techniques (Raman, UV/Vis and XAS) is that the found structures contain connected molybdenum oxide centres down to low Mo loadings in accordance with the literature. [28] Additionally, the distribution of the structure size of the dispersed molybdenum oxide does not seem to change with the loading as long as no crystalline MoO_3 is present on the support.

6.9.2. The Dehydrated State of Mo_xO_y/SBA-15

In the dehydration process a structural transformation of the molybdenum oxide is observed. For instance in the Raman spectra the Mo-O-Mo band at 880 cm^{-1} disappears and the band Mo=O band at 950 cm^{-1} is shifted to 970 to 990 cm^{-1}. Furthermore, it was observed that the molybdyl band consists of at least two contributions located at 970 cm^{-1} and at around 980 cm^{-1}. The latter band shows a Mo loading dependent shift from 980 to 996 cm^{-1} when increasing the loading from 5.9 to 12.1 wt.% Mo (0.8 to 3.5 Mo/nm^2). In the literature, the two bands are assigned to the symmetric and antisymmetric molybdyl mode of an isolated tetrahedral molybdenum oxide. The assignment was supported by results from EXAFS and theory. [28,30,31] However, a recent theoretical study suggests that the two molybdyl modes should be assigned to tetrahedral and a square pyramidal molybdenum oxide centre, but without considering the possibility of connected molybdenum oxide centres. [132] (see chapter 6.2.)

Under *in situ* conditions at 500°C in synthetic air, the Raman spectra of the Mo_xO_y/SBA-15 system resembles the spectra of the dehydrated state at room temperature. Additionally, under these conditions for the sample with 10.1 Mo wt.% (2.0 Mo/nm^2) loading, a more intensive band at 991 cm^{-1} was observed than at room temperature. The addition of propylene to the feed mixture has no significant influence on shape and position of the band. In contrast the presence of steam (50 vol.%) in the feed mixture influences the ratio of the bands at 969 and 991 cm^{-1}. Furthermore, a red shift of the band at 991 to 983 cm^{-1} with time is observed. Both effects can be seen as an indication that the two bands do not represent the symmetric and antisymmetric molybdyl mode, but belong to different Mo_xO_y species. (chapter 6.7.)

The UV/Vis-spectra support the presence of more than one molybdenum oxide surface species. (chapter 6.3.) A loss of intensity relative to the band maximum (242 nm) at wavelengths higher than 300 nm and a gain of relative intensity at 280 nm is observed. As in the case of the hydrated Mo_xO_y/SBA-15, less but still significant intensity is observed at wavelengths between 300 and 350 nm. It may originate from the presence of isolated octaherals, connected tetrahedral or connected octahedral molybdenum oxide centres or a mixture of these species. The intensity loss at higher wavelengths can be interpreted as a shift in the distribution of those species towards smaller molybdenum oxide species and therefore a higher dispersion than in the hydrated state.

This is also corroborated by XP spectra of a Mo_xO_y/SBA-15 sample with a loading of 5.9 wt.% Mo (0.8 Mo/nm^2) as the Mo 3d 5/2 emission shows a shift of 0.4 eV to higher binding energies as compared to the hydrated state. The determined binding energy is higher than for α-MoO_3 (Mo $3d_{5/2}$: 232.6 eV), which is a bulk reference compound for Mo^{6+}. It can be explained by a higher dispersion of the dehydrated molybdenum oxide (chapter 6.4. and 6.9.1.). Previously, a similar behaviour has been observed for vanadia. [169] Although shifted to smaller average size of the molybdenum oxide species, the broadness of the size distribution seems to be constant as FWHM of the Mo 3d signal is constant at 2.8 eV.

The increase in dispersion of the molybdenum oxide species in the dehydrated state can be also concluded from the XANES region in the XAS, which is almost featureless. A further indication for higher dispersion is also the reduced amplitude at higher Mo-Mo shells in the FT(χ(k)·k^3). Moreover, the coordination of the molybdenum oxide centres changes from distorted octahedral to a more tetrahedral, as the pre-edge is increased after the dehydration. A fit of the pre-edge peak with octahedral and tetrahedral reference compounds (α-MoO_3 and Na_2MoO_4) exhibits an O_h : T_d ratio of 1 : 3. The detailed EXAFS analysis displays a peak at typical Mo-Mo distances in the radial distribution function FT(χ(k)·k^3), which indicates the presence of connected molybdenum centres. Therefore, the SBA-15 supported

molybdenum oxide structures can be described as mixture of tetrahedrally and distorted octahedrally coordinated MoO_4 and MoO_6 units. Additionally, for the octahedral MoO_6 units a similar connection like in the α-MoO_3 building blocks may be assumed. Moreover, besides isolated tetrahedral MoO_4 units, connected MoO_4 units to other MoO_x units may also be present on the SBA-15. (chapter 6.6.) The degree of dispersion and the ratio of the present molybdenum oxide species is independent of the loading and the preparation procedure as the χ(k) for the Mo_xO_y/SBA-15 samples with 1.0 and 5.5 Mo wt.% (0.2 and 0.8 Mo/nm^2) strongly resemble each other.

The analysis of the O K-edge NEXAFS of Mo_xO_y/SBA-15 samples with a loading of 5.9 Mo wt.% (0.8 Mo/nm^2) and 11.1 Mo wt.% (2.4 Mo/nm^2) concerning the present molybdenum oxide structures is very limited due to the lack of appropriate reference substances. For a deeper understanding of the O K-edge details, the application of theoretical calculations is necessary.

Another method, that has been employed to study the connectivity of the molybdenum oxide centres, is NO adsorption on Mo_xO_y/SBA-15 followed by oxidation of the adsorbed NO to other nitric oxides and their observation by IR spectroscopy. (chapter 6.5.) Besides other volatile nitric oxides, vacuum stable IR signals of nitrates coordinated to molybdenum oxide centres have been identified. The found nitrate signals at 1618 and 1573 cm^{-1} have been assigned to bridging and bidentate nitrates, respectively. Furthermore, the results have been verified by similar experiments with isotope labeled ^{15}NO which show a shift of the nitrate signals to 1585 and 1534 cm^{-1}. The presence of bridging surface nitrates implies a strong hint that dimeric and/or oligomeric molybdenum oxide surface species exist besides monomers on Mo_xO_y/SBA-15.

In summary, it can be said regarding the dehydrated state of the Mo_xO_y/SBA-15, that the molybdenum is present as Mo^{6+} and that it is more dispersed than in the hydrated state as shown by XPS. Furthermore, according to UV/Vis, XAS, NEXAFS results the ratio of the

supported molybdenum oxide species seems to be independent of the Mo loading. In contrast to the literature view that only monomeric tetrahedral or square pyramidal molybdenum oxide centres are present, spectroscopic evidence has been found that more than one molybdenum oxide species is present on the SBA-15 support at low Mo densities ($\leq$1.0 Mo/nm^2). Therefore, the structure of SBA-15 supported molybdenum oxide also at low Mo densities can be described as dispersed octahedral and tetrahedral molybdenum oxide centres, which can be monomeric or exhibit connections to each other. Additionally, the ratio of the molybdenum oxide species seems to be independent of the Mo loading as in the hydrated state. A picture of the dispersed molybdenum oxide structures is given in scheme 6.1.

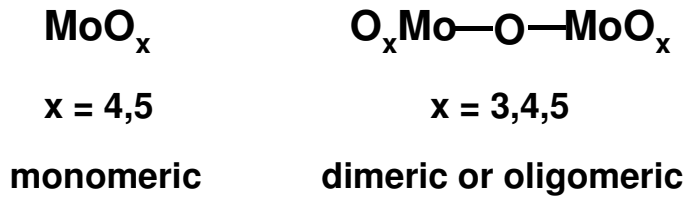

Scheme 6.1: Dispersed molybdenum oxide species present on silica SBA-15.

As the described dehydrated state is also present under *in situ* conditions while propylene oxidation at 500°C, also di- and oligomeric molybdenum oxide centres should be considered as active sites for the reaction.

7. Conclusions and Outlook

7.1. Conclusions

The subject of this study was the investigation of structure of silica SBA-15 supported molybdenum oxide and catalytic activity in propane and propylene oxidation. Therefore, Mo_xO_y/SBA-15 catalysts in a loading range of 1.0 to 21.1 wt.% Mo (0.2 to 9.8 Mo/nm^2) have been prepared by a grafting/ion exchange and incipient wetness impregnation procedure. For the structural characterization of the catalyst, Raman-, UV/Vis-, Photoelectron-, X-ray Absorption- and IR spectroscopy in combination with NO/O_2 adsorption have been used. Also, the structure of the catalyst under reaction conditions in presence of propylene and steam has been studied. For this purpose, a new *in situ* Raman-MS setup was constructed. Furthermore, the effect of the washing on the SBA-15 support structure during the synthesis and scale up was examined.

During the upscaling of the SBA-15 synthesis it was found, that the washing procedure of uncalcined SBA-15 influences the quality of the final product. Washing with single solvent (water *or* ethanol) does not alter the homogeneity and order of the pores in SBA-15 and shows no dependence on the amount of solvent. An increase of the surface area of the SBA-15 can be obtained by a combined washing approach using two solvents (water *and* ethanol), but may change the SBA-15 structure when too much solvent is used. The structural change can be observed as a decrease of the long range order in XRD and as a bulge at a p/p_0 value of 0.45 in the desorption branch of the nitrogen adsorption isotherm,

which is called tensile strength effect and occurs at pore diameters below 50Å. This effect is caused by hydrolysis and re-condensation reactions of the silica in the pore wall during the washing procedure, which lead to a narrowing or widening of certain pore sections and therefore influence the nitrogen desorption behaviour. The benefit of an increased surface area while maintaining a narrow mono-modal pore size distribution can be reached by a controlled washing procedure with reduced quantities of both solvents. Furthermore, it was observed that the influence of the solvent volume on the pore size distribution and the shape of the isotherm is reduced during the scale up of the SBA-15 synthesis.

The Mo_xO_y/SBA-15 catalyst was prepared by a grafting/ion exchange and incipient wetness impregnation procedure. The non-destructive insertion of the precursor during the synthesis was monitored by Raman spectroscopy. After calcinations, a high dispersion of the molybdenum oxide on the support was reached up to 12.1 wt.% Mo (3.5 Mo/nm^2). Above that level, besides a dispersed molybdenum oxide phase crystalline MoO_3 was also formed, which has been detected with very high sensitivity by Raman spectroscopy. The crystalline MoO_3 consists of large needles (2 x 20 µm) and small platelets (diameter 0.5 to 1.0 µm) of α-MoO_3 and small needles (length 0.3 to 1.0 µm) of β'-MoO_3 as identified by HRTEM and XRD. A quantification of the dispersed and the crystalline molybdenum oxide was done by comparison of XRF and EDX data. The Mo loadings of the dispersed molybdenum oxide as determined by EDX have been acquired by choosing 25 crystalline MoO_3-free regions in the sample for the measurement. By this method, the amount of dispersed molybdenum oxide in the range of loadings, where also crystalline MoO_3 is present, was found to be almost constant between 12 and 13 wt.% Mo.

Catalysis tests have been performed on Mo_xO_y/SBA-15 (5.9 wt.% Mo, 0.8 Mo/nm^2) in a tubular quartz made fixed bed reactor for propane and propylene oxidation in a temperature

range from 400 to 500°C. The catalyst showed only very little activity in selective propane oxidation to propylene or other oxygenates. For propylene oxidation, the formation of propionaldehyde, acetone and acrolein has been observed as main products, whereas acrylic acid and acetic acid were detected as minor products. Furthermore, small amounts of ethene, formaldehyde, propylene oxide and acetaldehyde were formed, but have not been quantified. From the variety of different reaction products that are formed in propylene oxidation, it can be concluded that Mo_xO_y/SBA-15 comprises sites active in acid, basic and redox chemistry. Furthermore, products like acetic acid or acetaldehyde, which are formed by C-C bond cleavage, show that electrophilic beside nucleophilic oxygen is present in the supported dispersed molybdenum oxide. Oxa/SBA-15 as silica support reference did not show any catalytic activity apart from CO_x formation at higher temperatures.

For the determination of the structure of supported dispersed molybdenum oxide, a hydrated and a dehydrated state have to be distinguished. The hydrated state exists in the presence of moisture at room temperature, whereas the dehydrated state can be obtained by a thermal treatment at 350 to 500°C in dry synthetic air.

The molybdenum oxide in the dehydrated state at low loadings on the silica SBA-15 support is present in a Mo^{6+} oxidation state and contains dispersed molybdenum oxide as indicated by a shift to higher binding energies (Mo $3d_{5/2}$: 233.6 eV) of Mo 3d peaks in XPS compared to α-MoO_3 (Mo $3d_{5/2}$: 232.6 eV). The homogeneous broadening of the Mo 3d peaks (FWHM: 2.8 eV) showed that probably a molybdenum oxide species distribution of different size is present on the support. Also the additional intensity in the UV/Vis spectra up to 370 nm showed the presence of more than one molybdenum oxide species with probably connected molybdenum oxide centres. A further proof for connections between the molybdenum oxide centres is provided by EXAFS analysis, which exhibits a distinct peak in the Mo-Mo distance range in the FT(χ(k)·k^3). The results for the structure of the

silica supported molybdenum oxide in the hydrated state will require more detailed studies in the future. According to Raman spectroscopy, the supported molybdenum oxide should comprise hepta- or octamolybdate structure motif. In contrast to that, on the basis of XAS and the analysis of the XANES and EXAFS region of the spectra an α-MoO_3 or hexagonal MoO_3 structure motif should be present. All three results have to be seen in the light of the sensitivity of the different methods and that only crystalline bulk references were employed for structure assignment of the supported nanometer sized molybdenum oxide. Therefore, the structure can be described best as preferentially octahedral molybdenum oxide centres, which can be monomers or connected to di- or oligomers.

The dispersion of the molybdenum oxide in the dehydrated state was found to be higher as compared to the hydrated state, which is shown by a further shift to higher binding energies (Mo $3d_{5/2}$: 234.0 eV) for the Mo 3d peaks in XPS. No indication has been found for the presence of reduced molybdenum oxide in Mo^{5+} or Mo^{4+} oxidation state. The broadening of Mo 3d peaks (FWHM: 2.8 eV) suggests a molybdenum oxide species distribution of different size like in the hydrated state. Furthermore, it can be concluded from the almost constant shape of the UV/Vis, XAS, NEXAFS-spectra with increasing molybdenum loading that the ratio of the molybdenum oxide species seems to be Mo loading independent. In the literature, the structure of silica supported molybdenum oxides at low Mo densities ($\leq$1.0 Mo/nm^2) is described as exclusively monomeric tetrahedral or square pyramidal molybdenum oxide centres. [28,30,31] In contrast to that, evidence has been found that molybdenum oxide species of different size and coordination geometry are present on the SBA-15 support at low Mo densities ($\leq$1 Mo/nm^2). The UV/Vis spectra at Mo densities $\geq$1.0 Mo/nm^2 show for instance intensity up to a wavelength of 350 nm, which can only be explained by a second or more molybdenum oxide species, which probably exhibit connections between the molybdenum oxide centres. Additional proof for the connection of molybdenum oxide centres is also provided by XAS, which shows in the

FT(χ(k)·k^3) a peak typical for Mo-Mo distances. The detection of bridging nitrates by IR spectroscopy after NO/O_2 adsorption is another hint for connections between the molybdenum oxide centres. Evidence for the presence of two coordination geometries was found in XAS by a fit of the XANES pre-edge feature, which shows an O_h : T_d ratio of 1 : 3. Further evidence for presence of more than one molybdenum oxide species in Raman spectroscopy is for instance the shift of the molybdyl mode for 991 to 983 cm^{-1} and a change of the intensity ratio of the two bands at 969 and 991 cm^{-1} in *in situ* experiments during the application of steam. Thus, the molybdenum oxide structure at low Mo densities in the dehydrated state can also be described as dispersed tetrahedral and octahedral molybdenum oxide centres. Furthermore, these centres coexist as monomers and connected di- or oligomers on the silica support surface. As in case of the hydrated state, the size distribution of the molybdenum oxide species seems to be independent of the Mo loading.

MoO_x	$O_xMo—O—MoO_x$
x = 4,5	x = 3,4,5
monomeric	dimeric or oligomeric

Scheme 7.1: Dispersed molybdenum oxide species present on silica SBA-15 in dehydrated state.

Therefore, the structures of the supported molybdenum oxide species in the dehydrated state (Scheme 7.1) are much more complex than previously described in the literature. [28,30,31]

7.2. Outlook

A short term objective for further research on the Mo_xO_y/SBA-15 system is, for example, the detailed analysis of the O K-edge NEXAFS spectra by theoretical calculations to further corroborate the existence of supported di- or oligomeric molybdenum oxide species in the dehydrated state.
Also, the systematic catalytic testing of the Mo_xO_y/SBA-15 system should be extended to receive more kinetic data and knowledge about the oxidation reaction pathways. Therefore, in a first stage catalysts with dispersed molybdenum oxide (0.7, 2.0 Mo/nm^2) and a sample, which also contains crystalline MoO_3 besides dispersed molybdenum oxide (7.6 Mo/nm^2) should be tested in propane and propylene oxidation. In a second stage, the Mo_xO_y/SBA-15 system should be compared to the V_xO_y/SBA-15, $V_xMo_yO_z$/SBA-15 mixed oxide system in dispersed state of the same metal density (e.g. 0.7 M/nm^2) and to an inert reference like oxa/SBA-15. Moreover, the influence of steam and the use of another silica support like Aerosil on conversion and selectivity should be tested.

As long term objectives, also *in situ* Raman experiments with ^{18}O isotopes and UV-Raman experiments can be performed to gain a deeper understanding of the supported molybdenum oxide structure. Additionally, a comparison of the molybdenum oxide on different silica supports like SBA-15 and Aerosil for example should be done to obtain proof for the independence of the observed behaviour from the support structure. As silica is a chemically very inert material, it can be useful to apply another metal oxide as support material like titania or a titania coated silica nanostructure (TiO_2/SBA-15) as support for the molybdenum oxides to obtain a better understanding of the support effect.

A point of further interest is the comparison of supported molybdenum oxides with other supported metal oxides like vanadium, chromium or tungsten oxide. Perhaps a general trend can be found that the structure of supported metal oxides at low loadings (≤1.0 M/nm^2) is more complex than described in the literature until now. Additionally, the interactions of different metal oxides like molybdenum oxide and vanadia on the support surface should be studied for their detailed structure and catalytic behaviour to obtain systems of increased complexity, which are closer to the real catalyst.

8. Appendix

8.1. References and Notes

[1] R.K. Grasselli, Catal. Today 49 (1999) 141.

[2] J. Haber, Fundamentals of Hydrocarbon Oxidation in "Handbook of Heterogeneous Catalysis" 2nd edition, Wiley-VCH Verlag, Weinheim (2010) 3359.

[3] O. Ovsitser, Y. Uchida, G. Mestl, G. Weinberg, A. Blume, J. Jäger, M. Dieterle, H. Hibst, R. Schlögl, J. Mol. Catal. A 185 (2002) 291.

[4] T. Ushikubo, H. Nakamura, Y. Koyasu, S. Wajiki, US Patent 5,380,933 (1995).

[5] M. Lin, Appl. Catal. A 207 (2001) 1.

[6] M.A. Banares, N.D. Spencer, M.D. Jones, I.E. Wachs, J. Catal. 146 (1994) 204.

[7] K. Chen, A.T. Bell, E. Iglesia, J. Catal. 209 (2002) 35.

[8] Z. Song, N. Mimura, S. Tsubota, T. Fujitani, S.T. Oyama, Catal. Lett. 121 (2008) 33.

[9] Z. Song, N. Mimura, J.J. Bravo-Suarez, T. Akita, S. Tsubota, S.T. Oyama, Appl. Catal. A 316 (2007) 142. [and ref. therein]

[10] M.A. Banares, H. Hu, I.E. Wachs, J. Catal. 150 (1994) 407.

[11] W. Zhang, S.T. Oyama, J. Phys. Chem. B 100 (1996) 10759.

[12] H. Liu, E. Iglesia, J. Catal. 208 (2002) 1.

[13] J. Mol, P.W.N.M. Leeuwen, Metathesis of Alkenes in "Handbook of Heterogeneous Catalysis" 2nd edition, Wiley-VCH Verlag, Weinheim (2010) 3240.

[14] J. Handzlik, J. Ogonowski, R. Dula, J. Stoch, E.M. Serwicka, React. Kinet. Catal. Lett. 79 (2003) 135.

[15] J.J.P. Biermann, F.J.J. Janssen, J.R.H. Ross, Appl. Catal. A 86 (1992) 165.

[16] I. Nova, L. Lietti, L. Casagrande, L Dall'Acqua, E. Giamello, P. Forzatti, Appl. Catal. B 17 (1998) 245.

[17] S. Lowell, J. Shields, and M.A.Thomas, eds., Characterization of Porous Solids and Powders: Surface Area, Pore Size and Density, Kluwer Acadamic Publishers, Dordrecht / Boston / London, 2004, chapter. 4.

[18] J. Leyrer, R. Margraf, E. Taglauer, H. Knözinger, Surf. Sci. 201 (1988) 603.

[19] R. A. Rajadhyaksha, H. Knözinger, Appl. Catal. 51 (1989) 81.

[20] J. Leyrer, D. Mey, H. Knözinger, J. Catal. 24 (1990) 349.

[21] V. Chiola, J.E. Ritsko, C.D. Vanderpool, US Patent 3,556,725 (1971).

[22] J.S. Beck, C.T.-W. Chu, I.D. Johnson, C.T. Kresge, M.E. Leonowicz, W.J. Roth, J.W. Vartuli, WO Patent 91/11390 (1991).

[23] D.Y. Zhao, J.L. Feng, Q.S. Huo, N. Melosh, G.H. Fredrickson, B.F. Chmelka, G.D. Stucky, Science 279 (1998) 548.

[24] D. Zhao, Q. Huo, J. Feng, B.F. Chmelka, G.D. Stucky, J. Am. Chem. Soc. 120 (1998) 6024.

[25] K. Cassiers, T. Linssen, M. Mathieu, M. Benjelloun, K. Schrijnemakers, P. Van Der Voort, P. Cool, E.F. Vansant, Chem. Mater. 14 (2002) 2317.

[26] R. Herbert, D. Wang, R. Schomäcker, R. Schlögl, C. Hess Chem. Phys. Chem. 10 (2009) 2230.

[27] E. Vansant, P. van der Voort, and K. Vranken, Characterization and Chemical Modifcation of the Silica Surface, in Studies in Surface Science and Catalysis, B. Delmon and J.T.Yates, eds., vol. 93, Elsevier, 1995, chapter 3 to 6.

[28] H. Hu, I.E. Wachs, S.R. Bare, J. Phys. Chem. 99 (1995) 10897.

[29] C.C. Williams, J.G. Ekerdt, J.M. Jehng, F.D. Hardcastle, A.M. Turek, I.E. Wachs, J. Phys. Chem. 95 (1991) 8781.

[30] R. Radhakrishnan, C. Reed, S.T. Oyama, M. Seman, J.N. Kondo, K. Domen, Y. Ohminami, K. Asakura, J. Phys. Chem. B 105 (2001) 8519.

[31] S. Chempath, Y. Zhang, A.T. Bell, J. Phys. Chem. C 111 (2007) 1291.

[32] N. Ohler, A.T. Bell J. Phys. Chem. B 110 (2006) 2700.

[33] N. Ohler, A.T. Bell, J. Phys. Chem. B 109 (2005) 23419.

[34] T. Ressler, A. Walter, Z.-D. Huang, W. Bensch, J. Catal. 254 (2008) 170.

[35] Z. Huang, W. Bensch, W. Sigle, P.A. van Aken, L. Kienle, T. Vitoya, H. Modrow, T. Ressler, J. Mater. Sci. 43 (2008) 244.

[36] Y. Lou, H. Wang, Q. Zhang, Y. Wang, J. Catal. 247 (2007) 245.

[37] J.B. Peri, J. Phys. Chem. 86 (1982) 1615.

[38] K. Hadjiivanov, Catal. Rev. - Sci. Eng. 42 (2000) 71.

[39] G.T. Pott, W.H.J. Stork, Preparation of Catalysts (B. Delmon, P.A. Jacobs, G. Pocelet, eds.) Elsevier, Amsterdam 1976, p. 537.

[40] T. Fransen, P.C. Van Berge, P. Mars, Preparation of Catalysts (B. Delmon, P.A. Jacobs, G. Pocelet, eds.) Elsevier, Amsterdam 1976, p. 405.

[41] M.A. Banares, H. Hu, I.E. Wachs, J. Catal. 155 (1995) 249.

[42] E.L. Lee, I.E. Wachs, J. Phys. Chem. C 111 (2007) 14410.

[43] G. Mestl, T.K.K. Srinivasan, Catal. Rev.-Sci. Eng. 40 (1998) 451.

[44] N. Magg, B. Immaraporn, J.B. Giorgi, T. Schroeder, M. Bäumer, J. Döbler, Z. Wu, E. Kondratenko, M. Cherian, M. Baerns, P.C. Stair, J. Sauer, H.J. Freund, J. Catal. 226 (2004) 88. (and ref. therein)

[45] M. Hävecker, M. Cavalleri, R. Herbert, R. Follath, A. Knop-Gericke, C. Hess, K. Hermann, R. Schlögl, Phys. Status Solidi B 246 (2009) 1459.

[46] M. Cavalleri, K. Hermann, A. Knop-Gericke, M. Hävecker, R. Herbert, C. Hess, A. Oestereich, J. Döbler, R. Schlögl, J. Catal. 262 (2009) 215.

[47] A. Walter, R. Herbert, C. Hess, T. Ressler, Chem. C. J. 4 (2010) 3.

[48] Y. Iwasawa, K. Asakura, H. Ishii, H. Kuroda, Z. Phys. Chem. 144 (1985) 105.

[49] Y. Iwasawa, Adv. Catal. 35 (1987) 265.

[50] M. Matsuoka, T. Kamegawa, R. Takeuchi, M. Anpo, Catal. Today 122 (2007) 39.

[51] G. Xiong, C. Li, Z. Feng, P. Ying, Q. Xin, J. Liu, J. Catal. 186 (1999) 234.

[52] S. Higashimoto, Y .Hua, R. Tsumura, K. Iino, M. Matsuoka, H. Yamashita , Y.G. Shul, M. Che, M. Anpo, J. Catal. 235 (2005) 272.

[53] J.Y. Piquemal, J.-M. Manoli, P. Beaunier, A. Ensuque, P. Tougne, A.P. Legrand, J.M. Bregeault, Microp. Mesop. Mat. 29 (1999) 291.

[54] J.P. Thielemann, J. Kröhnert, C. Hess, J. Phys. Chem. C 114 (2010) 17092.

[55] I. Horvath, Encyclopedia of Catalysis, Vol. 3, Wiley-Interscinece, New Jersey, 2003.

[56] R. K. Grasselli, Top. Catal. 21 (2002) 79.

[57] R. Schlögl, Modern Heterogeneous Oxidation Catalysis: Design, Reactions and Characterization, Wiley-VCH, Weinheim (2009) 1.

[58] A. Bielanski, J. Haber, Oxygen in catalysis, Marcel Dekker, New York, 1991.

[59] P. Mars, D.W. van Krevelen, Chem. Eng. Sci. 3 (1954) 41.

[60] R. Schlögl, A. Knop-Gericke, M. Hävecker, U. Wild, D. Frickel, T. Ressler, R.E. Jentoft, J. Wienold, G. Mestl, A. Blume, O. Timpe, Y. Uchida, Top. Catal. 15 (2001) 219.

[61] www.fluidat.com, accessed 6/2/2010.

[62] T. Ressler, J. Synch. Rad. 5 (1998) 118.

[63] J.J. Rehr, C.H. Booth, F. Bridges, S.I. Zabinsky, Phys. Rev. B 49 (1994) 12347.

[64] T. Ressler, S.L. Brock, J. Wong, S.L. Suib, J. Phys. Chem. B 103 (1999) 6407.

[65] http://www.ixasportal.net/ixas/images/ixas_mat/StandardsCriteria_July25_2000.pdf, accessed 2/1/2010.

[66] Numerical Recipes: The Art of Scientific Computing, Third Edition, Cambridge University Press (2007).

[67] E.M. Vass, M. Hävecker, S. Zafeiratos, D. Teschner, A. Knop-Gericke, R. Schlögl, J. Phys. 20 (2008) 1.

[68] H. Bluhm, M. Hävecker, A. Knop-Gericke, M. Kiskinova, R. Schlögl, M. Salmeron, MRS Bull. 7 (2007) 602.

[69] A. Knop-Gericke, E. Kleimenov, M. Hävecker, R. Blume, D. Teschner, S. Zafeiratos, R. Schlögl, V.I. Bukhtiyarov, V.V. Kaichev, I.P. Prosvirin, A.I. Nizovskii, H. Bluhm, A. Barinov, P. Dudin, M. Kiskinova, Adv. Catal. 52 (2008) 215.

[70] L. Jelinek, E. Kováts, Langmuir 10 (1994) 4225.

[71] J.H. de Boer, B.G. Linsen, T. van der Plas, G.J. Zondervan, J. Catal. 4 (1965) 649.

[72] Q. Huo, D. Margolese, U. Ciesla, P. Feng, T. Gier, P. Sieger, R. Leon, P. Petroff, F. Schüth, G. Stucky, Nature 368 (1994) 317.

[73] F. Di Renzo, A. Galarneau, P. Trens, F. Fajula in Handbook of Porous Solids, Wiley VCH, Weinheim, F. Schüth, K.S.W. Sing, J. Weitkamp (2002) 1311.

[74] A. Sayari in The Chemistry of Nanostructured Materials, World Scientific Publishing Co. Pte. Ltd., Singapore-London (2003) 39.

[75] S. Jun, S.H. Joo, R. Ryoo, M. Kruk, M. Jaroniec, Z. Liu, T. Ohsuna, O. Terasaki, J. Am. Chem. Soc. 122 (2000) 10712.

[76] R. Ryoo, C.H. Ko, M. Kruk, V. Antochshuk, M. Jaroniec, J. Phys. Chem. B 104 (2000) 11465.

[77] M. Imperor-Clerc, P. Davidson, and A. Davidson, J. Am. Chem. Soc. 122 (2000) 11925.

[78] I.G. Shenderovich, G. Buntkowsky, A. Schreiber, E. Gedat, S. Sharif, J. Albrecht, N.S. Golubev, G.H. Findenegg, H.H. Limbach J. Phys. Chem. B 107 (2003) 11924.

[79] C.G. Sonwane, P.J. Ludovice, J. Mol. Catal. A 238 (2005) 135.

[80] C.M. Yang, B. Zibrowius, W. Schmidt, F. Schüth, Chem. Mater. 15 (2003) 3739.

[81] S. Ruthstein, V. Frydman, S. Kababya, M. Landau, D. Goldfarb, J. Phys. Chem. B 107 (2003) 1739.

[82] A. Galarneau, H. Cambon, F. Di Renzo, F. Fajula, Langmuir 17 (2001) 8328.

[83] M. Kruk, M. Jaroniec, C.H. Ko, R. Ryoo, Chem. Mater. 12 (2000) 1961.

[84] A.S.M. Chong, X.S. Zhao, J. Phys. Chem. B 107 (2003) 12650.

[85] C.M. Yang, B. Zibrowius, W. Schmidt, F. Schüth, Chem. Mater. 16 (2004) 2918.

[86] L.M. Yang, Y.J. Wang, G.S. Luo, Y.Y. Dai, Microp. Mesop. Mat. 81 (2005) 107.

[87] R. van Grieken, G. Calleja, G.D. Stucky, J.A. Melero, R.A. Garcia, J. Iglesias, Langmuir 19 (2003) 3966.

[88] B. Tian, X. Liu, C. Yu, F. Gao, Q. Luo, S. Xie, B. Tu, D. Zhao, Chem. Commun. (2002) 1186.

[89] Z. Luan, E.M. Maes, P.A.W. van der Heide, D. Zhao, R.S. Czernuszewicz, L. Kevan, Chem. Mater. 11 (1999) 3680.

[90] C. Hess, Chem. Phys. Chem. 10 (2009) 319. (and ref. therein)

[91] S. Perathoner, P. Lanzafame, R. Passalacqua, G. Centi, R. Schlögl, D.S. Su, Microp. Mesop. Mat. 90 (2006) 347.

[92] M.L. Ojeda, J.M. Esparza, A. Campero, S. Cordero, I. Kornhauser, F. Rojas, Phys. Chem. Chem. Phys. 5 (2003) 1859.

[93] Y.K. Bae, O.H. Han, Microp. Mesop. Mat. 106 (2007) 304.

[94] O.P. Tkachenko, K.V. Klementiev, E. Löffler, I. Ritzkopf, F. Schüth, M. Bandyopadhyay, S. Grabowski, H. Gies, V. Hagen, M. Muhler, L. Lu, R.A. Fischer, W. Grünert, Phys. Chem. Chem. Phys. 5 (2003) 4325.

[95] M. Kruk, M. Jaroniec, S.H. Joo, R. Ryoo, J. Phys. Chem. B 107 (2003) 2205.

[96] P. Van Der Voort, P.I. Ravikovitch, K.P. De Jong, M. Benjelloun, E. Van Bavel, A.H. Janssen, A.V. Neimark, B.M. Weckhuysen, E.F. Vansant, J. Phys. Chem. B 106 (2002) 5873.

[97] J.C. Groen, L.A.A. Peffer, J. Pérez-Ramírez, Microp. Mesop. Mat. 60 (2003) 1.

[98] S. Lowell, J.E. Shields, M.A. Thomas, M. Thommes, Characterization of Porous Solids and Powders: Surface, Area, Pore Size and Density, Kluwert Academic Publishers, Dordrecht / Boston / London (2004).

[99] K.S.W. Sing, D.H. Everett, R.A.W. Haul, L. Moscou, R.A.Pierotti, J. Rouquerol, T. Siemieniewska, Pure Appl. Chem. 57 (1985) 603.

[100] K. Morishige, H. Fujii, M. Uga, D. Kinukawa, Langmuir 13 (1997) 3494.

[101] K. Morishige, M. Ito, J. Chem. Phys. 117 (2002) 8036.

[102] P. Van Der Voort, P.I. Ravikovitch, K.P. De Jong, A.V. Neimark, A.H. Janssen, M. Benjelloun, E. Van Bavel, P. Cool, B.M. Weckhuysen, E.F. Vansant, Chem. Commun. (2002) 1010.

[103] V. Meynen, P. Cool, E.F. Vansant, Microp. Mesop. Mat. 104 (2007) 2.

[104] B.S. Tian, C. Yang, J. Phys. Chem. C 113 (2009) 4925.

[105] C. Hess, J.D. Hoefelmeyer, T.D.Tilley, J. Phys. Chem. B 108 (2004) 9703.

[106] Lin-Vien, D.; Colthup, N. B.; Fateley, W. G.; Grasselli, J. G. The Handbook of Infrared and Raman Characteristic Frequencies of OrganicMolecules; Academic Press, Boston, (1991).

[107] C.J. Brinker, R. Kirkpatrick, D.R. Tallant, B.C. Bunker, B. Montez, J. Non-Cryst. Solids 99 (1988) 418.

[108] R.H. Stolen, G.E. Walrafen, J. Chem. Phys. 64 (1976) 2623.

[109] Griffith, Lesniak, J. Chem. Soc. A (1969) 1066.

[110] P. Beato, “Synthesis and characterization of realistic molybdenum oxide based model systems in heterogeneous catalysis”, Dissertation, TU-Berlin 2005, p. 36.

[111] M. Dieterle, “In situ Resonance Raman Studies of Molybdenum Oxide Based Selective Oxidation Catalysts”, Dissertation, TU-Berlin 2001, p. 144.

[112] J. Wienold, R.E. Jentoft, T. Ressler, Eur. J. Inorg. Chem. (2003) 1058.

[113] T. Arii, Y. Sawada, N. Kieda, S. Seki, J. Mass. Spectrom. Soc. Jpn. 47 (1999) 354.

[114] E.H.M. Diefallah, A.A.El-Bellihi, S.N.Basahel, M.A.Wahab, Z.A.Omran, Thermochimica Acta 230 (1993) 143.

[115] L. Kihlborg, Arkiv foer Kemi 21 (1963) 357.

[116] J.B. Parise, E.M. McCarron III, R. von Dreele, J.A. Goldstone, J. Solid State Chem. 93 (1991) 193.

[117] J.B. Parise, E.M. McCarron III, A.W. Sleight, Mat. Res. Bull. 22 (1987) 803.

[118] E.M. McCarron III, J.C. Calabrese, J. Solid State Chem. 91 (1991) 121.

[119] K. Chen, A.T. Bell, E. Iglesia, J. Phys. Chem. B 104 (2004) 1292.

[120] F. Solymosi, K. Kedves, Catal. Lett. 77 (2001) 179.

[121] J.C. Védrine, E.K. Novakova, E.G. Derouane, Catal. Today 81 (2003) 247.

[122] J. Haber, Stud. Surf. Sci. Catal. 110 (1997) 1.

[123] G. Centi, F. Cavani, F. Trifirò, Selective Oxidation by Heterogeneous Catalysis, Kluwer Academic Publishers, New York (2001).

[124] T. Liu, M. Forissier, G. Coudurier, J.C. Vedrine, J. Chem. Soc. Faraday Trans. 1 85 (1989) 1607.

[125] A. Vaghi, A. Castellan, J.C.J. Bart, N. Giordano, J. Catal. 42 (1976) 381.

[126] E.L. Lee, I.E. Wachs, J. Phys. Chem. C 112 (2008) 6487.

[127] T.M. McEvoy, K.J. Stevenson, Langmuir 21 (2005) 3521.

[128] Signal at 422 cm^{-1} originates from the sample holder.

[129] D.R. Tallant, B.C. Bunker, C.J. Brinker, C.A.Balfe, Mater. Res. Soc. Symp. Proc. 73 (1986) 261.

[130] B.C. Brinker, D.R. Tallant, E.P. Roth, C.S. Ashley, Mater. Res. Soc. Symp. Proc. 61 (1986) 387.

[131] M. de Boer, A.J. van Dillen, D.C. Koningsberger, J.W. Geus, M.A. Vuurman, I.E. Wachs, Catal. Lett. 11 (1991) 227.

[132] L.J. Gregoriades, J. Döbler, J. Sauer, J. Phys. Chem. C 114 (2010) 2967.

[133] T.V. Venkov, C. Hess, F.C. Jentoft, Langmuir 23 (2007) 1768.

[134] R.K. Rana, B. Viswanathan, Catal. Lett. 52 (1998) 25.

[135] The spectra of hydrated Mo_xO_y/SBA-15 with a loading of 13.9 wt.% Mo (3.2 Mo/nm^2) and 19.9 wt.% Mo (6.2 Mo/nm^2) are not shown as the reflectance is below 10%, which makes the Kubelka Munk conversion unreliable. The reflectance spectra do not show any fundamental difference in shape to those of the lower loaded samples (5.9 and 12.1 wt.% Mo)

[136] R.S. Weber, J. Catal. 151 (1995) 470.

[137] M. Fournier, C. Louis, M. Che, P. Chaquin, D. Masure, J. Catal. 119 (1989) 400. (and ref. therein)

[138] H. Jezlorowski, H. Knözinger, J. Phys. Chem. 83 (1979) 1166.

[139] Y.V. Plyuto, I.V. Babich, I.V. Plyuto, A.D. Van Langeveld, J.A. Moulijn, Coll. Surf. A 125 (1997) 225.

[140] S.R. Seyedmonir, R.F. Howe, J. Catal. 110 (1989) 216.

[141] C.N. Asmolov, O.V. Krylov, Kim. Katal. 11 (1970) 1028.

[142] M. Matsuoka, T. Kamegawa, R. Takeuchi, M. Anpo, Catal. Today 122 (2007) 39.

[143] J. Moulder, W. Stickle, P. Sobol, and K. Bomben, eds., Handbook of X-ray Photoelectron Spectroscoy, Perkin-Elmer Corporation, 1992.

[144] R.J. Colton, A.M. Guzman, J.W. Rabalais, J. Appl. Phys. 49 (1978) 409.

[145] A.M. Venezia, Catal. Today 77 (2003) 359.

[146] Z. Li, L. Gao, S. Zheng, Appl. Catal. A 236 (2002) 163.

[147] C. Hess, J. Catal. 248 (2007) 120.

[148] C. Hess, R. Schlögl, Chem. Phys. Lett. 432 (2006) 139.

[149] I.E. Wachs, Catal. Today 27 (1996) 437.

[150] P.S. Braterman, Metal Carbonyl Spectra, Academic Press, London, 1975.

[151] B. Djonev, B. Tsyntsarski, D. Klissurski, K. Hadjiivanov, J. Chem. Soc., Faraday Trans. 93 (1997) 4055.

[152] K. Hadjiivanov, D.G. Klissurski, V.P. Bushev, J. Chem. Soc. Faraday Trans., 91 (1995) 149.

[153] J. Laane, J.R. Ohlsen, Prog. Inorg. Chem. 28 (1986) 465.

[154] K. Nakamoto, Infrared Spectra of Inorganic and Coordination Compounds, 2nd ed., Wiley, New York (1970).

[155] A. Givan, A. Loewenschuss, J. Chem. Phys. 90 (1989) 6135.

[156] K. Hadjiivanov, D. Klissurski, G. Ramis, G. Busca, Appl. Catal. B 7 (1996) 251.

[157] T. Ohno, F. Hatayama, Y. Toda, S. Konishi, H. Miyata, Appl. Catal. B 5 (1994) 89.

[158] K. Hadjiivanov, H. Knözinger, B. Tsyntsarski, L. Dimitrov, Catal. Lett. 63 (1999) 35.

[159] F.A. Cotton, G. Wilkinson, Advanced Inorganic Chemistry, 4th ed., Wiley, New York (1980).

[160] N. Ahmetov, Inorg. Chem., Vyshaya Schola, Moscow (1985).

[161] M.M. Kantcheva, V.P. Bushev, K. Hadjiivanov, J. Chem. Soc. Faraday Trans 88 (1992) 3087.

[162] T. Weingand, S. Kuba, K. Hadjiivanov, H. Knözinger, J. Catal. 209 (2002) 539.

[163] T. Shimanouchi, Tables of Molecular Vibrational Frequencies Consolidated Volume II, J. Phys. Chem. Ref. Data 6 (1972) 993.

[164] G. Wu, T. Sekiguchi, Y. Baba, I. Shimoyama, Nucl. Instr. and Meth. in Phys. Res. B 245 (2006) 406.

[165] DFT-Calculations are currently performed in the Group of Prof. Hermann at the Theory Department of the Fritz-Haber-Institute (Berlin).

[166] A. Sadezky, H. Muckenhuber, H. Grothe, R. Niessner, U. Pöschl, Carbon 43 (2005) 1731.

[167] F.D. Hardcastle, I.E. Wachs, J. Raman Spec. 21 (1990) 683.

[168] M.A. Banares, I.E. Wachs, J. Raman Spec. 33 (2002) 359.

[169] C. Hess, G. Tzolova-Müller, R. Herbert, J. Phys. Chem. C 111 (2007) 9471.

8.2. List of Figures

3.9 Small angle XRD of SBA-15 unwashed (**1A**), after washing with 30 ml ethanol (**1B**) and 30 ml water (**1C**). The intensities are normalized to the 100 reflex and offset by 0.4 (**1A**) and 0.2 (**1B**).

3.10 N_2 adsorption/desorption isotherms of SBA-15 unwashed (**2A**), after washing with 5 ml (**2B**) and 30 ml (**2C**) quantities of solvent. The isotherms are offset by 350 (**2A**) and 50 (**2B**) cc/g.

3.11 NLDFT pore size distribution of SBA-15 unwashed (**2A**), after washing with 5 ml (**2B**) and 30 ml (**2C**) quantities of solvent calculated from the adsorption branch of the isotherm. The pore size distributions are offset by 0.05 (**2A**) and 0.025 (**2B**) cc/A/g.

3.12 NLDFT pore size distribution of SBA-15 unwashed (**2A**), after washing with 5 ml (**2B**) and 30 ml (**2C**) quantities of solvent calculated from the desorption branch of the isotherm. The pore size distributions are offset by 0.5 (**2A**) and 0.25 (**2B**) cc/A/g.

3.13 Small angle XRD of SBA-15 unwashed (**2A**), after washing with 30 ml ethanol (**2B**) and 30 ml water (**2C**). The intensities are normalized to the 100 reflex and offset by 0.4 (**2A**) and 0.2 (**2B**).

3.14 N_2 adsorption/desorption isotherms of SBA-15 sample **3** divided into a 1x half-batch unwashed (**3A**), after washing with 5 ml (**3B**) and 30 ml (**3C**), a 3x half-batch washed with 120 ml (**3D**) and a 9x half-batch washed with 350 ml (**3E**) quantities of solvent. The isotherms are offset by 1100 (**3A**), 700 (**3B**), 500 (**3C**), 300 (**3D**) cc/g.

3.15 NLDFT pore size distribution of SBA-15 sample **3** calculated from the adsorption branch of the isotherm. The sample was divided into a 1x half-batch unwashed (**3A**), after washing with 5 ml (**3B**) and 30 ml (**3C**), a 3x half-batch washed with 120 ml (**3D**) and a 9x half-batch washed with 350 ml (**3E**) quantities of solvent The pore size distributions are offset by 0.16 (**3A**), 0.12 (**3B**), 0.08 (**3C**) and 0.04 (**3D**) cc/A/g.

3.16 XRD of SBA-15 sample **3** divided into a 1x half-batch unwashed (**3A**), after washing with 5 ml (**3B**) and 30 ml (**3C**), a 3x half-batch washed with 120 ml (**3D**) and a 9x half-batch washed with 350 ml (**3E**) quantities of solvent. The intensities are normalized to the 100 reflex and offset by 0.8 (**3A**), 0.6 (**3B**), 0.4 (**3C**) and 0.2 (**3D**). Note: Oscillations are an artefact in the measurement.

4.1 Raman spectrum at 633 nm showing (a) APTMS functionalised SBA-15; (b) APTMS functionalised SBA-15 after ion exchange with AHM; (c) AHM (Roth). The spectra are offset for clarity.

4.2 Decomposition of APTMS/SBA-15 after ionexchange with AHM to 12.1 wt.% Mo Mo_xO_y/SBA-15; TG and DSC (left); MS (right)

4.3 Decomposition of APTMS/SBA-15 after ion exchange with $K_2C_2O_4 \cdot 2\ H_2O$ to oxa/SBA-15; TG and DSC (left); MS (right) and SBA-15-APTMS; (A) TG and DSC; (B) MS

4.4 TG and DSC during decomposition of APTMS/SBA-15.

4.5 XRD of Mo_xO_y/SBA-15 with 13.9 wt.% / 6.8 Mo/nm^2; Insets a and b: Details of XRD of Mo_xO_y/SBA-15 with 13.9 wt.% / 6.8 Mo/nm^2 (red), α-MoO_3 Fit (black)

4.6 SEM picture of of α-MoO_3 crystallites beside

4.7 HRTEM micrograph of plate like α- and needle like β'-MoO_3 crystallites.

4.8 Structures of α, β and β'-MoO_3

4.9 SEM picture shows a Mo_xO_y/SBA-15 sample with 21.1 wt.% Mo (9.8 Mo/nm²). The inset indicates the size of a EDX sampling spot, which is well separated from surrounding MoO_3 crystallites.

4.10 Loading-dependent distribution of dispersed and crystalline molybdenum oxide. The total Mo-loading has been measured by XRF (green) and Mo-loading of the dispersed Mo_xO_y-species by EDX (red).

5.1 Conversion versus selectivity plot for propylene oxidation ($C_3H_6/O_2/N_2$ = 3/7/90) over 5.9 wt.% Mo (0.8 Mo/nm^2) Mo_xO_y/SBA-15 at 500°C and a GHSV of 1000, 2000 and 3000 ml$\cdot h^{-1} \cdot g^{-1}$.

6.1 Room temperature Raman spectra of hydrated (a) oxa/SBA-15 and Mo_xO_y/SBA-15 (b) 5.9 wt.% Mo / 0.8 Mo/nm^2; (c) 8.4 wt.% Mo / 1.5 Mo/nm^2 (d) 12.1 wt.% Mo / 3.5 Mo/nm^2 (e) 13.9 wt.% Mo / 6.8 Mo/nm^2. The spectra are offset for clarity.

6.2 Room temperature Raman spectra of dehydrated (a) oxa/SBA-15 and Mo_xO_y/SBA-15 (b) 5.9 wt.% Mo / 0.8 Mo/nm^2; (c) 8.4 wt.% Mo / 1.5 Mo/nm^2 (d) 11.0 wt.% Mo / 2.4 Mo/nm^2 (e) 12.1 wt.% Mo / 3.5 Mo/nm^2 (f) 13.9 wt.% Mo / 6.8 Mo/nm^2. The spectra are offset for clarity.

6.3 Magnified region from 850 to 1100 cm^{-1} of Fig. 6.3. A linear background subtraction has been performed from 850 to 1100 cm^{-1}. The spectra are normalized with respect to the peak at 970 cm^{-1} and offset for clarity.

6.4 Raman spectra of Mo_xO_y/SBA-15 at 500°C in N_2/O_2 (80:20) flow at 50 ml/min (a) 5.9 wt.% Mo; 0.8 Mo/nm^2; (b) 1.0 wt.% Mo; 0.2 Mo/nm^2 (Fit of the Si-OH stretching (dotted red)) and (c) 5.5 wt.% Mo; 0.6 Mo/nm^2 (incipient wetness). The spectra are offset for clarity.

6.5 UV/Vis spectrum of (a) 5.9 wt.% Mo (0.8 Mo/nm^2), (b) 11.1 wt.% Mo (2.0 Mo/nm^2), c) 13.9 wt.% Mo (3.2 Mo/nm^2), d) 19.9 wt.% Mo (6.2 Mo/nm^2) and references compounds Na_2MoO_4 (e), $Na_2Mo_2O_7$ (f) and MoO_3 (g) in the hydrated state. The inset shows normalized spectra. [135]

6.6 UV/Vis spectrum of a) 5.9 wt.% Mo (0.8 Mo/nm^2), b) 11.1 wt.% Mo (2.0 Mo/nm^2), c) 13.9 wt.% Mo (3.2 Mo/nm^2), d) 19.9 wt.% (6.2 Mo/nm^2) and references compounds Na_2MoO_4 (e), $Na_2Mo_2O_7$ (f) and MoO_3 (g) in the dehydrated state. The inset shows normalized spectra.

6.7 XP survey spectrum of 5.9 wt.% (0.8 Mo/nm^2) Mo_xO_y/SBA-15 in the dehydrated state

6.8 XPS of the Mo 3d region of 5.9 wt.% (0.8 Mo/nm^2) Mo_xO_y/SBA-15 in the dehydrated (black) and the hydrated state (red).

6.9 XP spectrum of the Mo 3d region shows the contributions dispersed Mo_xO_y species (red) and crystalline MoO_3 (blue) of 21.1 wt.% Mo (13.2 Mo/nm^2) Mo_xO_y/SBA-15 in the dehydrated state.

6.10 Transmission IR spectra showing the formation of molybdenum dinitrosyl species [Mo^{4+}-$(NO)_2$] on reduced 5.9 wt.% Mo (0.8 Mo/nm^2) Mo_xO_y/SBA-15 during exposure to ^{14}NO at room temperature

6.11 Transmission IR spectra showing the formation of molybdenum dinitrosyl species [Mo^{4+}-$(NO)_2$] on reduced 5.9 wt.% Mo (0.8 Mo/nm^2) Mo_xO_y/SBA-15 during exposure to ^{15}NO at room temperature

6.12 Transmission IR spectra during exposure of the molybdenum dinitrosyl species [Mo^{4+}-$(NO)_2$] on 5.9 wt.% Mo (0.8 Mo/nm^2) Mo_xO_y/SBA-15 to a mixture of NO (2 mbar) and O_2 (7.4 mbar). Note: The band at 1606 cm^{-1} is due to gas phase NO_2.

6.13 Transmission IR difference spectra of oxidized 5.9 wt.% Mo (0.8 Mo/nm^2) Mo_xO_y/SBA-15 (a) after treatment with NO (2.0 mbar) and O_2 (7.3 mbar) at room temperature, (b) after treatment at 150°C followed by evacuation to 10^{-5} mbar at room temperature, (c) after treatment at 100°C at 10^{-5} mbar and subsequent cooling to room temperature. The spectra are offset for clarity.

6.14 Transmission IR difference spectra of oxidized 5.9 wt.% Mo (0.8 Mo/nm^2) Mo_xO_y/SBA-15 (a) after treatment with NO (2.0 mbar) and O_2 (7.3 mbar) at room temperature, (b) after treatment at 150°C followed by evacuation to 10^{-5} mbar at room temperature, (c) after treatment at 100°C at 10^{-5} mbar and subsequent cooling to room temperature. The spectra are offset for clarity.

6.15 Transmission IR difference spectra of oxidized SBA-15 (ox) (a) after treatment with NO (10.0 mbar), (b) after treatment with NO (2.0 mbar) and O_2 (8.0 mbar) at room temperature and (c) after evacuation to 10^{-5} mbar at room temperature. The spectra are offset for clarity.

6.16 Transmission IR difference spectra of oxidized 5.9 wt.% Mo (0.8 Mo/nm^2) Mo_xO_y/SBA-15 (a) after treatment with ^{15}NO (6.1 mbar) and O_2 (2 mbar), (b) after evacuation to $4 \cdot 10^{-5}$ mbar at room temperature (c) after evacuation to $1.4 \cdot 10^{-5}$ mbar at room temperature. The spectra are offset for clarity.

6.17 Transmission IR difference spectra of oxidized Mo_xO_y/SBA-15 with a loading of 10.2 wt.% Mo (2.2 Mo/nm^2) (a) after treatment with ^{15}NO (6.1 mbar) and O_2 (2 mbar) and evacuation to $1.4.10^{-5}$ mbar at room temperature (b) after treatment with ^{14}NO (6.1 mbar) and O_2 (2 mbar) and evacuation to $2.2 \cdot 10^{-5}$ mbar at room temperature. The spectra are offset for clarity.

6.18 Coordinated nitrates present on Mo_xO_y/SBA-15 after exposure to a $^{14}NO/O_2$ mixture and evacuation

6.19 Mo K edge XAFS $\chi(k)$ of dehydrated MoxOy/SBA-15 with (a) 1.0 wt.% Mo; 0.2 Mo/nm^2 and (b) 5.5 wt.% Mo (0.6 Mo/nm^2) after thermal treatment in 20 vol.% O_2 in He at 623 K. The spectra are offset for clarity.

6.20 Mo K edge XANES spectra of dehydrated Mo_xO_y/SBA-15 with 5.5 wt.% Mo (0.6 Mo/nm^2) [solid] and 1.0 wt.% Mo (0.2 Mo/nm^2) [dotted].

6.21 Evolution of Mo K edge FT($\chi(k)\cdot k^3$) of Mo_xO_y/SBA-15 with 5.5 wt.% Mo (0.6 Mo/nm^2) during thermal treatment in 20 vol.% O_2 in He in the temperature range from 300 to 623 K (5 K/min).

6.22 Mass trace of water (m/z=18) during thermal treatment of Mo_xO_y/SBA-15 with 5.5 wt.% Mo (0.6 Mo/nm^2) in 20 vol.% O_2 in He in the temperature range from 300 to 623 K (5 K/min).

6.23 Mo K edge XANES spectra [top] and Mo K edge FT($\chi(k)\cdot k^3$) [bottom] of (c) dehydrated and (d) hydrated Mo_xO_y/SBA-15 (5.5 wt.% Mo / 0.6 Mo/nm^2) together with reference oxides (a) $Na_2Mo_2O_7$, (b) Na_2MoO_4, (e) α-MoO_3. The spectra are offset for clarity.

6.24 Direct comparison of [top] Mo K edge XANES spectra and Mo K edge FT($\chi(k)\cdot k^3$) [bottom] of hydrated [solid] and dehydrated Mo_xO_y/SBA-15 with 5.5 wt.% Mo (0.6 Mo/nm^2) [dotted].

6.25 Refinement of sum [dotted] of XANES spectra of references MoO_3 and Na_2MoO_4 [dashed] to Mo K edge XANES spectrum of dehydrated Mo_xO_y/SBA-15 with 5.5 wt.% Mo (0.6 Mo/nm^2) [solid].

6.26 Theoretical and experimental Mo K edge FT($\chi(k)*k^3$) of dehydrated Mo_xO_y/SBA-15 with 5.5 wt.% Mo (0.6 Mo/nm^2). Mo-O and Mo-Mo distances are indicated.

6.27 Comparison of theoretical data with contributions of different vanadia structures (V=O, V-O-V, V-O-Si) and experimental data of the O K-edge NEXAFS of 8.0 wt.% V_xO_y/SBA-15. [46]

6.28 Comparison of the O K-edge NEXAFS spectra at room temperature in the hydrated state (a) 11.1 wt.% Mo (2.4 Mo/nm^2), (b) oxa-SBA-15 and at 350°C in the dehydrated state (c) 11.1 wt.% Mo (2.4 Mo/nm^2), (d) oxa-SBA-15

6.29 O K-edge NEXAFS spectra at 350°C in the dehydrated state (a) 11.1 wt.% Mo (2.4 Mo/nm^2), (b) 5.9 wt.% Mo (0.8 Mo/nm^2) and at room temperature with reference compounds (c) α-MoO_3, (d) hexagonal MoO_3 and (e) $Na_2MoO_4 \cdot 2H_2O$

6.30 *In situ* Raman spectra of Mo_xO_y/SBA-15 (5.9 wt.% Mo, 0.8 Mo/nm^2) at 500°C in (**A**) $C_3H_6/O_2/N_2$ = 0/7/93, (**B**) $C_3H_6/O_2/N_2$ = 3/7/90, (**C**) $C_3H_6/O_2/N_2$ = 0/7/93 and 90 ml/min total. The spectra have been normalized with respect to the Peak at 986 cm^{-1}.

6.31 Mass traces of the reaction products on Mo_xO_y/SBA-15 (5.9 wt.% Mo, 0.8 Mo/nm^2) at (**A**) $C_3H_6/O_2/N_2$ = 0/7/93, (**B**) $C_3H_6/O_2/N_2$ = 3/7/90, (**C**) $C_3H_6/O_2/N_2$ = 0/7/93 and 90 ml/min total flow.

6.32 *In situ* Raman spectra of Mo_xO_y/SBA-15 (10.1 wt.% Mo, 2.0 Mo/nm^2) at 500°C in (**A**) $C_3H_6/O_2/N_2$ = 0/7/93, (**B**) $C_3H_6/O_2/N_2$ = 3/7/90, (**C**) $C_3H_6/O_2/N_2$ = 0/7/93 and 90 ml/min total flow. The spectra have been normalized with respect to the peak at 990 cm^{-1}.

6.33 Mass traces of the reaction products on Mo_xO_y/SBA-15 (10.1 wt.% Mo, 2.0 Mo/nm^2) at (**A**) $C_3H_6/O_2/N_2$ = 0/7/93, (**B**) $C_3H_6/O_2/N_2$ = 3/7/90, (**C**) $C_3H_6/O_2/N_2$ = 0/7/93 and 90 ml/min total flow.

6.34 *In situ* Raman spectra of Mo_xO_y/SBA-15 (19.9 wt.% Mo, 7.6 Mo/nm^2) at 500°C in (**A**) $C_3H_6/O_2/N_2$ = 0/7/93, (**B1/2**) $C_3H_6/O_2/N_2$ = 3/7/90, (**C**) $C_3H_6/O_2/N_2$ = 0/7/93 and 90 ml/min total flow. The spectra have been normalized with respect to the peak at 819 cm^{-1}. The spectra are offset by 1.1 (B1) 2.2 (B2) and 3.3 (C) for clarity.

6.35 Detailed view of the *in situ* Raman spectra shown in Fig. 6.32. The spectra have been normalized with respect to the peak at 819 cm^{-1} and are offset by 0.2 (B1) 0.4 (B2) and 1.0 (C) for clarity.

6.36 Mass traces of the reaction products on Mo_xO_y/SBA-15 (19.9 wt.% Mo, 7.6 Mo/nm^2) at 500°C in (**A**) $C_3H_6/O_2/N_2$ = 0/7/93, (**B**) $C_3H_6/O_2/N_2$ = 3/7/90, (**C**) $C_3H_6/O_2/N_2$ = 0/7/93 and 90 ml/min total flow.

6.37 *In situ* Raman spectra of Mo_xO_y/SBA-15 (10.1 wt.% Mo, 2.0 Mo/nm^2) at 500°C in (**D**) $C_3H_6/O_2/N_2/H_2O$ = 0/10/90/0, (**E**) $C_3H_6/O_2/N_2/H_2O$ = 0/10/45/45, (**F**) $C_3H_6/O_2/N_2/H_2O$ = 3/7/45/45 and 90 ml/min total flow. The spectra have been normalized with respect to the peak at 969 cm^{-1}. For a detailed description see text.

6.38 *In situ* Raman spectra of Mo_xO_y/SBA-15 (5.9 wt.% Mo, 0.8 Mo/nm^2) at 500°C with (**D**) $C_3H_6/O_2/N_2/H_2O$ = 0/10/90/0; (**E**) $C_3H_6/O_2/N_2/H_2O$ = 0/10/45/45 after 2 h and (**D**) $C_3H_6/O_2/N_2/H_2O$ = 0/10/45/45 after 4 h at 90 ml/min total flow. The spectra have been normalized to the peak at 969 cm^{-1}.

8.3. List of Tables

Mo_xO_y/SBA-15 to $^{14}NO/O_2$ and $^{15}NO/O_2$

6.6 Survey of all observed IR adsorbate bands on Mo_xO_y/SBA-15

6.7 Type, number (N), and XAFS disorder parameters (σ^2) of atoms at distance R from the Mo atoms in Mo_xO_y species in dehydrated Mo_xO_y/SBA-15. Experimental parameters were obtained from a refinement of a hexagonal MoO_3 model structure to the experimental Mo K edge XAFS χ(k) of dehydrated Mo_xO_y/SBA-15 (Fig. 6.23) (k range from 3.6 to 14.4 $Å^{-1}$, R range from 0.9 to 4.0 Å, E_0 = 8.0 eV, residual ~ 10.6, N_{ind} = 23, N_{free} = 13). Confidence limits in distances and σ^2 parameters are indicated. Subscript C indicates parameters that were correlated in the refinement.

8.4. List of Schemes

3.1 Effect of narrowed pores in the SBA-15 structure on the isotherm shape.

4.1 Scheme of the functionalization and ion exchange of SBA-15

6.1 Dispersed molybdenum oxide species present on silica SBA-15.

7.1 Dispersed molybdenum oxide species present on silica SBA-15 in dehydrated state.

8.5 Publications

Nitric Oxide Adsorption and Oxidation on SBA-15 Supported Molybdenum Oxide: A Transmission IR Study

J.P. Thielemann, J. Kröhnert, C. Hess, accepted publication *J. Phys. Chem. C* 114 (2010) 17092.

Pore structure and surface area of silica SBA-15: Influence of washing and scale up
J.P. Thielemann, F. Girgsdies, R. Schlögl, C. Hess, submitted to *BJ Nano*

Structure of Molybdenum Oxide Supported on Silica SBA-15 Studied by Raman, UV-Vis and X-Ray Absorption Spectroscopy
J. Thielemann, T. Ressler, A. Walter, G. Tzolova-Müller, R. Schlögl, C. Hess, submitted to *J. Catal.*

Controlled synthesis of highly dispersed molybdenum oxide supported on silica SBA-15
J. Thielemann, G. Weinberg, W. Zhang, R. Schlögl, C. Hess, in preparation

8.6. Poster

SBA-15 supported nanostructured Mo_xO_y- and $V_xMo_yO_z$ model catalysts for partial oxidations
Jörg Thielemann, Christian Hess, Robert Schlögl, 41. Jahrestreffen Deutscher Katalytiker, Weimar (Germany), February 27-29, 2008

Nanostructured Mo_xO_y- model catalysts supported by SBA-15 for partial oxidation reactions
Jörg Thielemann, Christian Hess, Wei Zhang, Jutta Kröhnert, Annette Trunschke, Robert Schlögl, 42. Jahrestreffen Deutscher Katalytiker, Weimar (Germany), March 11-13, 2009

Structure of SBA-15 supported Mo_xO_y-model catalysts for partial oxidation reactions
J. Thielemann, C. Hess, J. Kröhnert, A. Trunschke, A. Walter, T. Ressler, R. Schlögl,
EuropaCat IX, Salamanca (Spain), August 30 - September 4, 2009

Talks

Nanostructured molybdenum and vanadium model catalysts for partial oxidation reactions
Middle East Technical University, Ankara (Turkey), November 16-18, 2009

Eidesstattliche Erklärung

Ich erkläre hiermit an Eides Statt, dass ich meine Dissertation selbstständig und nur mit den angegebenen Hilfsmitteln angefertigt habe.

Berlin, den 16.12.10

(Jörg Thielemann)

Erklärung

Ich erkläre hiermit, noch keinen Promotionsversuch unternommen zu haben.

Berlin, den 16.12.10

(Jörg Thielemann)

PERSÖNLICHE DATEN

Name:	Jörg Thielemann
Geburtsdatum/-ort:	26.09.1979, Berlin
Staatsangehörigkeit:	BRD

AUSBILDUNG

10.2006 – 02.2011 **Promotion**

Fritz-Haber-Institut der Max-Planck-Gesellschaft

Doktorarbeit: Synthesis, Characterization and *in situ* Catalysis of Silica SBA-15 Supported Molybdenum Oxide Model Catalysts

seit 05.2008 Forschungsaufenthalte an der TU-Darmstadt

03. – 09.2006 **Wissenschaftlicher Mitarbeiter**

Universität Münster, Physikalischen Chemie

IRTG Münster – Nagoya (Japan)

10.2000 – 02.2006 **Diplomstudium Chemie**

Universität Potsdam

Diplomarbeit: Synthese und Konformationsanalyse von Alkyl-cyclohexylethern und 1,4-Dialkylcyclohexylethern

08. – 10.2003 **Praktikum in Japan**

Tanaka Kikinzoku Kogyo K.K., Hiratsuka

07.1999 – 04.2000 **Wehrdienst**

6. Feldjägerbataillon 720 Nienburg/Weser
6. Feldjägerbataillon 801 Neumünster

08.1992 – 06.1999 **Abitur**

4. Gymnasium Berlin-Marzahn

Berlin, 17.02.2011

Jörg Thielemann